Doctoral Dissertation (Shinshu University)

Melt-printing technology based on fluid phase for organic thin-film transistors

Shinshu University
Interdisciplinary Graduate School of Science and Technology
Department of Bioscience and Textile Technology

March 2020

Atsuro Ohyama

Acknowledgements

I really would like to thank my advisors, professor Musubu Ichikawa and associate professor Toshiki Koyama for the countless support and guidance through my Ph.D life for the past 5 years. You have been tremendous mentors for me, leading to the right direction and providing precious experience related to research activities all the time.

Also, I would like to express my sincere appreciation to the members in the OTFT team: Anoush Kanamori, Jun Miyazawa, Kazuaki Iwasaki, Nanae Aoyama, Riku Taira, Ryota Kashiwazaki, and Shunsuke Achiha who have cooperated with me at many points. Special thanks to other members, especially Kenta Ishikawa, Nakamura Toshihiro, Ryo Sakurai, Takashi Onoguchi, have spent the large part of my time in and out of the laboratory to inspire each other and share ideas with great passion.

Leaving the main research behind in Japan, I have visited at two research institutions for nearly 1 year; Bangor University, Wales and Imec, Belgium. Firstly, I would like to express the sincerest gratitude to Prof. Martin Taylor to host me at Bangor University and provide heartwarming support for 6 months. I never forget the period when we got nicely working inverters after eating the best tapas at the beautiful countryside. During the internship at Bangor, Wales, Dr. Colin Watson and Dr. Eifion Patchett have also given continuous support for my experiments and expanded my knowledge about the fabrication of integrated circuits. I am sure that a half of my Ph.D work is based on what you taught me. Also, my deepest gratitude will go to the LAE group in Imec, Belgium, especially my advisors, Dr. Cedric Rolin, Dr. Tung-Huei Ke, and Mr Takashi Goto, who have given me lots of chances for me to realize how important the team-working is. That has always been pleased for me to struggle with difficult tasks during the internship. In the private life, I have spent most of time drinking with lovely friends, Daniele and Viktor at Café Belge in the central city of Leuven. Finally, I would like to thank my family and friends in Japan who have never given up keeping touch with me: my parents, my older brother, my younger sister, Takumi, Masahiro, and Yasunobu. It seems like my Ph. D life is completed as a success story.

This work has been supported by a Grant-in-Aid for the Shinshu University Advanced Leading Graduate Program by the Ministry of Education, Culture, Sports, Science and Technology (MEXT), Japan.

Abstract

Thanks to their potential for low temperature fabrication on low-cost large area flexible substrates, circuits based on organic thin film transistors (OTFTs) attract attention for the realization of next-generation electronics such as flexible displays, sensors, and radio-frequency identification tags. The organic thin films as the active layer in OTFTs are prepared by a thermal evaporation process and a solution process, and the latter is arguably regarded to be suitable for the low-cost large area circuits. The realization of this technology has been, however, questioned due to organic solvents exploited in its system to dissolve organic semiconductors (OSCs). There are several severe issues; (1) the usage of environmentally dangerous organic solvents such as a chlorine-based solvent, (2) the impurity indigenously existing in the solvents that hinders the uniform device outputs, (3) the evaporation of the solvents that complicates the control of the thin-film morphology. Hereby, we wonder if we can melt the OSC and spread the molten OSC between a polymer film with a solvent repellent finish and a substrate, leaving high crystalline organic thin-films on the substrate. In this thesis, a new melt-printing technology to exclude the troublesome solvents is developed. First, suspensions of organic semiconductors (naphthalene diimides with long alkyl chains as referred to NTCDI-C*n*) with different melting points are exploited for the development of this technology. A quality of the OSC thin-films related to set-up parameters, for example, process temperature, phase-transition temperature of materials, and thickness of the films, is investigated. Then, the OTFTs are fabricated to check their electrical property, resulting in the highest electron mobility of 0.4 cm^2/Vs, which was comparable to the evaporated TFTs. Second, we aim to developing a solvent-free process by replacing the OSC suspensions with an OSC powder to remove 2-propanol used as a poor solvent in the suspension. The comparison of the morphological and electrical measurements reveals that the quality of the resulting film prepared by using the powder melt-printing process resembles the one prepared by using the suspension melt-printing process. The highest electron mobility of 0.32 cm^2/Vs is obtained from the NTCDI-C13 TFTs. Also, the investigation of a printing film contributes to further understanding the mechanism of the process, resulting in an interesting finding that silica beads indigenously existed in the original polymer film works as spacers to keep a specific distance between the printing film and the substrate to create molecularly smooth thin-films with high crystallinity. The finding leads us to a conclusion that the control of crystal alignment in the films and the patterning of the films are feasible. Finally, a home-made polymer film with no silica beads but with photoresist patterns as the controlled bumps is applied to the powder melt-printing process. As the result, the possibility to control the growth direction of crystalline and to pattern the films with one-shot is shown with the various shape of the thin-films even with the words.

Abbreviation

AFM	atomic force microscopy
a-Si	amorphous silicon
Au	gold
BTBT	[1]benzothieno[3,2-*b*][1]benzothiophene
*C*i	gate dielectric capacitance per unit area
CMOS	complementary metal-oxide-semiconductor
C60MC12	fullerene-fused N-methylpyrrolidine-m-C12-phenyl
D	crystalline size
DCB	dichlorobenzene
DNTT	dinaphtho[2,3-*b*:2',3'-*f*]thieno[3,2-*b*]thiophene
h	film thickness
HOMO	highest occupied molecular orbital
I_D	drain current
$I_{D,lin}$	drain current in linear regime
$I_{D,sat}$	drain current in saturation regime
I_G	gate current
IL	isotropic liquid

I_{on}/I_{off}	on/off ratio
IPA	isopropyl alcohol
K	boltzmann constant
L	channel length
LC	liquid crystal
LUMO	lowest unoccupied molecular orbital
MOSFET	metal-oxide-semiconductor field-effect transistor
NTCDI	naphthalene tetracarboxylic acid diimide
NTCDI-C*n*	naphthalene tetracarboxylic acid diimide derivatives substituted at the N and N' positions with long alkyl chains of varying lengths
OLED	organic light emitting diode
OTFT	organic thin-film transistor
Ph	phenyl
P(NDI2OD-T2)	poly{[*N*,*N*′-bis(2-octyldodecyl)-naphthalene-1,4,5,8-bis(dicarboximide)-2,6-diyl]-*alt*-5,5′-(2,2′-bithiophene)}
PTCDI	perylenetetracarboxydiimide
P5	pentacene
R_{ac}	access resistance
R_c	contact resistance
R_{ch}	channel resistance

R_p	parasitic resistance
RFID	radio-frequency identification
Si	silicon
SiO_2	silicon dioxide
T	temperature
T_m	melting point
TFT	thin-film transistor
TLM	transfer length method
V_D	drain voltage
V_G	gate voltage
V_{on}	on-set voltage
V_{th}	threshold voltage
W	channel width
XRD	x-ray diffraction
μ	mobility
μ_{eff}	effective mobility
μ_{int}	intrinsic mobility
μ_{lin}	mobility in linear regime
μ_{sat}	mobility in saturation regime

λ	wavelength

Table of Contents

Chapter 1

1. Introduction

Electronics technology has significantly advanced in the past few decades. Semiconductor devices have been contributing to this progress[1]; moreover, they recently have come to be essential for our lives, where they play important roles as integrated circuits in almost all electronic components, for example, Smart phones and Televisions. These semiconductor devices, which mostly consist of inorganic transistors such as single-crystalline, polycrystalline, and amorphous silicon are widely used because they are capable of operating at high speed and in an energy efficient manner[2], although devices incorporating on oxide-based semiconductor have been shown up recently[3,4]. However, such devices are less suited not only for flexibility because the process temperature is substantially high more than 300 ℃. At such a high temperature, conventional plastic polymers are thermally unstable and possibly degradable. Therefore, organic thin film transistors (OTFTs) based on organic semiconductors have been attracting significant attention to the flexibility[5].

Organic semiconductors can be deposited on plastic substrates at low temperatures using a vacuum process or a solution process. This is the reason why they are expected to be applied for the next generation of electronic devices such as flexible displays, flexible sensors, and furthermore epidermal devices. Moreover, these materials show wider energy band-gaps (> 2.5 eV) than the ones of inorganic semiconductors so there is a small possibility to thermally generate free charge carriers. Hence, organic thin-film transistors are strong candidates to realize superior off-state behaviors to set the level of the off current at minimum.

1.1 Organic Semiconductors

OTFTs[6–8], organic light-emitting diodes (OLEDs)[9,10], and organic solar cells[11,12] as electronic devices employing organic semiconductors have been researched since the 1900s. Among them, OLEDs have gained significant market share[13], hopefully reaching up to several thousand billion yen[14]. They are especially used for displays in Smart phones; moreover, the market share will certainly increase further in the next few decades. Hereby, the OTFTs, which have distinctive properties such as flexibility, are

expected to be the one of the candidates for backplane circuits in those displays. However, the performance of OTFTs has not reached the level of commercialization compared with OLEDs yet.

The semiconductor used in OTFTs can be divided into n-type and p-type. Since complementary metal oxide semiconductor (CMOS) circuits require both types to fabricate arithmetic circuits and memory circuits, both n- and p-type semiconductors are interesting research topics in the field of OTFTs[15]. Fig. 1.1 (a) shows representative p-type organic semiconductors for OTFTs. Acene derivatives and thiophene derivatives have been used for p-type TFT materials. Among the former analogs, pentacene is the most promising material because some papers have reported that devices consisting of pentacene exhibited higher mobility than that of amorphous silicon devices[16]. In particular, the highest mobility reached up to 5.5 cm^2/Vs after improving the quality of a pentacene thin film with surface treatment and annealing treatment on a silicon substrate[17]. On the other hand, it has been reported that naphtho[2,3-b:2’3’-f]thieno[3,2-b]thiophene (DNTT), a commonly known thiophen derivative, exhibited a mobility greater than 3.0 cm^2/Vs. In addition, rubrene single crystals have been shown to exhibit a mobility of 20 cm^2/Vs, with nearly ideal transistor behavior. Nevertheless, the development of n-type materials, in which electrons are carriers, are less mature than p-type materials because of limited reports of high-performance devices. Naphthalene derivatives and perylene derivatives have been used for n-type TFT materials[18]. In the recent years, high electron mobility of more than 1 cm^2/Vs has been reported from few materials; for example, perylene tetracarboxylic acid diimide (PTCDI) with tridecyl chains at the N and N’ positions achieved a mobility of 2.1 cm^2/Vs after annealing[19]. Naphthalene tetracarboxylic acid diimide (NTCDI) with cyclohexyl chains at the N, N’ positions[20] and fullerene exhibited mobilities near 6 cm^2/Vs, one of the highest carrier mobilities for either n- or p-type organic semiconductors.

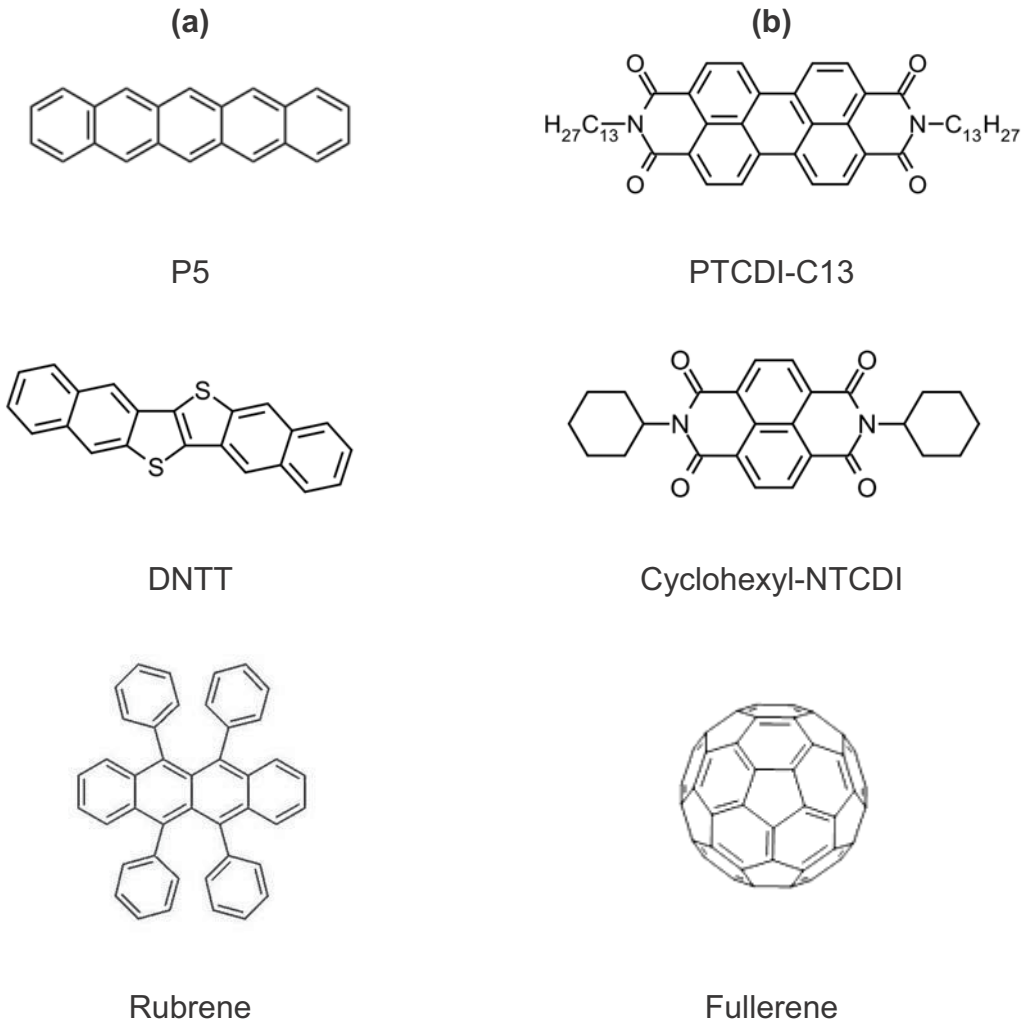

Fig. 1.1 Representative organic semiconductor materials;
(a) p-type semiconductors and (b) n-type semiconductors

Although the mobility in the OTFTs is inferior to that in the TFTs based on polycrystalline silicon (>100 cm^2/Vs) and oxide based transistors (10-80 cm^2/Vs), it has been reported that the mobility is higher than that in amorphous silicon transistors (0.5-1.5 cm^2/Vs). These materials are insoluble in widely used organic solvents. This is the reason why thin films of these materials are prepared by the vacuum evaporation process, which requires high vacuum conditions that have disadvantages for scale-up production, including high costs.

1.1.1 Soluble Organic Semiconductor

The easiest way to make insoluble materials soluble is introducing alkyl chains into the conjugated core called "alkylation." Fig. 1.2 shows representative soluble materials for both n- and p-type OTFTs. The alkylation is believed not to affect a chemical packing of the original materials so that these materials, which are soluble in common organic solvents, have exhibited high mobility up to 1 cm^2/Vs or more. Except for synthesizing new materials, the development of new manufacturing processes also has contributed to enhancing device performances. It is worth mentioning that during crystallization of an organic semiconductor in the state of a liquid, the crystal growth direction can be controlled by a process where solvents evaporate in a certain direction, such as anti-solvent crystallization and patternable solution crystallization. Single crystalline C_n-BTBT prepared by anti-solvent crystallization[21] and single crystalline films of C_{10}-DNTT prepared by patternable solution crystallization[22] exhibited mobilities greater than 10 cm^2/Vs for p-type OTFTs.

Compared with p-type soluble materials, very few soluble n-type materials have shown the benchmark mobility of 1 cm^2/Vs. Fullerene derivatives are well known as good n-type semiconductors[23–25]. In particular, C60MC12 exhibited a mobility near 0.50 cm^2/Vs[26]. Among the NTCDI derivatives, P(NDI2OD-T2) as a polymer TFT material[27] and NTCDI-C13 as a small-molecule TFT material[28] demonstrated relatively high mobilities, 0.8 cm^2/Vs and 0.2 cm^2/Vs, respectively. Hereby, there are still a lot of works remaining for n-type materials.

The interesting tendency to show low mobility was found in solution-processed devices. This is because the soluble materials have small molecular interactions with adjacent molecules that lead to mobility degradation due to small transfer integrals. Hopefully, an organic semiconductor with asymmetric side chains named Ph-BTBT-C10 exhibited both high solubility in common organic solvents and a mobility greater than 10 cm^2/Vs[29].

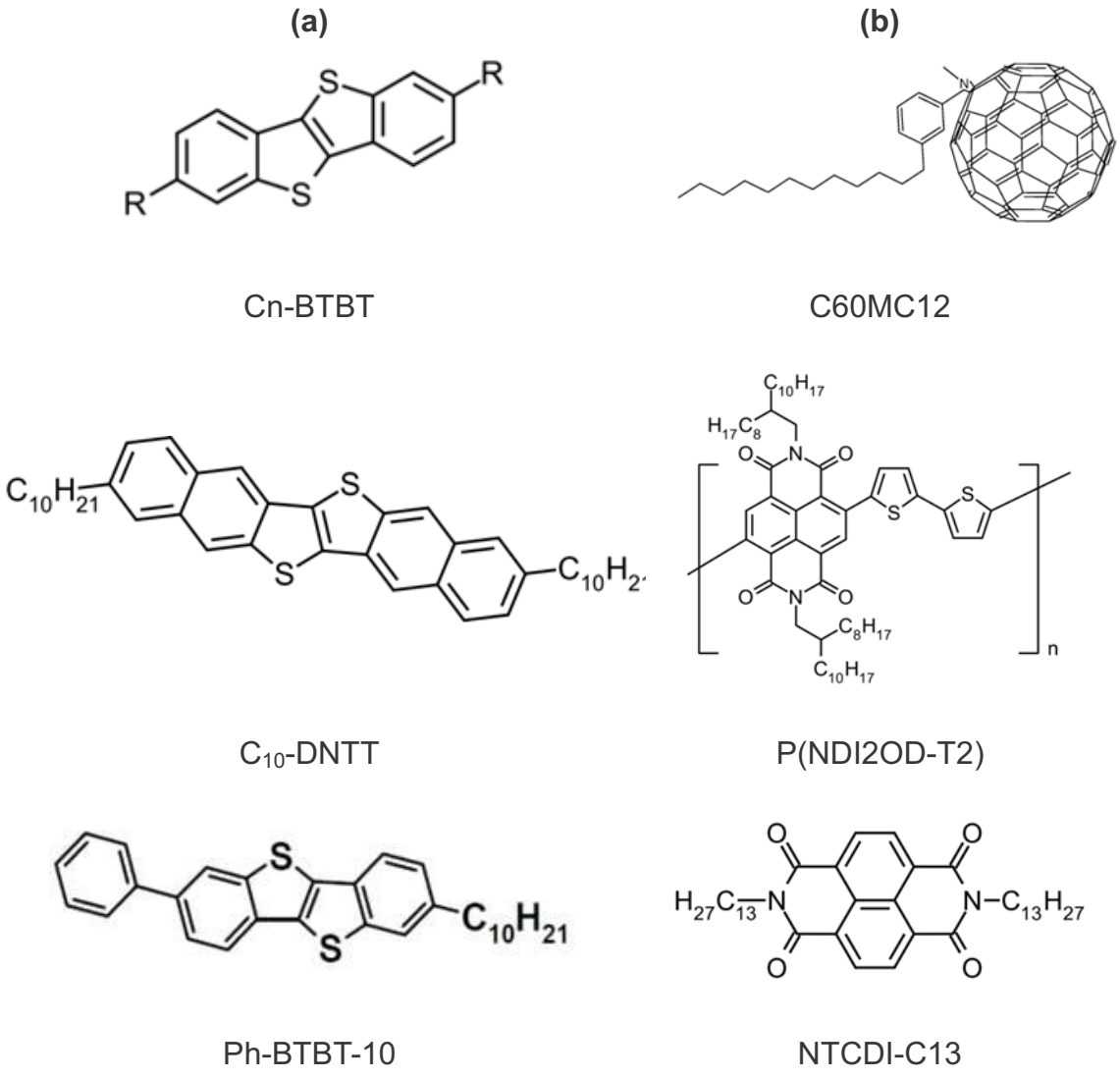

Fig. 1.2 Representative soluble organic semiconductor materials;
(a) p-type semiconductors and (b) n-type semiconductors

1.1.2 Meltable Organic Semiconductor

Fig. 1.3 shows representative organic semiconductors which have melting points below 250 °C. As the rigid core has become smaller and smaller to dissolve in common solvents, among these advanced soluble materials, few of them have come to show another peculiar property of "a melting point" at relatively low temperature less than 250 °C[21,28,30,31]. These materials are attracting attention to the potential for the realization of the dry processes; the materials are molten and re-crystallized to form thin-films without solvents. In principle, states of matter such as crystal liquid and

isotropic liquid can be exploited to soften them by adding heat and/or mechanical pressure to form thin-films.

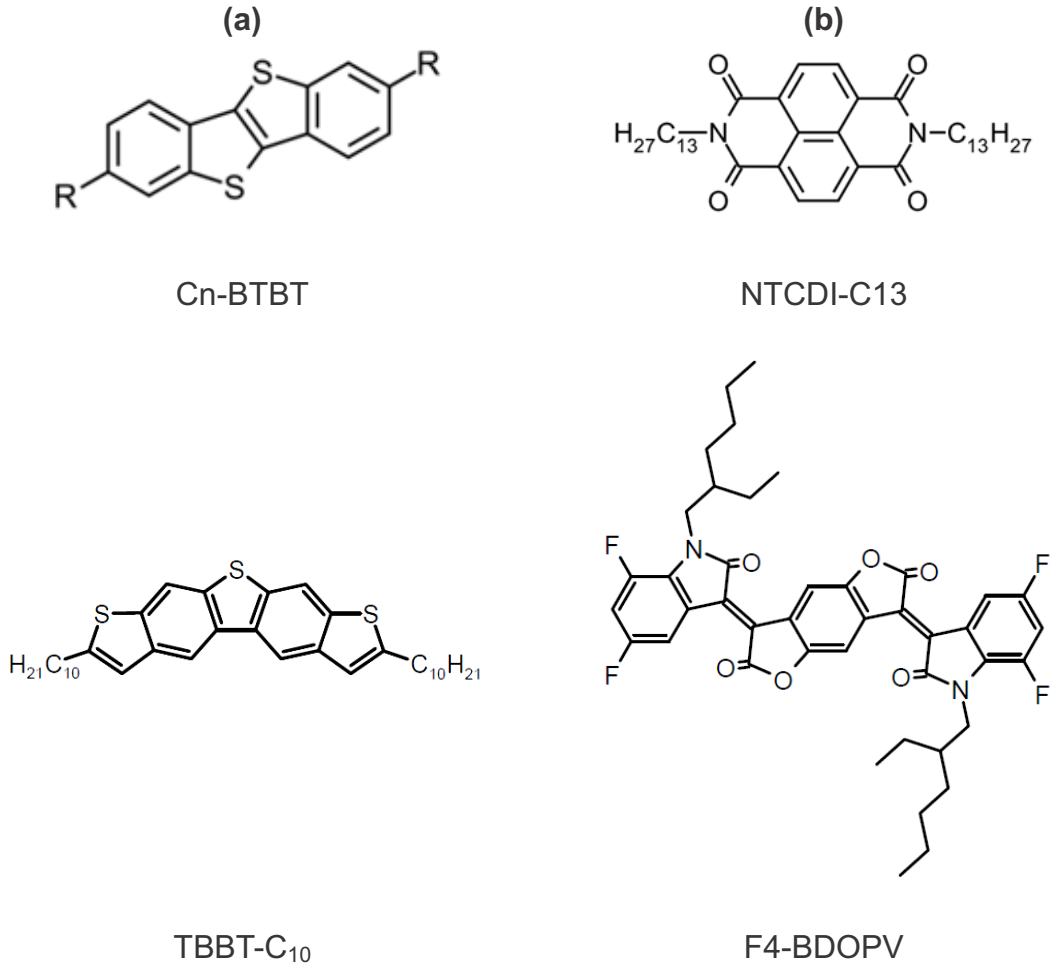

Fig. 1.3 Candidates of meltable organic semiconductor materials used for future melting processes; (a) p-type semiconductors and (b) n-type semiconductors

1.2 Organic thin film transistor

1.2.1 Device structure

An OTFT is a kind of field effect transistor composed of a gate electrode, a gate dielectric, an OSC, and source and drain (S/D) electrode layers. The OTFT structures are divided into two widely used designs, i.e., the bottom contact (BC) structure and top contact (TC) structure[32]. In the former structure, the S/D electrodes are formed on the gate dielectric using photolithography. The electrodes are prepared on the organic semiconductor through a shadow mask in the TC structure. The photolithography is suitable for producing highly reproducible micrometer-sized electrodes. Therefore,

considering the commercialization of OTFTs, the BC structure is suited for miniaturization and integration in electronic components. However, bottom contact devices lead to performance deterioration because of the low crystallinity of OSC on the S/D electrodes and insufficient contact between the electrodes and the semiconductor[33–35]. As the result, the TC structure is preferred for investigating the precise TFT performance of thin films.

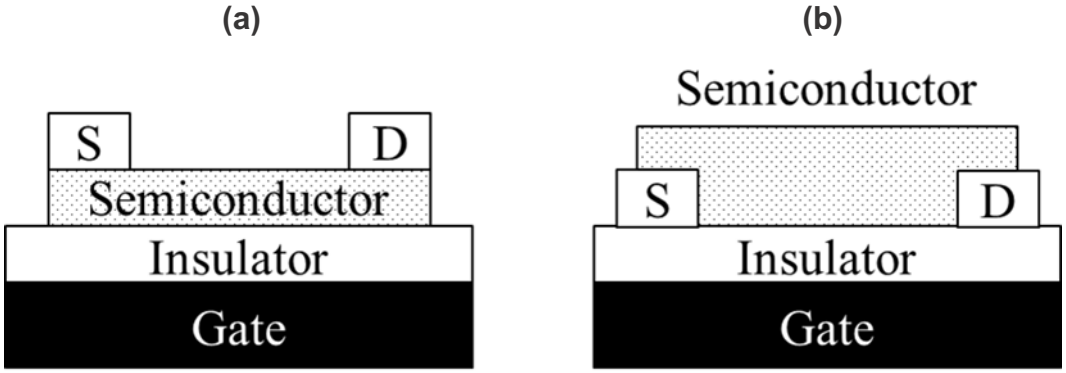

Fig. 1.4 Illustrations of OTFT;
(a) TC structure and (b) BC structure.

1.2.2 Operation

Fig. 1.5 illustrates an OTFT circuit. In OTFTs, electric current flows at the interface of the organic semiconductor and the gate dielectric by exploiting the potential difference between the source and drain electrodes when carriers are accumulated at the interface by applying a voltage at the gate electrode. The intrinsic conductivity of semiconductors is very little that, as long as no voltage is applied at the gate electrode, it is difficult for electric current to flow. This is why transistors can function as switching devices when a voltage is applied. Fig. 1.6 illustrates the two systems (p-type and n-type) in which electric current flow using energy band diagrams, which define with the lowest possible conduction band energy (E_c) and the highest possible valence band energy (E_v). In the system for p-type semiconductors, holes are accumulated at the interface of the dielectric and the semiconductor when a negative voltage is applied to the gate electrode. In contrast, for n-type semiconductors, electrons are accumulated between the gate dielectric and the semiconductor when a positive voltage is applied to the gate electrode. In such situations, electric current can be generated from the potential difference between source and drain electrodes[36]. Since OSC films in OTFTs are polycrystalline,

many grain boundaries exist between every crystalline, resulting in the significant energetic disorder[37]. Hereby, decreasing the number of grain boundaries contributes to the favorable carrier transport in principle.

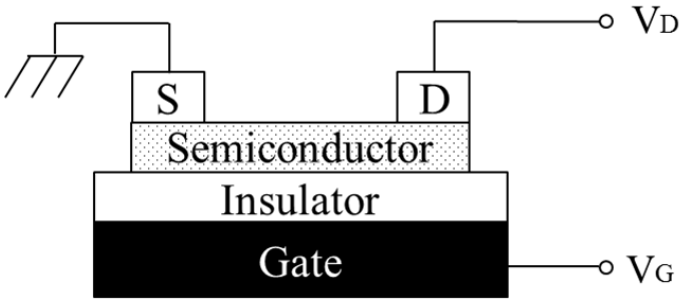

Fig. 1.5 Schematic illustration of OTFT measuring circuit.

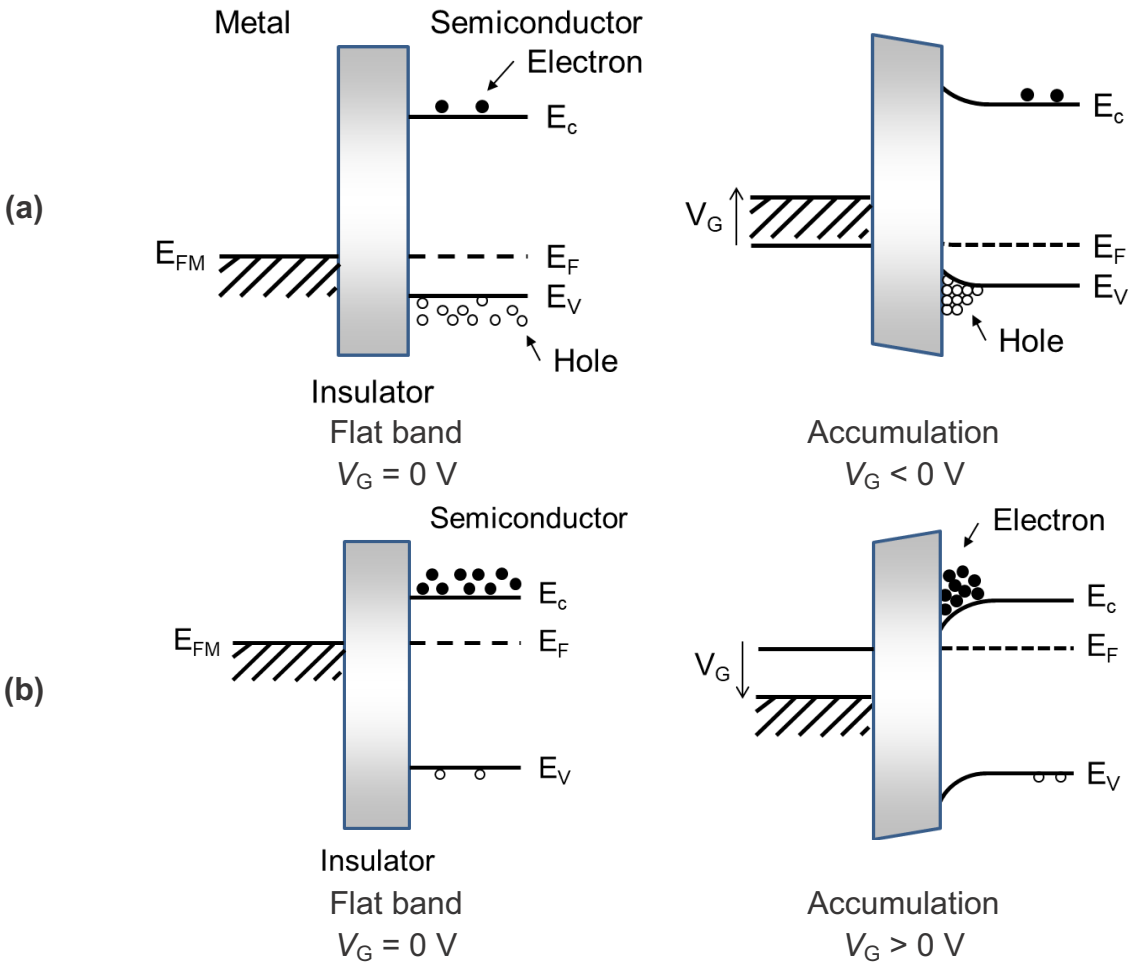

Fig. 1.6 Energy band diagram for OTFTs;
(a) p-type semiconductor , (b) n-type semiconductor.

The OTFTs can be used as a test structure to determine the mobility, in addition to key elements in circuits. The most widely used method to evaluate the mobility and threshold voltage is the classical metal-oxide-semiconductor field-effect transistor (MOSFET) model. This model naturally can be divided into two operating regimes, i.e., the linear regime and saturation regime. Fig. 1.7 shows the representative drain current (I_D) - gate voltage (V_G) and the drain current (I_D) - drain voltage (V_G) characteristics of n-type OTFTs. The drain current (I_D) can be described as in equation (1.1) in linear mode and equation (1.2) in saturation mode. The slope and intercept of the linear fits to the square root of the saturation I_D versus V_G relationship provide the mobility and threshold voltage. Another approach is to use the channel resistivity (R_{ch}) extracted with the transfer line method (TLM)[38]. By substituting the channel resistivity into equation (1.3), μ can be extracted in situations where the μ depends significantly on the channel resistance.

$$I_{D,lin} = \frac{W\mu C_i}{L}(V_G - V_{th})V_D \qquad (1.1)$$

$$I_{D,sat} = \frac{W\mu C_i}{2L}(V_G - V_{th})^2 \qquad (1.2)$$

$$\mu = \frac{I_{D,lin}L}{WC_i(V_G - V_{th})V_D} = \frac{1}{C_i(V_G - V_{th})R_{ch}} \qquad (1.3)$$

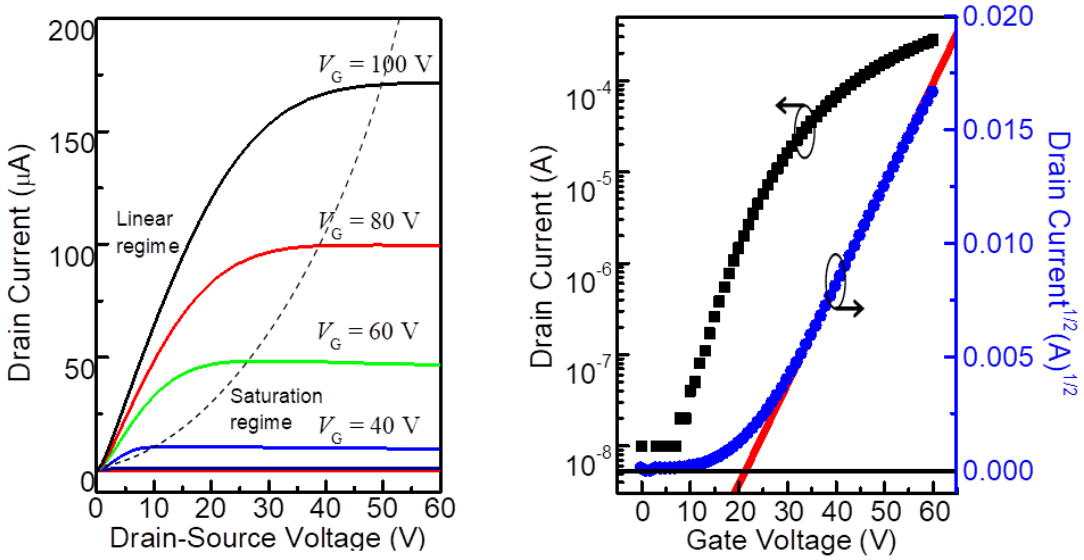

Fig. 1.7 Representative n-type OTFT characteristics.

1.2.3 Resistance component

The Total resistance in OTFTs is divided into three components, i.e., the contact resistance (R_c), access resistance (R_{ac}), and channel resistance (R_{ch}). R_c is generated at the interface between the source and drain electrodes and the organic semiconductor. R_{ac} is the resistance in the out-of-plane direction in the organic semiconductor from the source and drain electrodes to the active channel, and R_{ch} is the resistance in the in-plane direction in the organic semiconductor. R_{ac} is not generated in the bottom contact structure, only in the TC. Previous reports suggest that increasing the thickness of the organic semiconductor leads to an increase in both the R_{ac} and also the disorder of the molecular packing because the diffusion of metal particles in the organic semiconductor generates the extra R_{ac}. However, the separation of the R_{ac} and R_c is not feasible. This is why the total resistance of R_{ac} and R_c is called parasitic resistance (R_p) in this thesis; moreover, the sum of total R_p and R_{ch} is called total resistance (R_t).

1.3 Manufacturing

As previously mentioned, the market demand for OLEDs has been increasing rapidly and globally. This is the reason why the research field of electronic circuits based on the OTFTs remains interesting. The most interesting advantage for the OTFTs is the fabrication at low temperature less than 200 ℃. This makes it possible that the OTFTs can assemble on the plastic foil.

The manufacturing processes for the OTFTs are roughly divided to three kinds; thermal evaporation, solution process, and melting process.

1.3.1 Thermal Evaporation

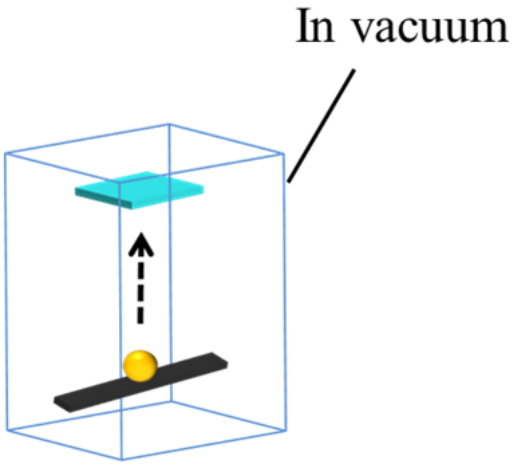

Fig. 1.8 Illustration of the vacuum evaporation process.

The thermal evaporation, illustrated in Fig. 1.8, since there is no need for OSCs to be soluble, high mobility insoluble materials can be used; moreover, simultaneous patterning of thin films through a shadow mask and preparation of re-producible devices with uniform performances are feasible. Hereby, the evaporation process has widely been used to prepare thin films in organic electronics. In this process, however, organic thin-films are prepared by thermally evaporating the powder set on a heated board and by accumulating molecules layer by layer so that requires high vacuum conditions (base pressure < 10^{-6} Torr) otherwise the OSCs are easily damaged and degraded by the heat. This makes the evaporation process difficult to achieve scale-up fabrication in a cost-effective manner.

Large-scale set-ups are needed for high vacuum process which is not compatible with the roll-to-roll process although Martin *et al.* reported a process to fabricate flexible OTFTs consisted of DNTT exhibited mobilities greater than 1.0 cm^2/Vs in a roll-to-roll compatible environment[39–41].

1.3.2 Solution Process

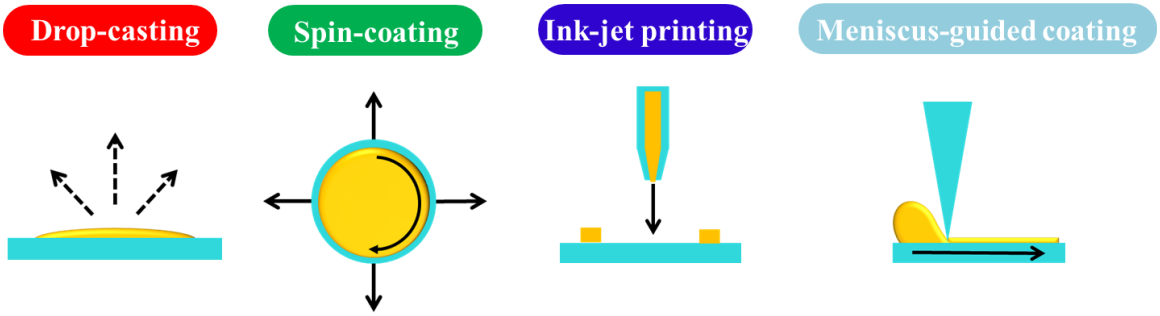

Fig. 1.9 Representative solution processes.

Due to the intrinsic problem of the thermal evaporation process, the counterpart has been a promising candidate to fabricate OTFTs for commercialization in recent 10 years. There seem to be several requirements to make the solution-processed thin-film reach at the level of the thermal evaporation processed ones; high crystallinity, molecularly smooth surface, low material consumption, environmentally friendliness, short time of process, et cetera. At present, there are many reports regarding solution processed OTFTs[42] but no reports can satisfy all the requirements. We pick up well-known solution processes hereafter.

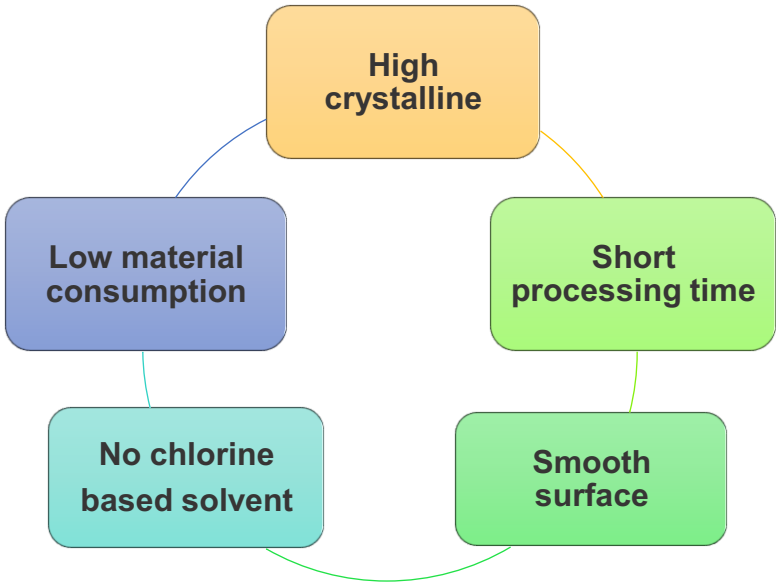

Fig. 1.10 Requirements for solution processes.

1.3.2.1 Drop-Casting

The concept of drop-casting is that the organic semiconductor solution is dropped on a

substrate and solvent evaporates slowly, leaving self-assembled thin-films[43,44]. To create high crystalline thin-films in this process, the drying time has to be long enough for molecules to crystallize in the solution. Thus, a solvent with a high boiling point such as DCB is typically used to achieve high performance. Not surprisingly, the processing time is substantially long. In addition, a coffee stain phenomenon[45] that the solvent dries from the edge of droplets to the center causes poor uniformity for the resulting films.

1.3.2.2 Spin-Coating

The spin-coating is one of commonly used solution processes besides the drop-casting in the semiconductor industry thanks to its consistency and scalability for reproducible uniform thin-films[46]. The solution is dropped on a substrate spinning at a set speed while spreading the solution out of the substrate. By adjusting the concentration of solution and the spin-speed, the thickness can be controlled easily so the spin-coating has been used to deposit OSCs to analyze their crystal features in thin-films, to test their electrical properties and to use as references until now[28,47].

Due to their fast drying time and the various directions of spreading the solution, the crystallinity of the thin-films is usually lower than drop-casting in principle so the performance tends to be poor except for some cases, where the direction of spreading the solution is carefully controlled.[48–50] In addition, the flown solution out of the substrate is ruined and this gets the material consumption efficiency low.

1.3.2.3 Meniscus-Guided Coating

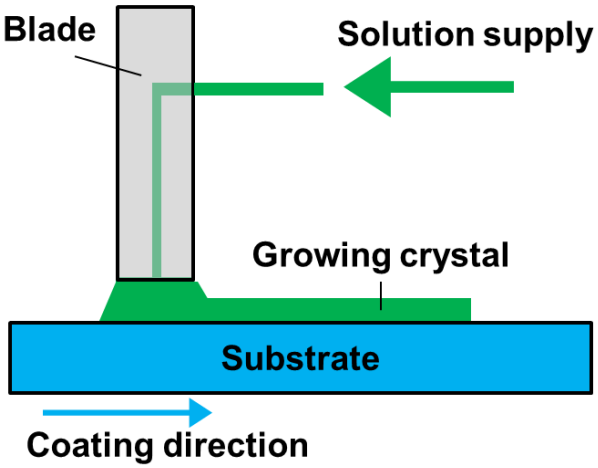

Fig. 1.11 Schematic representation of the zone-casting tool[51].

One of the most promising solution processes is the meniscus-guided coating[52–54]. The

difference from the drop-casting and the spin-coating are singled out about the direction of crystal growth during the processing. As illustrated in Fig. 1.9, the blade, which set on a slightly above the substrate shears slowly the solution kept in the gap between the blade and the substrate, leaving uniaxially grown crystals in the direction of shearing. A mobility greater than 5 cm^2/Vs have been exhibited consistently according to some references. More importantly, the state of the art meniscus-guided coating named "edge-casting" or "zone-casting" can provide the solution from the inside of the blade[51,55] and can prepare homogeneous single crystals composed of an OSC bimolecular layer[56].

There might be intrinsic issues that the surface of the substrate has to be necessarily smooth and highly hydrophilic.

1.3.2.4 Printing

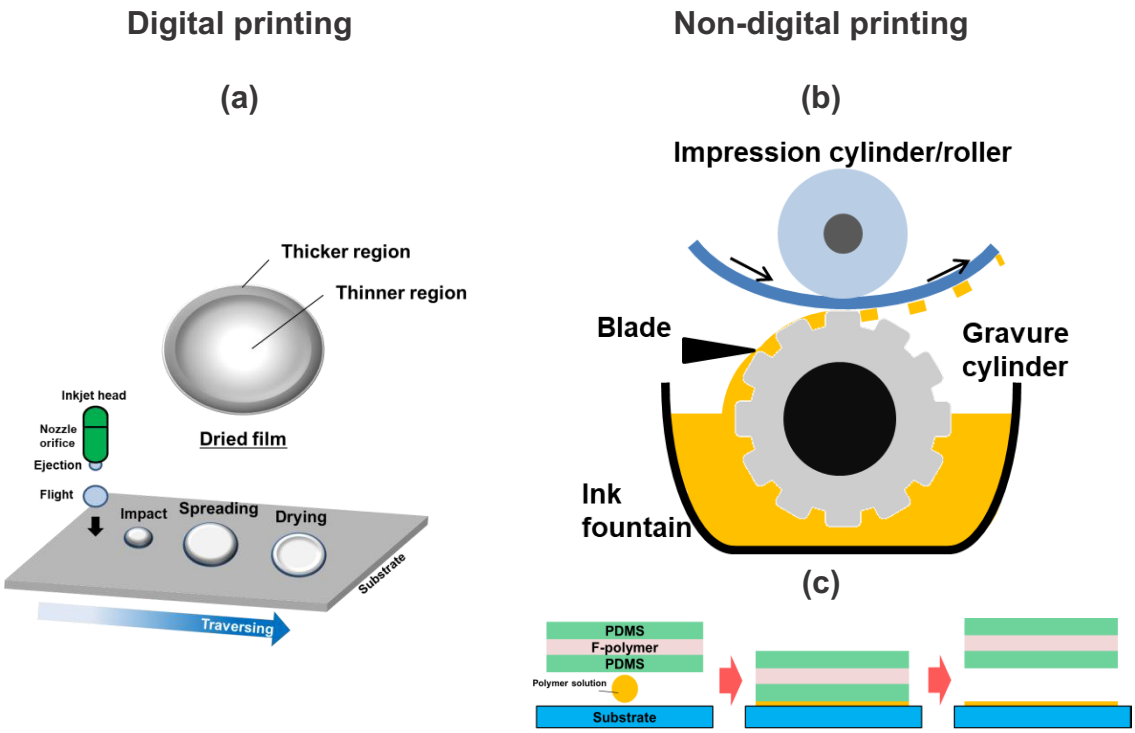

Fig. 1.12 Schematic illustration of the representative a digital method (a) ink-jet printing[42], and non-digital printing methods (b) gravure printing process[42] and (c) push-coating process[57].

Since the history of the printing goes back long, long time ago (before 220), there are

countless kinds of the printing processes at present[42,58], mainly divided into digital methods such as ink-jet printing[59] and non-digital methods such as screen printing[60] and offset printing[61,62]. Both the processes are capable of scale-up manufacturing for OTFTs in a cost-efficient manner. For example, the ink-jet printing that jets OSC droplets from multiple nozzles to a substrate moving at high speed can make any patterns in high resolution on the fly. In the ink-jet printing, the surface treatment is required in most of the cases otherwise the droplets arrived on the substrate cause the coffee stain phenomenon during the dry as explained in Fig. 1.12 (a)[42,63]. Therefore, the non-digital methods are more promising about the reproducible devices because no nozzles are involved and OSCs are able to directly be transferred from the contact line to the substrate (Fig. 1.12 (b) and (c))[64–67].

Note that the usage of toxic organic solvents is mandatory for the solution processes to completely dissolve OSCs to confirm homogeneous films. Therefore, environmentally friendly processes to get rid of these solvents will be required for the upcoming generation of electronics.

1.3.3 Environmentally Friendly Process

As previously pointed out, common organic solvents, especially chlorine based solvents such as chloroform and DCB, are used in solution processes and the use of chlorine-based solvents is arguable with many reasons. Not surprisingly, the trend of switching the conventional processes to environmentally friendly and even solvent-free processes has been increasing in several industries and the movement have almost come to the field of organic electronics not only in the material synthesis but also in the manufacturing[68–73]. Considering this viewpoint, the next generation of the manufacturing process for OTFTs will be environmentally friendly or solvent-free.

1.3.3.1 Suspension

Some researchers have attempted to modify a conventional solution process into an environmentally friendly one by selecting solvents such as water, ethanol, and IPA and by not dissolving but dispersing OSCs in their poor solvent. For example, Gill *et al.* have explored the successful fabrication of n-type OTFTs devices prepared by drop-casting an OSC suspension. However, the OTFT performances of these devices deteriorated down to 1% of the performance of the device prepared by the vacuum

evaporation process[51]; this deterioration occurred because the many grain boundaries generated in thin films made from organic semiconductor in a poor solvent, organic semiconductor suspension, and organic semiconductor powder limited the carrier transportation in OTFTs. It implies that it is difficult for conventional solution processes to be applied to these suspensions because granular thin-films are formed, resulting in polycrystalline films with poor connections at boundaries between grains. Therefore, a new process that can be used with these suspensions or that exploits different film-forming mechanisms is needed for the fabrication of thin films.

1.3.3.2 Solvent-free Process

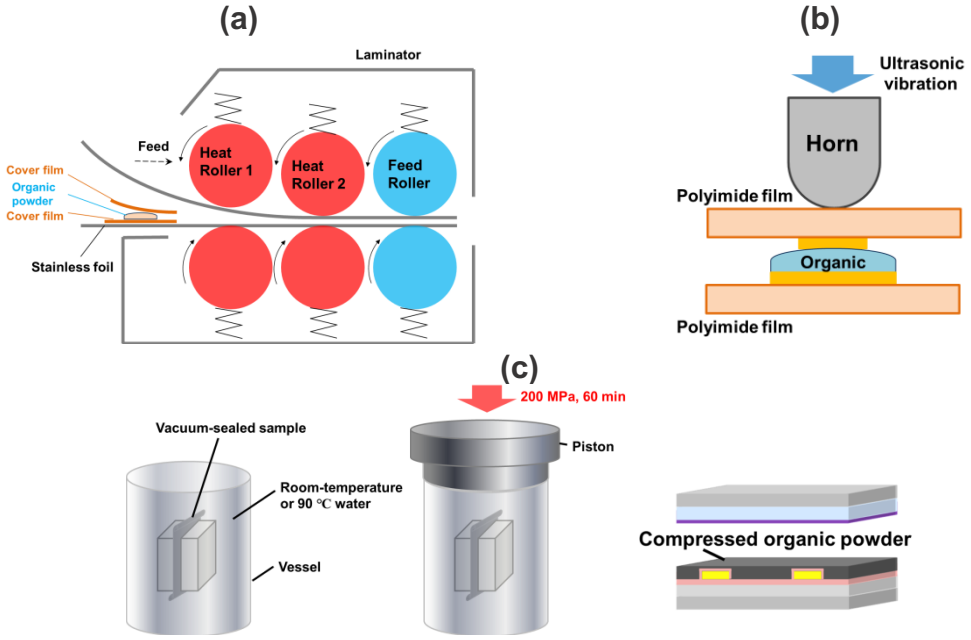

Fig. 1.13 (a) A schematic illustration of OFET fabrication by the thermal lamination process[74]. (b) Illustration of an ultrasonic welder[75]. (c) Illustrations of hot isostatic pressing (HIP) techniques[76].

In this thesis, a solvent-free process is defined as a process which does not use any solvent to prepare organic semiconductor thin-films. Such a process is barely feasible by using transition phases of OSCs; the phase of liquid crystal phase and liquid phase, where the OSCs are relatively softer than the state of solids and formable to thin-films by using heat and/or mechanical forces.

There are a few reports of solvent-free processes[74–76]. A research group at Chiba University has successfully developed p-type OTFTs by annealing C8-BTBT at temperatures greater than the melting points in a thermal lamination process and

ultrasonic welding (Fig. 1. 13. (a) and (b)). Thanks to the transition, the material has formed thin-films showing a mobility up to 3 cm^2/Vs which is slightly lower than the ones of the devices prepared by the thermal evaporation and the solution processes. Matsushima et al. also have developed a solvent-free process (although they used water as solvent) to fabricate organic layers for TFT devices using a hot isostatic pressing, where the OSC powder pressed by water pressure in its crystal liquid phase (Fig. 1.13. (c)). Similarly, those processes annealed and pressed OSCs in soft matters to force the solids to be films. Due to the pressing, the surface of the resulting films seemed to be rough and the control of the thickness may be challenging.

On the other hand, when it comes to other classes of electric and electronic materials except for OSCs, there are, in fact, excellent reports about formation of conductive and/or semiconducting thin-films or layers based on particles such as metals and metal oxides[77–79].

1.4 Aims and Outlines

This research is aimed at developing a new offset printing process that exploits an isotropic liquid phase of organic semiconductors to create thin-films without using chlorine-based solvents and further without using any solvent. This research will be divided into two key parts, i.e., employing suspensions of OSCs to replace the toxic solvent with IPA and then removing IPA from the system to develop a solvent-free process. In chapter 3, we demonstrate OTFTs by depositing n-type organic semiconductor suspensions. Our team develops OTFTs by melt-printing an OSC suspension, annealing at the temperature greater than the melting point of the OSC, spreading the molten between a printing film and a substrate, and cooling down the material slowly. This technology leads to larger grains in thin-films implying that the number of grain boundaries decreased in the active channel as well as leads to molecularly smooth surface. In the chapter 4, we attempt to get rid of IPA from the system and prepare high crystalline organic thin-films with the molecularly flat surface. It is also proved that this process requires a small amount of OSCs (0.01 mg) to form the square area of 1 cm^2 to confirm high material consumption efficiency because all materials can be used to form the thin-films. At the end of the chapter, we reveal the mechanism of this process and prove the most important factor to form molecularly

smooth thin-films with high crystallinity. The findings lead us to propose a new printing film so-called “printing plate” based on a polyimide film and a photoresist material in chapter 5. It is concluded that this process is expected to be able to control the crystallinity and the shape of thins films in the future. We would like to show some clues to do so at the end.

Chapter 2

2. Experimental

This chapter is partially supported from the following publications:

Atsuro Ohyama, Jun Miyazawa, Yoichiro Yokota, Naoki Hirata, Naomi Oguma, Musubu Ichikawa, **Printing technology based on isotropic liquid phase of naphthalene diimide derivatives for n-type organic transistors**

Atsuro Ohyama, Naoki Hirata, Naomi Oguma, Musubu Ichikawa, **Solvent-free printing process for organic transistors using a naphthalene diimide bearing long alkyl chains**

This chapter summarizes all information related to materials and methods used in this thesis apart from Chapter 5. Firstly, the selection of organic semiconductors with a melting point is discussed in the section 2.1. Then, the preparation of suspensions and printing films used in printing are detailed. Moreover, full information of the melt-printing technology is disclosed in the section 2.2. Finally, the characterization methods for these films are described in the section 2.3, followed by the detailed information about the fabrication of OTFTs in the section 2.4.

2.1 Organic Semiconductors

Since we exploit a melting point to develop a new process, materials which show an isotropic liquid phase at relatively low temperature less than 250 ℃ have to be chosen as an OSC. Furthermore, a LC phase should be essential to enhance its crystallinity when the OSC is molten and self-organized. Therefore, NTCDI-C*n*s are selected as the OSC layers in this research.

2.1.1 NTCDI-C*n*

We selected naphthalene tetracarboxylic diimides with long alkyl chains at the *N*,*N*′ positions (NTCDI-C*n*, see Fig. 2.1(a)). These materials are processable by both the thermal evaporation process and the solution process. Moreover, they had showed a

relatively high field-effect electron mobility (> 0.1 $cm^2 V^{-1} s^{-1}$) from the evaporated devices and the spin-coated devices according to previous studies[28,80].

NTCDI-C*n* derivatives were synthesized from naphthalene-1,4,5,8-tetracarboxylic acid dianhydride and the corresponding alkylamine according to literature procedures[20,81]. Through subsequent purifications by using a gel-permeation chromatography column (JAI, JAIGEL 1H-40) and re-crystallization, the white powder was collected and determined as the target materials. As shown in Fig. 2.1 (a), we expect that NTCDI-C13 changes its forms from the liquid crystal to the isotropic liquid at more or less 160 ℃ according to references[28,80]. The phase transition behavior of each NTCDI-C*n* is summarized on Table 2.1. Considering the gathered information about NTCDI-C*n*s, these materials are seemed to be suitable for the understanding of the printing technology in the beginning stage.

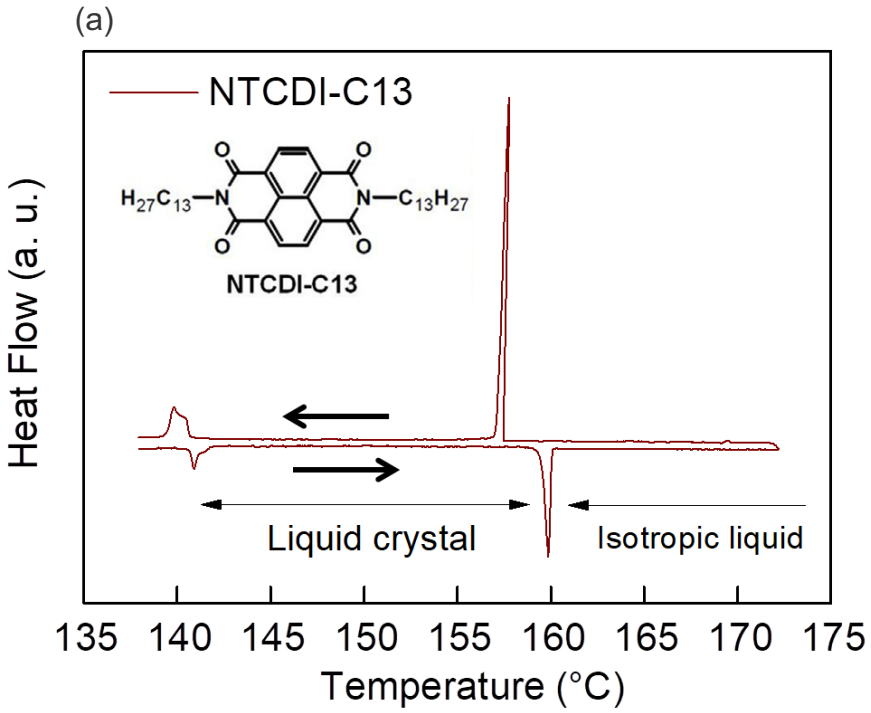

Fig. 2.1 (a) Chemical structure of NTCDI-C*n*, (b) microscope image of the crystals in the C13 powder, and (c) Differential scanning calorimetry (DSC) curves of NTCDI-C13.

Table 2.1 Phase transition behavior of each NTCDI-C*n* measured by using DSC. *K* and *LC* represent crystalline and liquid crystalline states, respectively.

NTCDI-	Transition Temperature (°C)		
	K-K	***K-LC***	***LC-IL***
C8	-	171.1	185.1
C13	109.2	143.6	162.3
C15	114.2	139.6	156.2

2.2 Film Preparation

2.2.1 Suspension

NTCDI-C*n* suspensions were prepared through the so-called re-precipitation method as follows. First, a 0.1 wt% chloroform solution of NTCDI-C*n* was prepared and then was injected into IPA under vigorous stirring. The injection rate was 100 μL/min controlled by a micro syringe pump as illustrated in Fig. 2.2. NTCDI-C*n* suspensions were finally prepared after concentration to 0.1 wt% and removal of the remaining chloroform from the suspension under vacuum, as shown in Fig. 2.2. Fig. 2.3(b), (c) and (d) show granules of NTCDI-C8, 13, 15 in their suspensions after dropping a droplet of the suspensions and drying IPA to leave granules on a slide glass. The granules were needle-like crystals, approximately 3 μm in length and 100 nm in width. Increasing the number of carbon atoms in alkyl chains changed the appearance of crystals from the plate-like crystals for C8 and the needle-like crystals for C13 and C15. We successfully prepared the reproducible microcrystals which are expected to melt and fuse more easily to create enlarged grains. These suspensions are used in chapter 3.

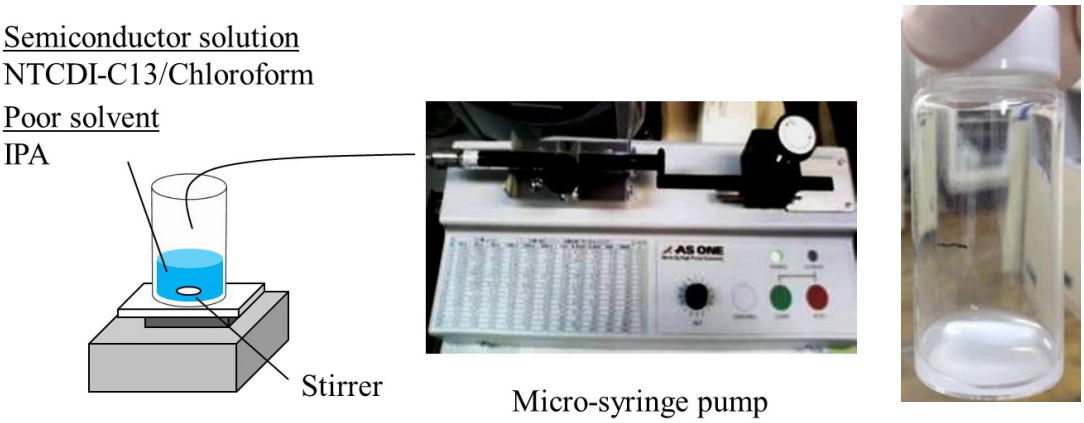

Fig. 2.2 (a) Illustration of the re-precipitation method for NTCDI-C*n* suspensions (b) Image of the 0.1 wt% suspension after concentrating.

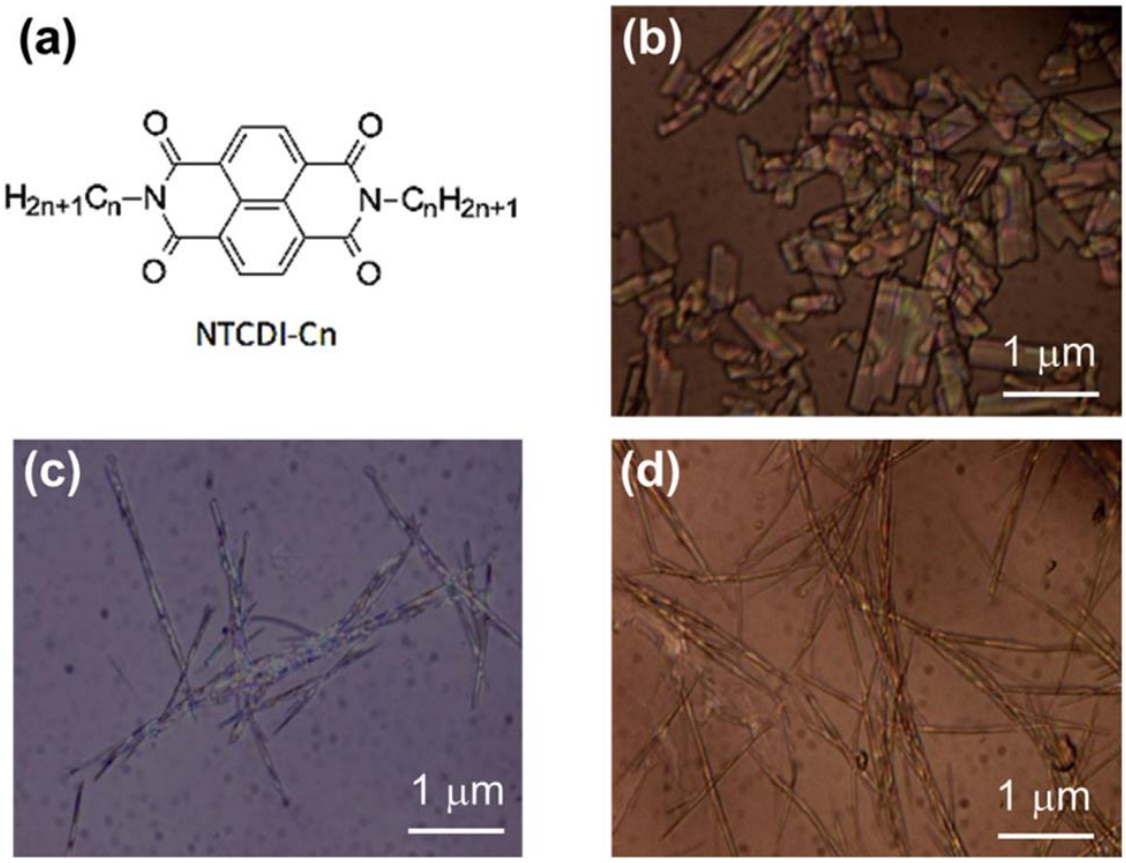

Fig. 2.3. (a) Chemical structure of the organic semiconductors NTCDI-C*n* and microscope images of the crystals in NTCDI-C*n* suspensions prepared on a glass plate; NTCDI-C8 (b), -C13 (c), and -C15 (d).

2.2.2 Printing Film

A 75-μm-thick polyimide (PI) film (Fig. 2.4(a)), obtained from UBE Industries, Ltd. (UPILEX®-75S), was treated with a solvent repellent reagent following a previously reported process. A 0.5-wt% 1-butanol solution of *N*-phenyl-3-aminopropyltrimethoxysilane was spin-coated on a PI film at 2000 rpm for 45 s and then annealed at 90 °C for 5 min on a hot plate. CYTOP solution (purchased from AGC) as a solvent repellent reagent was spin-coated at 5000 rpm for 60 s onto the film and annealed at 180 °C for 20 min in an oven. The water contact angle on the surface was 114.4°. Hereafter, the treated PI films are denoted as printing films. These films are mainly used in chapter 3.

2.2.3 Home-Made Printing Film

Printing films are also prepared at our laboratory from the PI precursor vanish (UPIA®, UBE Industries, Ltd) through the following steps. The vanish was spin-coated at 750 rpm for 60 s on the flat surface of a Si wafer and the spin-coating repeated once again. The silicon wafer with the vanish was annealed at 80 ℃ for 20 h and 100-180 ℃ by 20 ℃ each 30 min, and 200-260℃ by 20 ℃ each 15 min in air to confirm the good uniformity of PI film. Fig. 2.4(b) shows the 30-μm-thick PI film (abbreviated as vPI hereafter). The thickness of the vPI is thinner than UPILEX®-75S due to the difficulty in the preparation. The face side attached with the flat surface of the Si wafer was treated with the solvent repellent reagent through the same steps to be used as the printing films, mainly in chapter 4 and chapter 5.

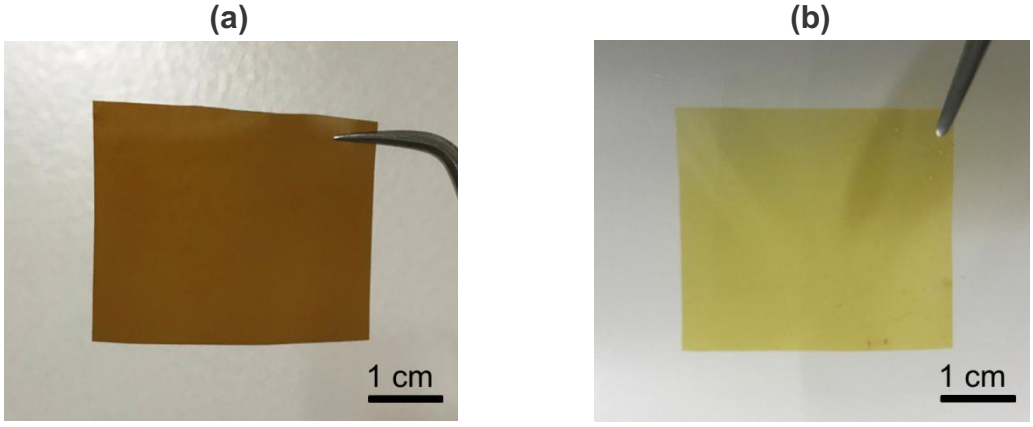

Fig. 2.4 Image of the 70-μm-thick PI film (a) and the vPI (b).

2.2.4 Suspension Melt-Printing Technology

Fig. 2.5 shows the process flow diagram. A 10–150 mL portion of the suspension was softly dropped onto the printing film, and then the droplet was carefully dried on a cold metal block to remove IPA. After the preparation of the dried film, the film was turned upside down and placed on a Si wafer with a 200-nm-thick SiO_2 layer, and then an arbitrary load was applied to the film to hold it on the wafer. The setup was annealed above the melting point of each NTCDI-C*n* for 1–2 h in a vacuum oven, and then cooled down slowly. The annealing temperature was measured with a thermocouple attached to the surface of another Si wafer placed right alongside the printing set. The averaged maximum temperature in the annealing processes for C13 was 173 ± 1.8 ℃. In the case where the maximum annealing temperature was below the melting point, the solid did not melt and flow under the printing film. An OSC film was left on the Si wafer after peeling off the printing film. The films prepared by this technology are detailed in chapter 3.

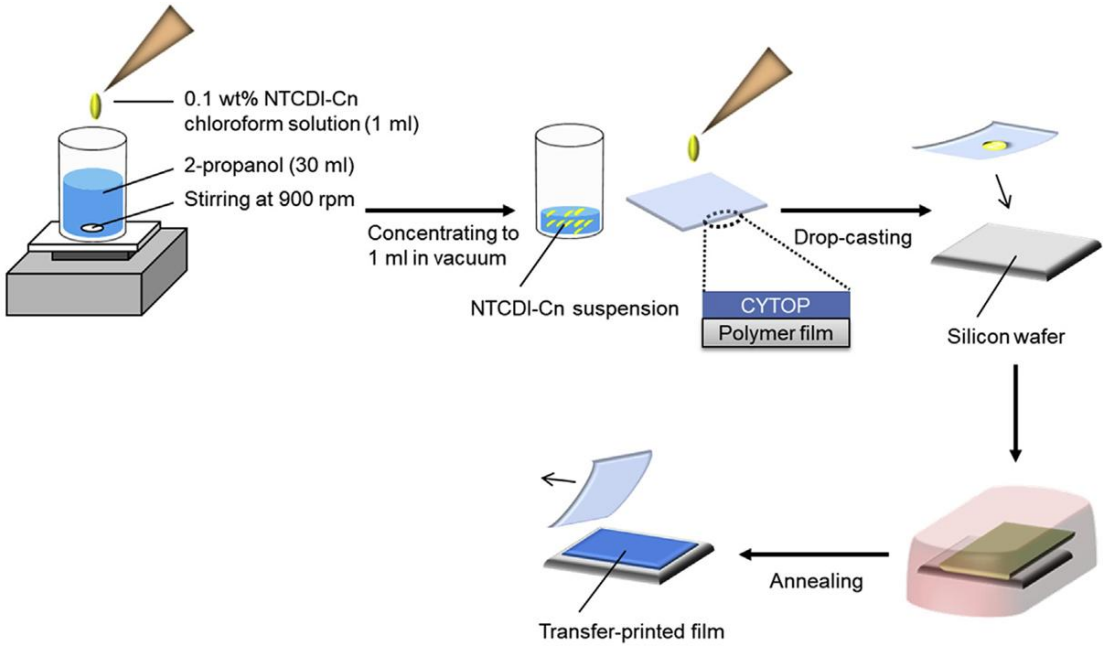

Fig. 2. 5 Schematic illustration of all steps in the melt-printing technology.

2.2.5 Powder Melt-Printing Technology

The micrograph image in Fig. 2.6 confirmed that the C13 powder consisted plate-like microcrystallines with a length of approximately 100 μm and width of 30 μm. The C13 powder after the purification using the gel-permeation chromatography column and

recrystallization was used directly for the process. C13 thin films were prepared by the following steps modified for the powder melt-printing process. First, a small amount (less than 0.01 mg) of the C13 powder was placed on a printing film based on the printing film. Second, the printing film with the C13 powder was turned upside down, placed on a Si substrate, and then annealed in an oven under vacuum. The powder might electrostatically attach to the film because it did not fall off the film upon inversion. During annealing, the C13 powder melted and then the molten material isotropically spread from the area where the powder was placed until the molten reached to the opposite edge of the PI film. Finally, a C13 thin film was left on the Si substrate by peeling off the printing film. The films prepared by the technology are detailed in chapter 4.

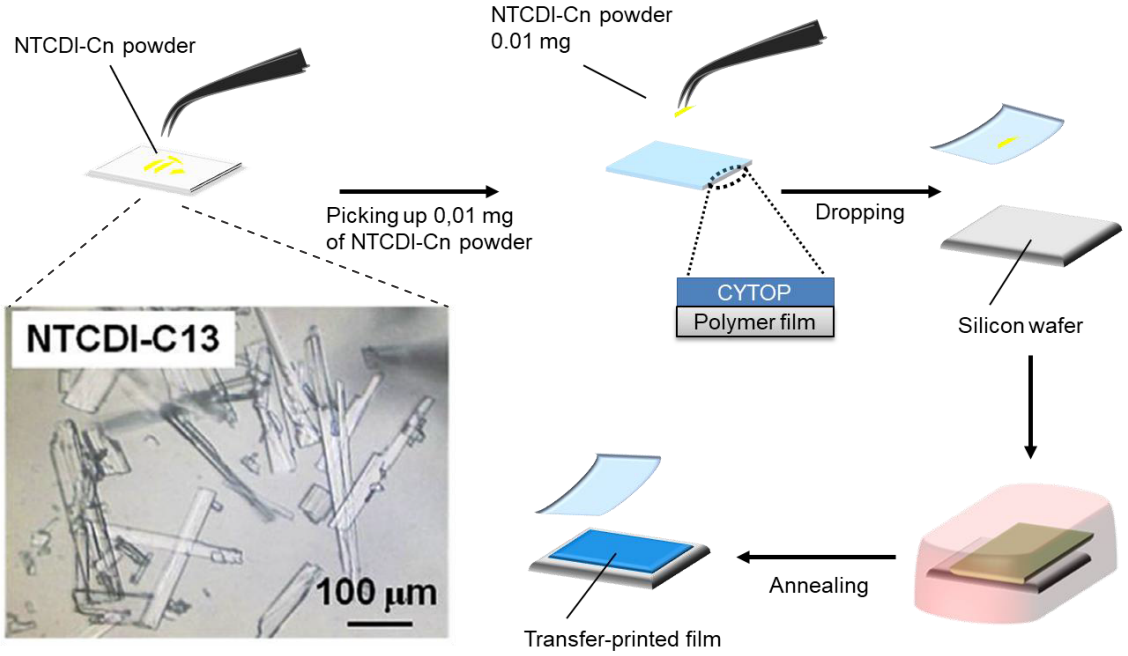

Fig. 2.6 Schematic illustration of all steps in the modified melt-printing technology.

2.2.6 Thermal Evaporation

Thermally evaporated films were also prepared on a heavily doped p-type silicon wafer with 200-nm-thick thermally grown SiO_2 as references. NTCDI-Cn derivatives were thermally evaporated at the rate of 0.03 nm/s onto the substrates at high vacuum (below 5×10^{-6} Torr). Unless there is no specific information, the thickness of the evaporated films is fixed to be 30 nm.

2.3 Characterization of the film

2.3.1 Atomic Force Microscope (AFM)

AFM is one of the most useful techniques to check the surface topology for various kinds of materials. This is sorted to be a type of scanning probe microscopy. Tiny sharp tips are used as a probe sensor approaching to the surface of samples at the certain frequency. The information about the surface morphology is gathered to a whole picture typically related to the height profile or the phase profile. Herein, the resolution of the image is reached to some order of a nanometer in height.

AFM (a Bruker scanning probe microscope (Dimension ICON PTX) was carried out to investigate the surface topology of the thin films made from NTCDI-C8, C13, and C15 at room temperature in air.

2.3.2 X-ray Diffraction

The X-ray diffraction (XRD) is a commonly used technique to estimate an atomic-scale structure for inorganic single crystalline[82]. This technique exploits the interaction of an incident beam and a sample in the path of the beam, resulting in periodic diffraction patterns at the detector. For example, single crystalline materials exhibits sharp X-ray diffracting profiles owing to the structural periodicity but amorphous materials or polycrystalline materials, which lack the periodicity, end up the appearance of broad peaks and/or halo patterns as a consequence of structural variations[83]. For the latter, gathering crystallographic information is, of course, not easy. Most of organic semiconductors are, in fact, known as polycrystalline materials, which produce the broad peaks, but XRD has been used as an effective tool to investigate their crystallographic information by estimating the *d*-spacing, the degree of orientation and the crystal size.

Our films are characterized with Rigaku rotaflex X-ray diffractometer with Cu-Kα radiation (154 pm). The *d*-spacing was determined by Bragg's equation (1):

$$n\lambda = 2d \sin\theta \qquad (2.1)$$

The crystallite size (*D*) was estimated by Scherrer's equation (2) in Ref. [84]:

$$D = \frac{0.89\,\lambda}{B_{1/2}\cos\theta} \qquad (2.2)$$

where θ, $B_{1/2}$, and λ are, respectively, the diffraction angle (θ) and the full width at half maximum of the diffraction peak, and the wavelength of the used X-ray.

2.3.3 Grazing-Incidence Wide-Angle X-ray Scattering (GI-WAXS)

Molecular orientations in the in-plane direction rather than the ones in the out-of-plane direction have been attracting attention to the research of OTFTs since they directly relate to the carrier transport; the transport from the source to the drain electrodes as illustrated in Fig. 1.4. Not like the common XRD technique, the GI-WAXS can detect crystallographic information in the in-plane direction which involve with π-π stacking of adjacent molecules on a substrate. In GI-WAXS, an incident X-ray beam passes the surface of a sample at a very shallow angle less than 0.2 degree and the incident beam scatters due to the interaction between the beam and the sample illustrated in Fig 2.7. By employing a 2D detector and analyzing the patterns gathered on the detector, we can estimate molecular orientation in the in-plane direction. Our films are also characterized with Rigaku SmartLab X-ray diffractometer[85] with Cu-Kα radiation (154 pm) to investigate the molecular orientations in the in-plane direction. In our experiment, the angle of the incident beam was fixed at 0.13 degree and the beam incidence was continued for 1 hour.

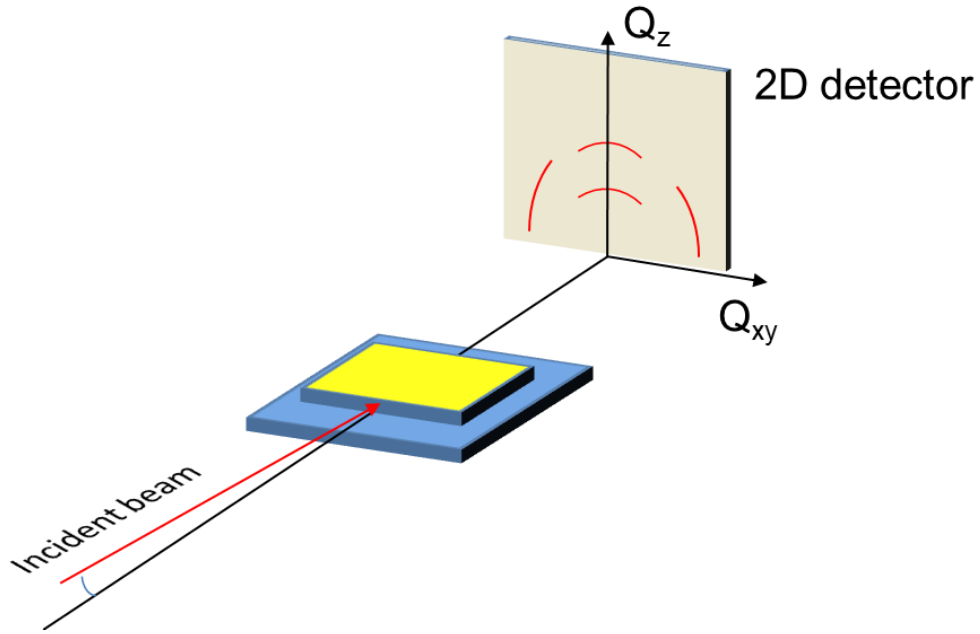

Fig. 2.7 Schematic illustration of GI-WAXS measurement. The yellow plate is a sample on a substrate.

2.4 Transistor Fabrication

2.4.1 Bottom Gate Top Contact

As mentioned in Chapter 1, the OTFT structures are divided into two widely used designs, i.e., the bottom contact (BC) structure and top contact (TC) structure. In the BC, the source and drain (S/D) electrodes are formed on the gate dielectric typically using photolithography and then the OSCs are deposited afterwards. A poor contact of the OSC thin-film and the S/D electrodes is problematic. On the other hand, the S/D electrodes are directly formed on the OSC film through a shadow mask in the TC. Moreover, the adjustment to place the S/D electrodes after the deposition is possible in the TC structure. Therefore, the TC structure is used in this work.

2.4.2 Source and Drain electrode

A 50 nm-thick layer of Au, for both the drain and source electrodes was thermally evaporated at 0.3 Å/s through a shadow mask on a NTCDI-Cn film in a vacuum. The design of the electrode pattern is shown in Fig. 2.8, where the length and width of the channels were 30, 50, or 100 μm and 2 mm, respectively. The structure of OTFTs is illustrated in Fig. 2.9. The capacitance of the gate dielectric was measured as 18 nF/cm^2. Nearly the entire surface of the gate dielectric was covered with thin films of NTCDI-Cn, whereas the large W/L ratio of 15 assures a negligible influence of the current flow on the outer sides of the electrodes.

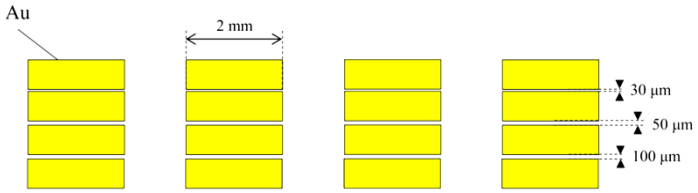

Fig. 2.8 Design for source and drain electrodes.

2.4.3 Electrical Property

The back side of the Si wafer was scratched with a sheet of sand-paper to remove naturally formed SiO_2 thin film. After attaching an aluminum plate to the back side by using conductive silver ink, the electrical conduction between the front and back of the Si wafer was confirmed. The circuit for measuring OTFTs was connected as illustrated in Fig. 2.9. The characteristics of OTFTs were determined by using an Agilent semiconductor parameter analyzer (B1500A) in the dark under vacuum to exclude the

influences of the illumination of light and exposure to oxygen and moisture. The I_D-V_D curves (V_G = 0–100 V) as a function of V_G (at V_G = 100) and the I_D-V_G curves (V_D = 100 V) as a function of V_D = 0, 20, 40, 60, 80, and 100 V were plotted.

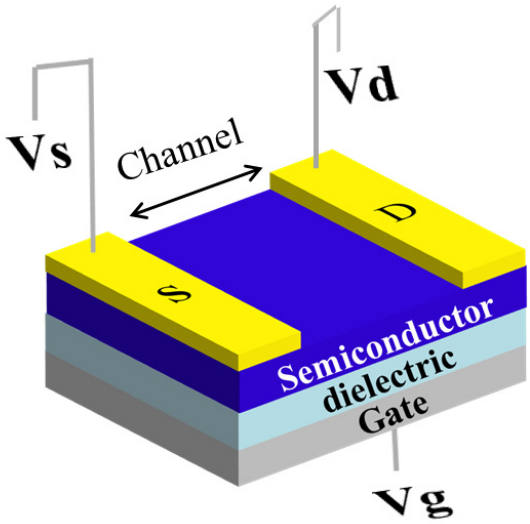

Fig. 2.9 Schematic illustration of measuring circuit.

The field-effect mobility (μ) and threshold voltage (V_{th}) of each device were extracted from square root plots of drain current (I_D) as a function of gate voltage (V_G) at a drain voltage (V_D) of 100 V using the following equation in the saturation regime:

$$I_{D,sat} = \frac{W\mu C_i}{2L}(V_G - V_{th})^2, \qquad (2.3)$$

where $I_{D,\,sat}$ is the I_D in the saturation regime at V_D = 100 V and C_i is the capacitance per unit area of the SiO_2 dielectric layer.

2.4.4 Extraction of resistance component

To extract the R_p and the channel resistivity, the Transfer Line Method (TLM)[38] was used according to the following steps through (a) to (d) in our research.

(a) Extracting R_t from the fitting line of the I_D-V_D characteristics in the range of 0-10 V

(b) Multiplying the channel width and R_t, resulting in R_tW

(c) Plotting R_tW versus the channel lengths

(d) Extracting the channel resistivity in the long channel length (L = 100 μm) from the slope of the fitting line and the total R_p from the y-intercept of the line.

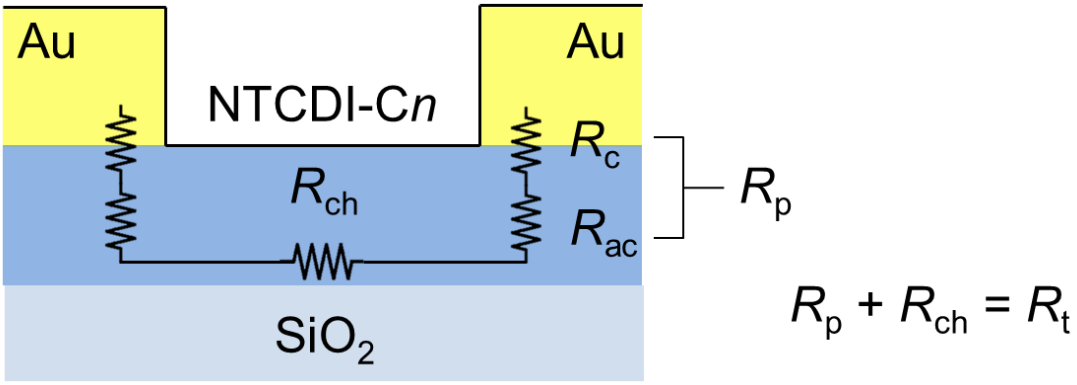

Fig. 2.9 Resistance components in a top contact structure.

Chapter 3

3. Melt-printing technology employing isotropic liquid phases

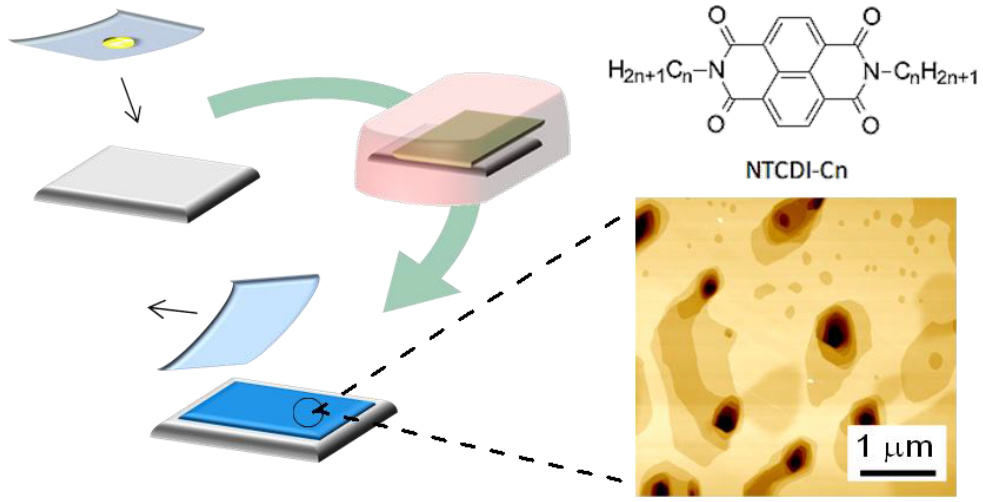

This chapter is adapted from the following publication:

Atsuro Ohyama, Jun Miyazawa, Yoichiro Yokota, Naoki Hirata, Naomi Oguma, Musubu Ichikawa, **Printing technology based on isotropic liquid phase of naphthalene diimide derivatives for n-type organic transistors**

This chapter is outlined as follows; firstly we take account to developing the melt-printing process. Secondly, the resulting melt-printed films are analyzed with AFM and XRD measurements to confirm molecularly flat surface with high crystallinity and the electrical properties of the films are compared with the one prepared by the thermal evaporation at last. Therefore, the optimization is completed in this chapter.

3.1 Introduction

Solution processes are well suited for large-scale production of thin films of organic active layers in transistors. However, environmentally hazardous chlorine-based solvents are usually required. In this chapter, we attempt to develop a new wet-process

approach, without the usage of toxic solvents for creating isotropic phases of NTCDI-C*n*. By sandwiching the molten between the melt-printing film and the substrate, the thin-films are spread under the film without evaporating to the air.

As a manufacturing process for OTFTs, the control of the resulting films is essential. Hereby, thin films of NTCDI-C13 are prepared to be the different thicknesses in the range of 50 nm to 200 nm. The dependence of the device performance on the thickness of the thin films is investigated by fabricating bottom gate top contact transistors. A maximum electron mobility of 0.38 cm^2/Vs was obtained from the 50-nm-thick NTCDI-C13 TFT, implying that making thin-films as thin as possible is better to enhance the injection of electrons. To gather more knowledge about this process, the NTCDI-C*n* with the different length of alkyl chains was melt-printed, and the performances were compared. All the devices of NTCDI-C*n* exhibited a relatively high electron mobility (~0.1 cm^2/Vs) but comparable differences were found out.

3.2 Results and Discussion

The key point for this process is the melting points of the OSCs and the transition from the IL to the LC. To spread the liquid under the melt-printing film and then form the thin-films. NTCDI-C*n* becomes an IL at relatively low temperatures of approximately 150–180 °C, as shown in Table 2.1. Although NTCDI-C*n* is inferior to PTCDI-C*n* in terms of electron affinity and extension of the π-electron system[19], NTCDI-C*n* is more favorable in terms of processing owing to the formation of their IL phases at fairly low temperatures. In the case of PTCDI-C*n*, they show only liquid crystal phases so that the high viscosity when annealing caused a poor coverage area not to form uniform films. Bottom-gate top-contact transistors were fabricated to evaluate the electrical characteristics of the melt-printed films. After the deposition of the semiconductors, Au as source and drain electrodes (50 nm thick), was evaporated through a shadow mask onto the film (Fig. 3(b)).

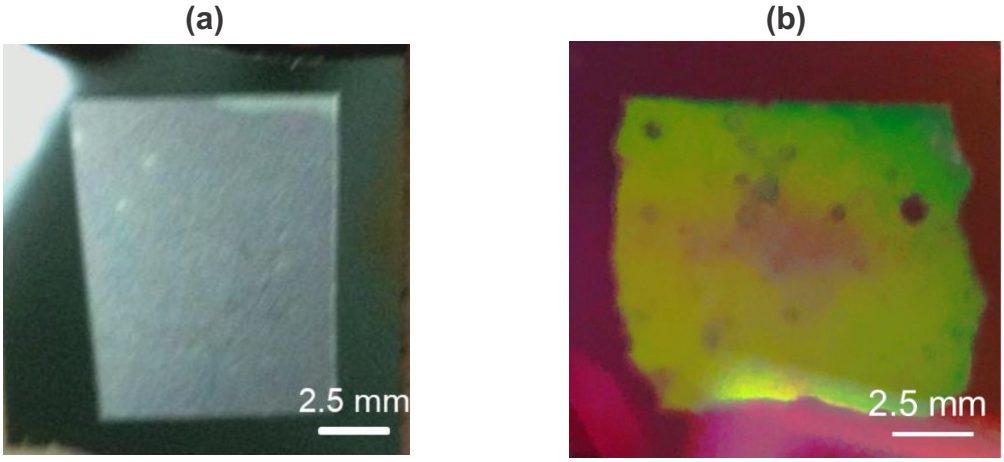

Fig. 3.1 Images of the NTCDI-C13 melt-printed films left on a silicon wafer before peeling off the melt-printing film (a) and after peeling off the melt-printing film (b).

3.2.1 Morphology and Crystallinity

Fig. 3.2(a) and (b) show the surface morphology of a thermally evaporated thin film and a melt-printed NTCDI-C13 thin film. Large and molecularly flat domains with steps can be seen. The step-terrace like surface morphology of the melt-printed film resembled that of thermal evaporation deposited films. Interestingly, the size of the grains in the melt-printed film was larger than of those in evaporated one. Therefore, the films prepared by this process might be preferable for transport of charge carriers in OTFTs. Although the melt-printed film seems to have deep holes, this effect is discussed at the next section. Fig. 3.2(c) shows X-ray diffraction (XRD) patterns of NTCDI-C13 films prepared by thermal evaporation and melt-printing. Progressive (00*l*) peaks up to the fifth order (005) appeared in the XRD pattern of the NTCDI-C13 film prepared by melt-printing, indicating that the film consisted of highly ordered crystalline layers. The *d*-spacing of the (00l) peak was 3.20 nm and corresponded to the step height exhibited on the surface of the thin film in Fig. 3.2(b) (i.e., 3.00 nm). This result suggests that NTCDI-C13 molecules in the film were oriented at *ca*. 52° normal to the substrate plane, although these molecules were oriented at *ca.* 49° in the evaporated film; both films featured a layer-by-layer structure, which is preferable for lateral carrier transport[21,28,80,86]. In addition, the extracted crystallite size *D* (150 nm) of the melt-printed film from Eq. (2.2) was considerably larger than that of the evaporated one

(30 nm)

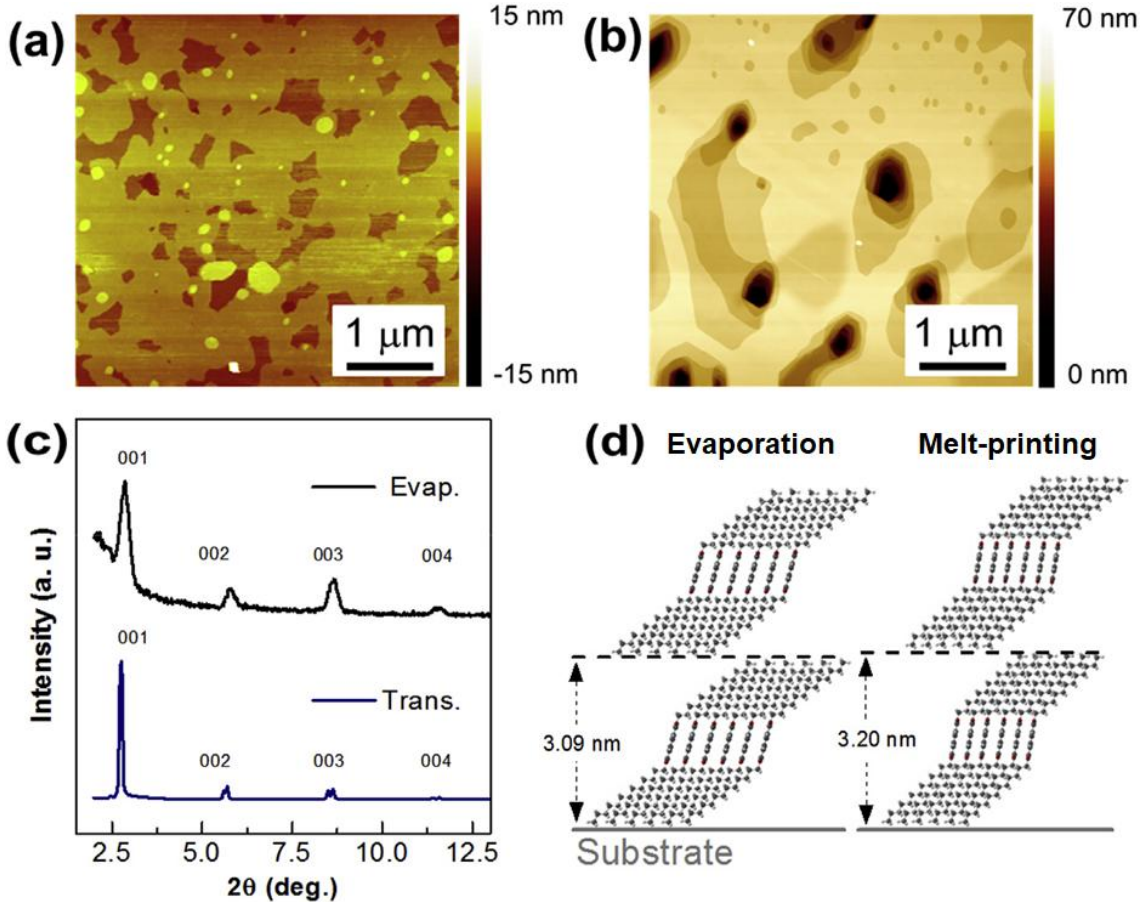

Fig. 3.2. Atomic force microscope (AFM) images of the surface topology of the NTCDI-C13 film; thermally evaporated (a) and melt-printed (b). (c) X-ray diffraction (XRD) patterns of NTCDI-C13 thin films prepared by thermal evaporation and melt-printing. (d) Presumed packing structures of NTCDI-C13 molecules in the evaporated film and the melt-printed film.

3.2.2 Electrical property

Fig. 3.3 shows the drain current (I_D) − gate voltage (V_G) and the drain current (I_D) − drain voltage (V_D) characteristics of the melt-printed and the thermal evaporated NTCDI-C13 TFTs. The TFTs exhibited typical *n*-type field-effect transistor behavior: the drain current positively increased as the gate voltage was positively increased. The electron mobility and threshold voltage of the melt-printed TFT were extracted from the square root of saturation I_D vs V_G relationship based on Eq. (2.3) to be 0.13 cm^2/Vs, which is relatively high for an n-type OTFT fabricated by solution-processing. However, this mobility is inferior to that of NTCDI-C13 OTFTs formed by evaporation methods[80].

The non-linearity of the I_D-V_D curves at the low V_D region below V_D = 20 V was observed in Fig 3.3(b) so that the large parasitic resistance between the contact and the channel existed in the melt-printed OTFTs. Therefore, the inferiority of mobility might be the result of poor carrier injection at the interface between the gold source electrode and the NTCDI-C13 semiconducting layer and/or the large access resistance because charge carriers must be transported in the vertical direction though the thick NTCDI-C13 layer, which has a thickness of approximately 200 nm.

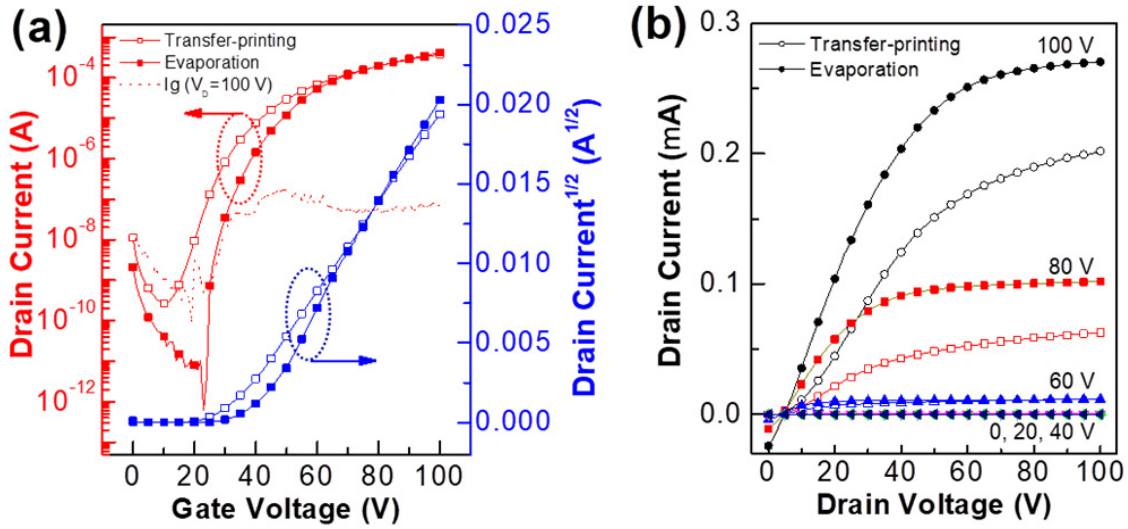

Fig. 3.3 (a) I_D-V_G characteristics obtained in the saturation regime (V_D = 100 V) for two OTFTs (L = 50 μm) with 200 nm of the OSC layer prepared by the melt-printing or 30 nm of the OSC layer prepared by thermal evaporation. The dotted line describes a typical gate leakage current (I_g) of the melt-printed NTCDI-C13 OTFT and (b) I_D-V_D characteristics obtained from the same OTFTs.

3.2.2.1 Effects of thickness

As mentioned above, a large resistance will limit performance of the NTCDI-C13 OTFTs. Hence, the thickness of the melt-printed films was optimized to decrease the resistance and improve performance. Fig. 3.4(a) shows the W/L normalized I_D-V_G characteristic obtained from a 30-nm-thick evaporated NTCDI-C13 TFT and a 50-nm-thick melt-printed NTCDI-C13 TFTs. Table 3.1 summarizes the important parameters of those devices. Note that the thickness of the semiconducting layer was varied by changing the amount of the suspension dropped onto the melt-printing film. The maximum mobility for each thickness of NTCDI-C13 increased remarkably from

0.11 cm^2/Vs for the 200-nm-thick device to 0.38 cm^2/Vs for the 50-nm-thick device; however, the threshold voltages changed only slightly. Here, parasitic resistances (R_p) arising from the contact electrodes for the devices with various NTCDI-C13 thicknesses were extracted by the standard transfer-length method (TLM)[38]. Fig. 3.5(b) shows the channel length dependences of the total resistances (R_t) of the devices with thicker NTCDI-C13 thickness, where R_t was estimated from the slope of I_D-V_D curve at V_G = 100 V in a small V_D region from 0 to 10 V. (Fig. 3.4(b)) The value of R_p, which should consist of the contact resistance (arising from the interface of the electrode and the semiconducting layer) and the access resistance (due to vertical transport of electrons through the semiconducting layer), was estimated from the intercept on the Y-axis, and the channel resistivity (R_{ch}) was extracted from the slope of the channel length dependence of R_t. Although R_p for the 80-nm-thick NTCDI-C13 device was 28.0 kΩ cm, R_p of 17.4 kΩ cm for the 50-nm-thick device decreased and was comparably small as that of the thermally deposited device with the 30-nm-thick NTCDI-C13 layer, as shown in the figure and Table 3.2. Non-linear behavior of the I_D-V_D curves in the small V_D region was improved when the thickness was decreased from 200 nm, as shown in Fig. 3.4(b). These findings indicate that the access resistance in R_p caused non-linear behavior and the lower electron mobility of the devices with thicker NTCDI-C13 layers. Notably, R_{ch} increased as the NTCDI-C13 thickness decreased from 80 to 50 nm. However, the channel layer, through which electrons pass, should be a few nanometers in thickness[47,87], and R_{ch} should be independent of the thickness of the channel layer. A possible reason for this effect is the presence of defective holes observed in AFM images, as shown in Fig. 3.2. If the bottom of the holes reached into the channel layer or to the SiO_2 dielectric layer, this could degrade the transport of charge carriers in the channel. A relatively high gate leakage current was observed in the I_D-V_D curves at V_G = 0 V. However, silicon substrates with 200-nm-thick have been used as the gate dielectric for both devices by thermal evaporation and melt-printing so that the leakage currents for all the devices are probably in the same level. Thus, in spite of the gate current, we think that the discussion about the resistances is reliable.

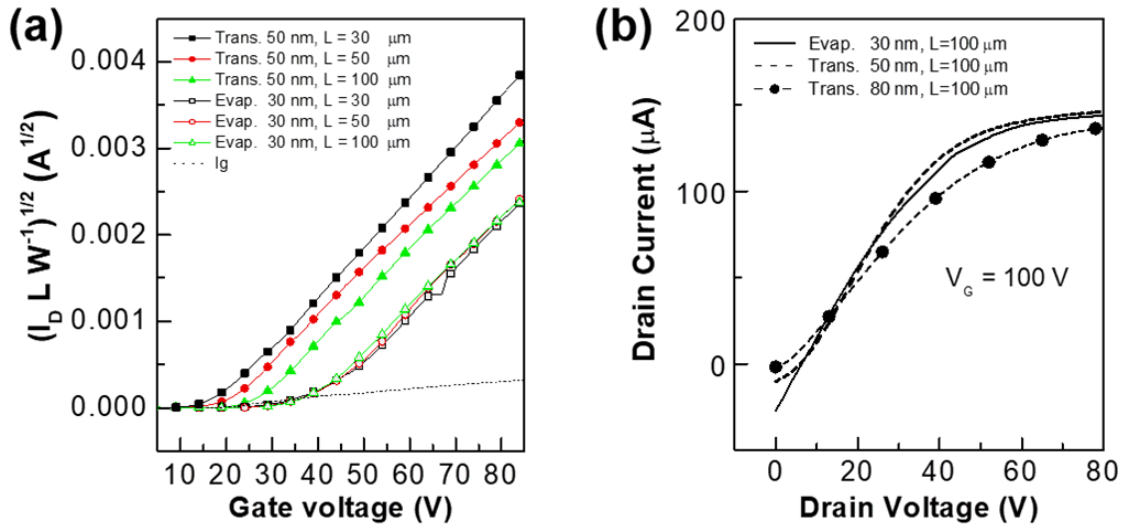

Fig. 3.4 (a) Square root plot of *W*/*L* normalized I_D-V_G characteristics obtained in the saturation regime (V_D = 100 V) for two OTFTs with 50-nm-thick melt-printed and 30-nm-thick evaporated NTCDI-C13 films. The dotted line describes typical gate leakage current (*I*g) obtained from the melt-printed NTCDI-C13 OTFT. (b) I_D-V_D characteristics at V_G=100 V obtained from the three OTFTs with 50-and 80- nm-thick NTCDI-C13 layers prepared by melt-printing and a 30-nm-thick NTCDI-C13 layer prepared by thermal evaporation.

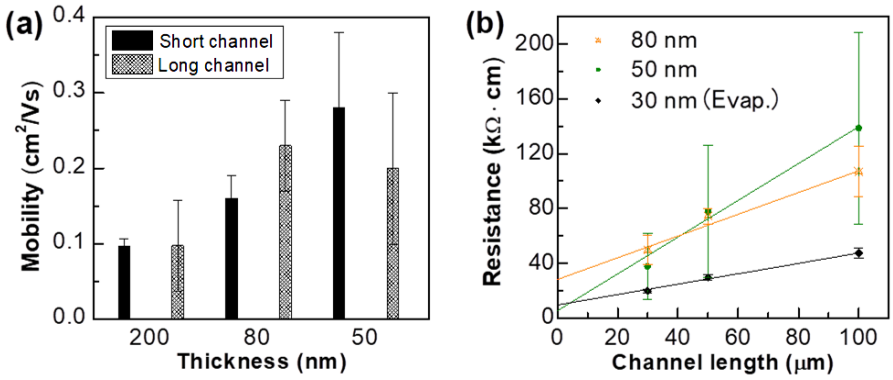

Fig. 3.5 Extracted mobility values (a), and total resistance values with channel lengths from 30 to 100 μm (b) as a function of the thickness for NTCDI-C13 OTFTs.

Table 3.1 Transistor characteristics of melt-printed NTCDI-C13 OTFTs, with short, medium and long channel lengths and three different active layer thicknesses from 200 to 80 and a 30-nm-thick evaporated NTCDI-C13 OTFT with a long channel length. Ion/Ioff is the ratio between I_D at V_G=100 V (I_{on}) and 0 V (I_{off}) for the same V_D of 100 V. Subthreshold slope (*SS*) is extracted from the steepest slope of the log I_D vs V_G relationship.

Thickness (nm)	*L* (μm)	μ_{ave} (cm^2/Vs)	μ_{max} (cm^2/Vs)	V_{th} (V)	I_{on}/I_{off}	*SS* (V/dec)
200	30	$(9.7 \pm 1) \times 10^{-2}$	0.11	12 ± 4	6.0×10^6	2.8
	50	$(9.1 \pm 2) \times 10^{-2}$	0.12	14 ± 8	3.3×10^6	3.1
	100	$(9.8 \pm 6) \times 10^{-2}$	0.17	6.9 ± 11	3.6×10^5	1.8
80	30	$(1.6 \pm 0.3) \times 10^{-1}$	0.18	6.0 ± 3	1.4×10^6	2.1
	50	$(1.3 \pm 0.05) \times 10^{-1}$	0.14	15 ± 5	8.6×10^5	3.1
	100	$(2.3 \pm 0.6) \times 10^{-1}$	0.27	1.8 ± 0.4	2.2×10^6	1.9
50	30	$(2.8 \pm 0.1) \times 10^{-1}$	0.38	15 ± 5	1.3×10^6	3.7
	50	$(1.8 \pm 0.1) \times 10^{-1}$	0.18	14 ± 4	7.7×10^5	4.2
	100	$(2.0 \pm 0.1) \times 10^{-1}$	0.27	16 ± 10	2.1×10^6	2.3
30[18]	100	$(4.2 \pm 0.4) \times 10^{-1}$	-	39 ± 2	9.0×10^4	-

Table 3.2 Extracted values of the parasitic resistances and the channel resistances for the melt-printed and thermally evaporated NTCDI-C13 TFTs with various thicknesses of C13 layers.

	Thickness (nm)	R_p (kΩ·cm)	R_{ch} (MΩ·cm)
Melt-printing	50	17.4	2.42
	80	28.0	1.59
Evaporation	30	7.75	0.81

3.2.2.2 Effect of alkyl Lengths

NTCDI with shorter and longer alkyl lengths than NTCDI-C13: NTCDI-C8 and -C15 were used to further investigate this processing technique. The melting points of C8 and C15 are, respectively, 185.1 and 156.2 °C, and are higher and slightly lower than that of C13 (see Table 2.1). Fig. 3.6(a) and (b) also show the surface morphology of the

surfaces of NTCDI-C8 and -C15 thin films prepared by melt-printing. The surfaces were very similar to that of the melt-printed NTCDI-C13 thin film. The XRD patterns, shown in Fig. 3.6(c), respectively gave estimated *d*-spacings of 2.40 (NTCDI-C8) and 3.70 nm (NTCDI-C15), which corresponded to the step-terrace-heights of 2.35 and 3.70 nm appearing in the surface morphologies, as shown in Fig. 3.6(a) and (b). Therefore, NTCDI-C8 and -C15 molecules aligned in the melt-printed thin-films in a similar way to those in NTCDI-C13 (slant edge-on alignment on the silicon substrates). Table 3.3 summarizes the electrical parameters obtained from melt-printed NTCDI-C*n* OTFT devices. NTCDI-C8 TFTs showed much poorer performance than the others. This finding is consistent with previously reported results for spin-coated and thermally-deposited NTCDI-C*n* TFTs. NTCDIs with longer alkyl chains tend to exhibit higher electron mobility[28,80]. NTCDI-C15 and -C13 showed a similar electron mobility of 0.1 cm^2/Vs except for a NTCDI-C15 device with the longer channel (100 μm). One possible reason for the low mobility in the NTCDI-C15 device with the 100-μm-long channel is the high viscosity of molten NTCDI-C15 due to its large molecular size. This effect might lead to defects in the thin films of NTCDI-C15 because of the poorer spread of the melt in melt-printing. The differences in crystallite size and performance of the OTFTs indicated that C13 was the most suitable molecule for this process.

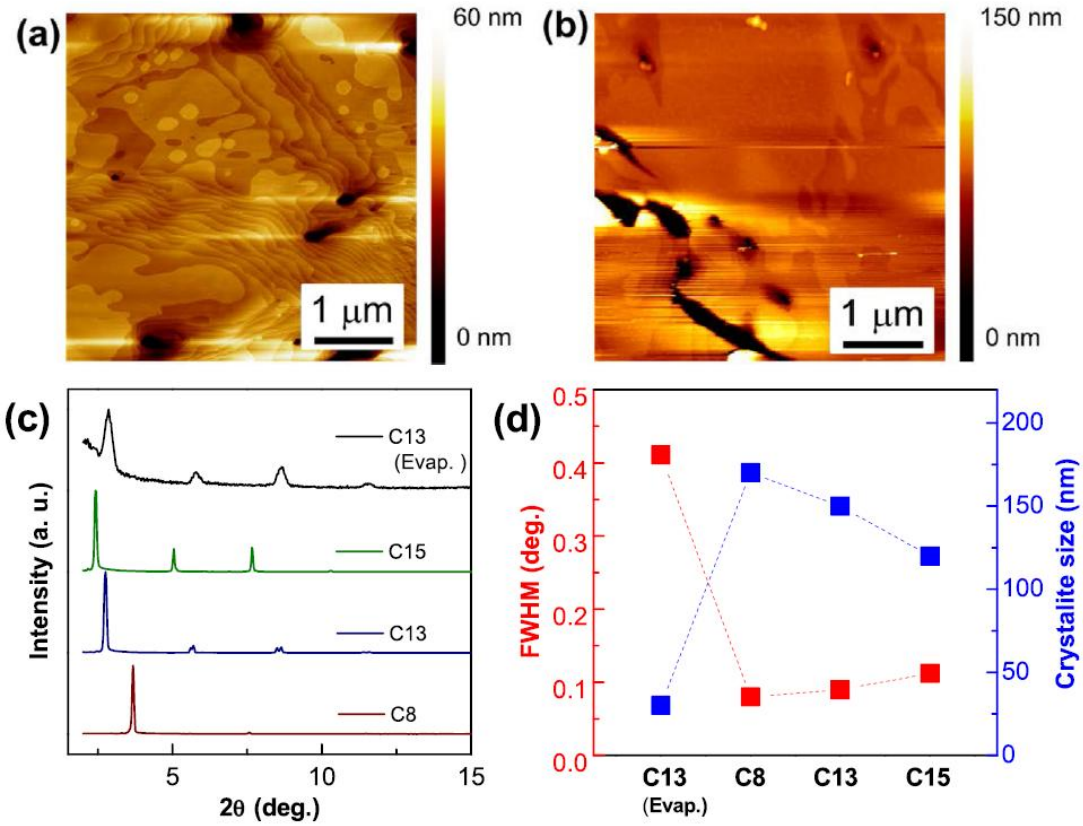

Fig. 3.6 AFM images of the surface topology of the NTCDI-C8 (a) and -C15 (b) films prepared by the melt-printing process. (c) X-ray diffraction (XRD) patterns of NTCDI-C*n* thin films prepared by thermal evaporation or melt-printing and (d) FWHM and crystallite size *D* extracted from the (001) peaks in the XRD patterns. Dotted lines in the panel (d) are guides to the eye.

Table 3.3 NTCDI-C*n* transistor characteristics for short and long channel lengths.

NTCDI-	L (μm)	μ_{ave} (cm^2/Vs)	μ_{max} (cm^2/Vs)	V_{th} (V)
C8	30	$(3.0 \pm 3) \times 10^{-2}$	0.017	20 ± 4
	100	$(5.5 \pm 5) \times 10^{-2}$	0.078	32 ± 4
C13	30	$(9.7 \pm 1) \times 10^{-2}$	0.11	12 ± 4
	100	$(9.8 \pm 6) \times 10^{-2}$	0.17	6.9 ± 11
C15	30	$(9.8 \pm 2) \times 10^{-2}$	0.11	25 ± 2
	100	$(1.5 \pm 1) \times 10^{-2}$	0.028	27 ± 7

3.3 Conclusion

In this chapter, we demonstrate a new wet process for preparing thin-films of OSCs based on OSC suspensions, which is named “a melt-printing process.” The thin films consisting of OSCs, prepared from a suspension, are annealed at a temperature higher than their melting points, between the substrate and a plastic film with a solvent repellent finish. During annealing, the OSC solid melts and flows before crystallizing on cooling. The number of OSC small particles should decrease, resulting in fewer grain boundaries in the OSC thin-films. The thin-films prepared by melt-printing consisted of significantly enlarged grains with high crystallinity, which were preferable for carrier transportation. The thickness of the melt-printed thin films could be varied from 50 to 200 nm by controlling the amount of NTCDI-C*n* suspension dropped on the printing film. The maximum electron mobility of 0.38 cm^2/Vs was obtained from the 50-nm-thick NTCDI-C13 TFT because thicker NTCDI-C*n* layers increased parasitic resistance of the devices. A comparison of the TFT performances for the NTCDI-C13 and -C15 devices suggests that the viscosity of molten NTCDI-C*n* is important for preparing well-spread thin-films. This study demonstrates the great potential of this process for environmentally friendly fabrication of organic semiconductor thin-films.

Chapter 4

4. Melt-printing technology towards solvent-free

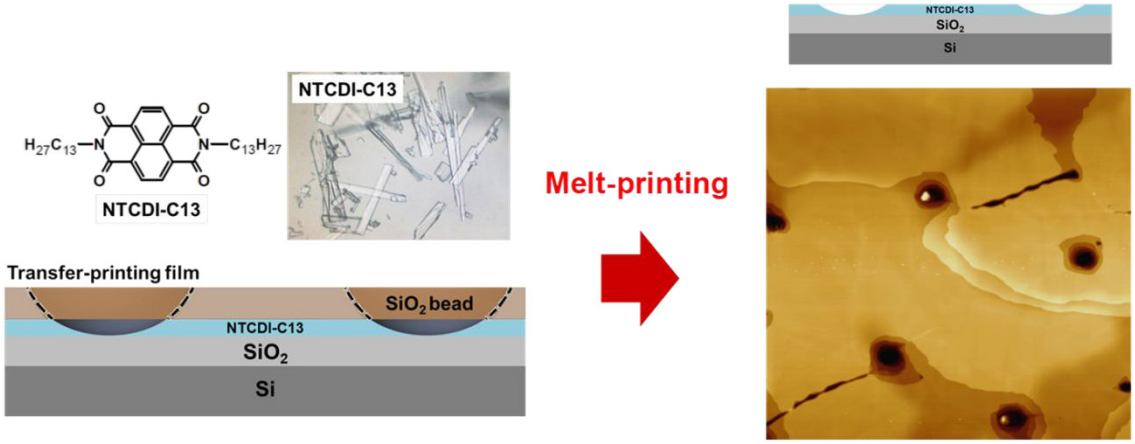

This chapter is adapted from the following publication

Atsuro Ohyama, Naoki Hirata, Naomi Oguma, Musubu Ichikawa

Solvent-free printing process for organic transistors using a naphthalene diimide bearing long alkyl chains

This chapter is outlined as the follows; firstly we prepare melt-printed films by using a NTCDI-C13 powder instead of the suspension, followed by AFM and XRD measurements to check the quality of the resulting films as well as the electrical measurements to compare their performances to the ones prepared by the thermal evaporation and the melt-printing process with the suspension. Finally, we clarify the mechanism of this technology in more details.

4.1 Introduction

Coating and printing technologies are important to realize the production of easy and low-cost printed electronics based on organic thin-film transistors (OTFTs)[29,67,88–91]. However, the usage of organic solvents to dissolve or disperse organic semiconductors (OSCs) is always arguable for the following reasons; the presence of the trace impurities in organic solvents and the vacancies induced by solvent evaporation that may cause severe non-uniformity of the resulting active layer. The consistent device

performance from solution-processed devices is not reasonable[92,93]. Moreover, popular chlorine-based solvents—which are often used for OSCs with low solubility—are hazardous to ecology and human health. In the previous chapter, we suggested that use a new approach to melt OSCs and to spread the molten between the printing film and the substrate. Molecularly smooth organic thin-films with high crystallinity were successfully exhibited. However, we still exploited IPA as the poor solvent to prepare the OSC suspension and ideally any solvents do not have to be included in the process.

In this chapter, we aim to modifying the melt-printing technology to prepare melt-printed thin-films with the same quality but without using any solvents. The main concepts of this approach are to remove IPA used to prepare the suspension and to directly melt-print OSC powder onto a substrate. Unlike our previous process, this approach can be regarded as dry processing rather than wet processing. In addition, the approach developed here allows the use of a very small amount of OSC powder (less than 0.01 mg) to cover an area of ca. 1 cm^2 with a thickness of several tens of nanometers on a silicon (Si) substrate and employs all the powder in the thin film. We prove the ability of this solvent-free melt-printing process to provide high-quality OSC thin films for OTFTs with efficient material usage.

4.2 Results and discussion

4.2.1 Material Consumption Efficiency

Figure 4.1 presents a photograph of a powder melt-printed C13 thin film. We can observe a few large defects, but the thin film was reasonably uniform and almost the same shape as the printing film, as was the case for the previously reported thin films obtained by the suspension printing. The area and thickness of the thin film were ca. 1 cm^2 and 80 nm, respectively, and the calculated amount of C13 in the thin film was almost the same (90%) of the amount of C13 powder (less than 0.01 mg) initially loaded on the printing film. This finding proves that the powder melt-printing process uses the material efficiently. Due to such a small amount, the precise measurement of the weight for the powder is not feasible therefore we simply took a large amount of the powder to be 0.1 mg, divided it into 10 pieces manually, and
used them for ten substrates.

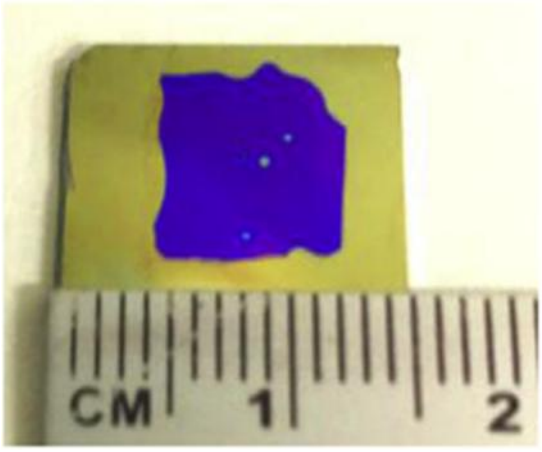

Fig. 4.1 Overview picture of a powder melt-printed C13 film prepared on a Si substrate just after peeling off the printing film.

4.2.2 Surface Morphology and Crystallinity

Fig. 4.2(a) and (b) show the surface morphologies of suspension and powder melt-printed C13 films, respectively, along with corresponding cross-section profiles for the white lines in the images. The crystalline domains showed step and terrace structures similar to those observed in our previous report[94], and the step height was 3.2–3.3 nm. In our previous work, the melt-printed films contained many deep holes. Fig. 4.2(b) shows that similar deep holes were also observed in this work. There seemed to be five to ten deep holes per 5 × 5 μm square region of the thin films. The origin of these defects is fully detailed in the next section.

Fig. 4.3(a) shows X-ray diffraction (XRD) patterns of thermally evaporated and melt-printed C13 films measured with the Rigaku Rotaflex X-ray diffractometer. The *d*-spacing of the (001) peak at 2.80° was 3.15 nm and corresponded to the step heights of 3.2 to 3.3 nm measured in the cross-section profiles of the AFM images, indicating that the π-conjugated skeletons of the C13 molecules stood up on the substrate, as previously reported for the film obtained from suspension melt-printing[94]. This orientation of C13 molecules is favorable for transporting carriers in OTFT configurations[21,28,80,86,94]. Progressive (00*l*) peaks up to the sixth order (006) (only until (003) shown in the chart) revealed the films consisted of highly ordered layer-by-layer structures. The FWHM of the (001) diffraction peak for the powder melt-printed film was slightly narrower than that of suspension melt-printed film, as shown in Fig. 4.3(b).

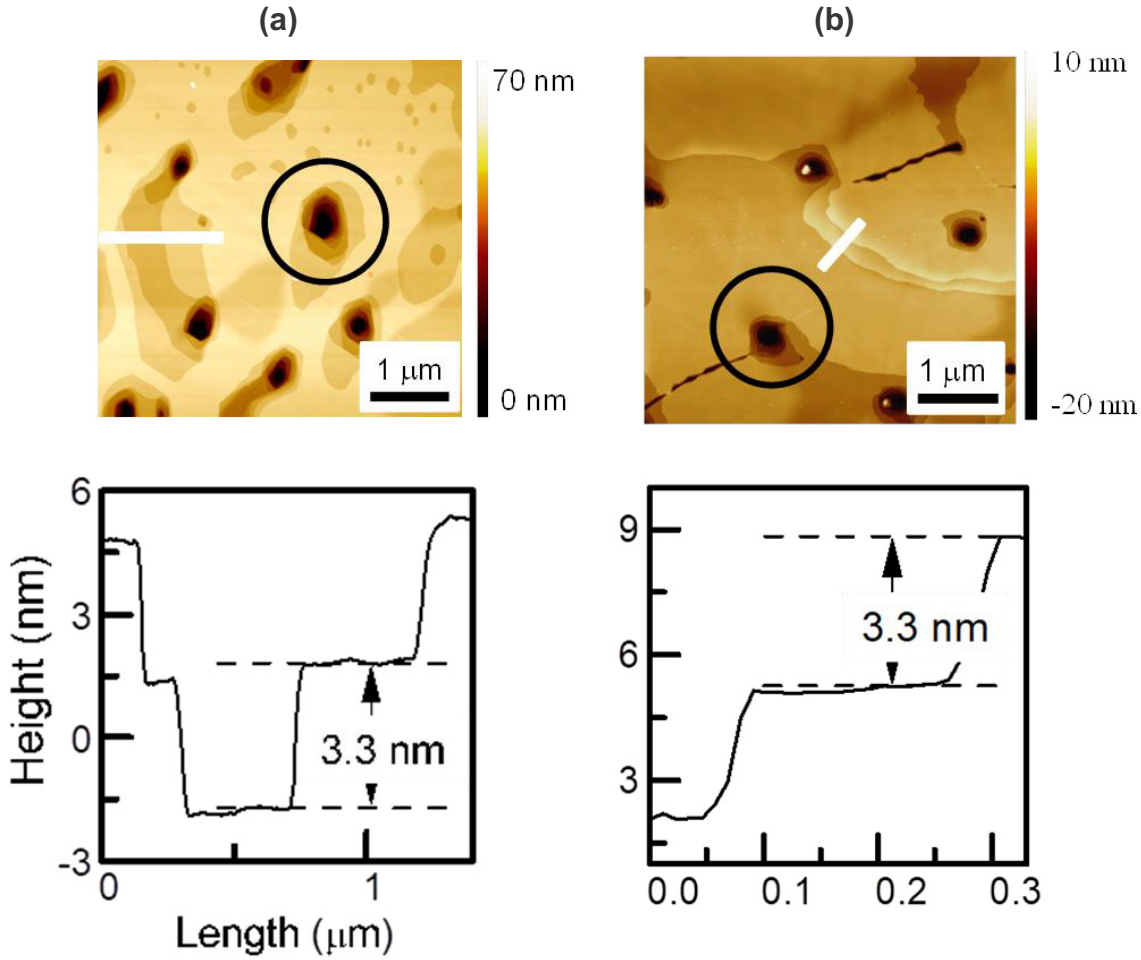

Fig. 4.2 AFM images of melt-printed C13 films and the cross-section profiles for the corresponding white lines drawn in the images. Suspension (a) and powder (b) printing films.

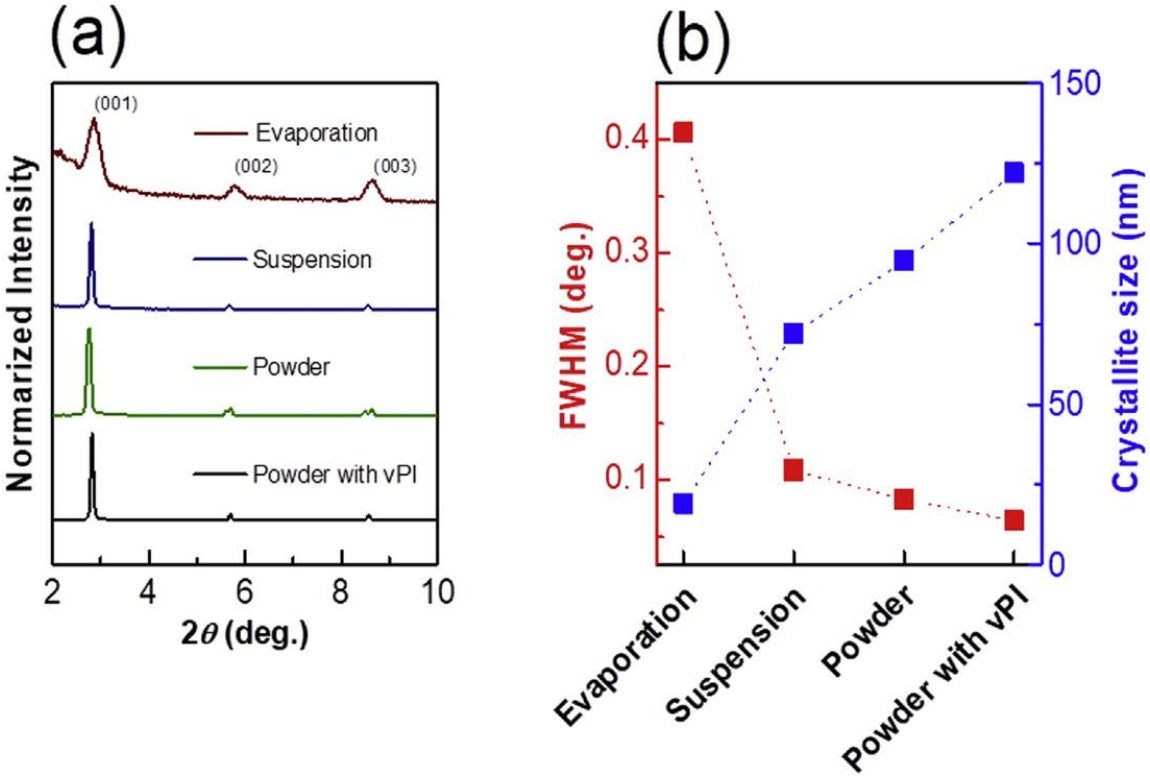

Fig. 4.3 (a) XRD patterns of C13 thin films prepared by thermal evaporation or melt-printing. (b) FWHM and crystallite size D extracted from the (001) peaks in the XRD patterns.

4.2.3 Electrical property

The I_D–V_G and I_D–V_D characteristics were measured from the devices shown in Fig. 4.4.

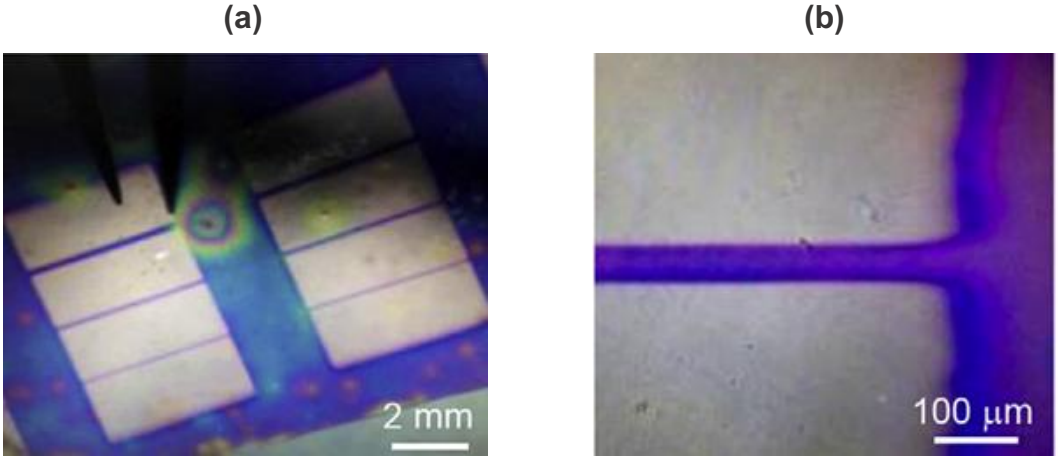

Fig. 4.4 (a) and (b) Microscope images of the C13 TFTs completed with the thermal evaporation of gold layers as source and drain electrodes.

Fig. 4.5 shows the I_D–V_G and I_D–V_D characteristics of thermally evaporated and powder

melt-printed C13 OTFTs with a channel length of 100 μm. The powder melt-printed OTFT exhibited comparable characteristics to those of the devices with thermally evaporated C13 films. This means that C13 thin films fabricated by powder melt-printing possess comparable quality to those prepared by thermal evaporation. An apparent difference between the thermally evaporated and melt-printed films was the large hysteresis between the forward and backward sweeps in the I_D–V_G characteristics for the melt-printed films. This might result from impurities, disorder of the semiconductor layers, and/or carrier traps at the interface between the semiconductor and dielectric layers. Trapped carriers in the dielectric layer also cause the hysteresis[95]. Note that annealing organic thin films at a suitable temperature after the preparation is useful for enhancing crystallinity and OTFT performances. However, in the case of thermally evaporated NTCDI-C*n* films, annealed OTFTs have exhibited inferior mobilities[80]. Therefore, we employed no annealing OTFTs as comparative objects in this research.

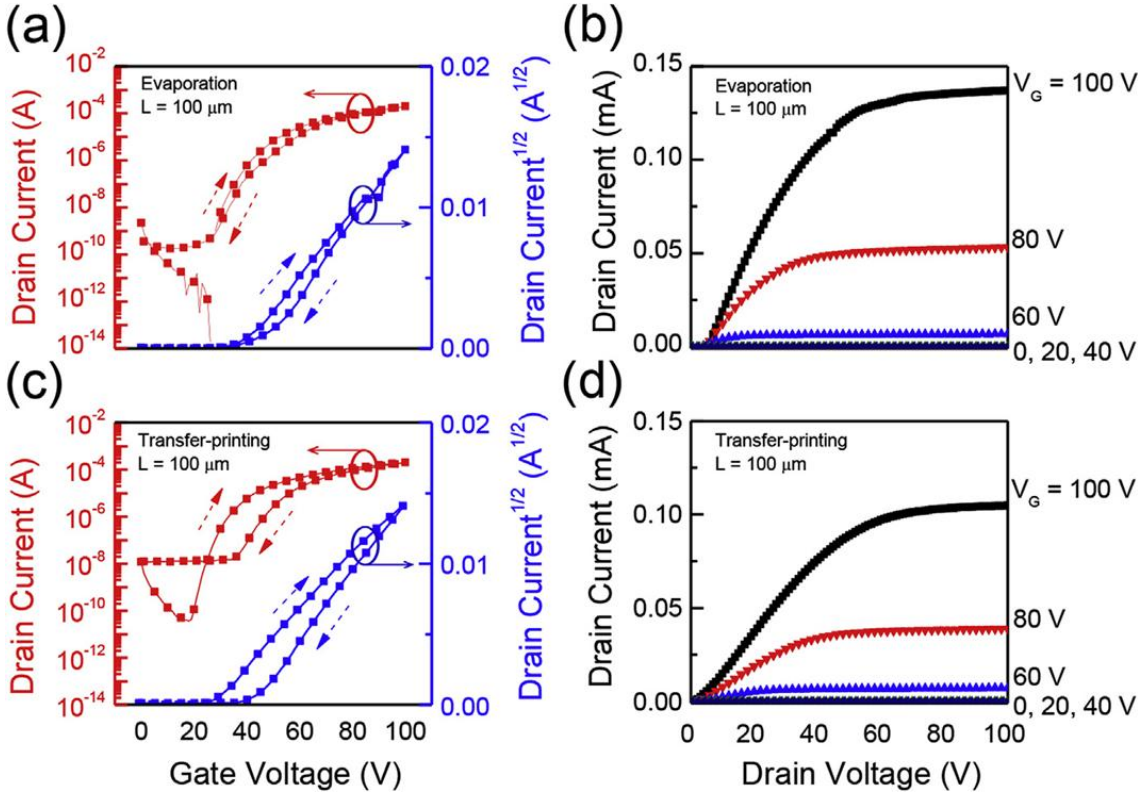

Fig. 4.5. I_D–V_G (V_D=100 V) and I_D–V_D characteristics of OTFTs (L=100 μm) with 30-nm-thick thermally evaporated (a, c) and 80-nm-thick melt-printed (b, d) C13 thin-films.

Finally, we discuss the dependence of powder melt-printed OTFTs on channel length and propose a mechanism for the influence of the SiO_2 beads and resulting holes in the semiconducting layer. The performance of the powder melt-printed OTFTs exhibited channel-length dependence, as seen in Fig. 4.6, whereas the evaporated OTFTs did not. Fig. 4.6 summarizes the μ, V_{th}, and normalized resistance ($R_t\ W\ L^{-1}$) characteristics of the 12 melt-printed C13 OTFTs with different channel lengths, where R_t was defined as the resistance obtained from the slope of I_D–V_D (V_G = 100 V) at low V_D (from 0 to 10 V). In general, μ of OTFTs becomes larger with increasing channel length because of the contact resistances between the source/drain electrodes and semiconductor layer; however, our OTFTs displayed the opposite tendency. The highest μ of 0.32 cm^2/Vs was obtained for the device with the shortest channel, and the lowest μ was exhibited by the device with the longest channel. The comparison of $R_t\ W\ L^{-1}$ values in Fig. 4.7(c) revealed that the channel resistance was higher for the OTFTs with longer channels, which was probably caused by the many deep holes in the C13 thin films, as shown in Fig. 4.2. In addition, boundaries or cracks (line defects) were seen around the deep holes in the printed films. The deep holes and line defects probably degrade the charge carrier transport in the melt-printed C13 layers. Not surprisingly, our interest was shifted towards the origin of these defects, leading us to investigate the printing film for deeply understanding the mechanism of the technology from the following section.

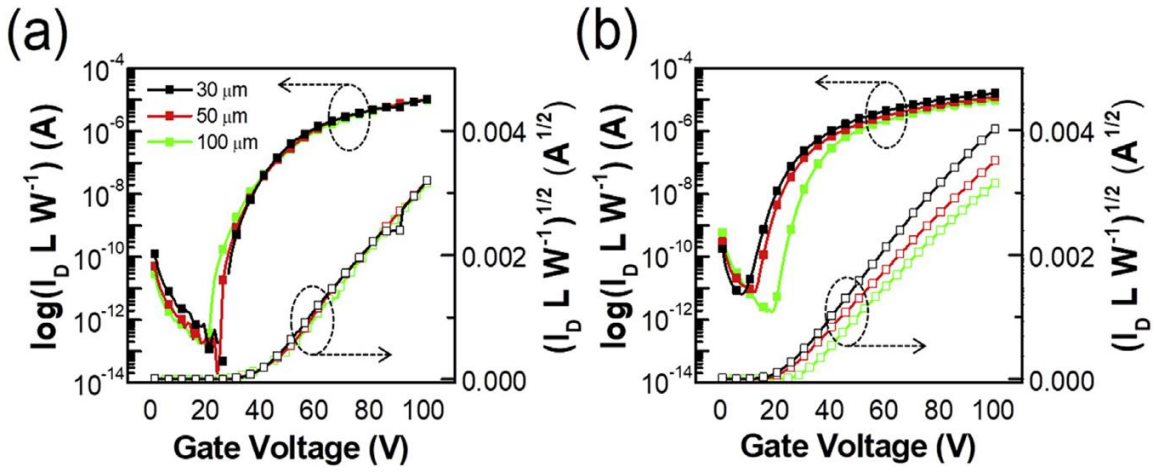

Fig. 4.6. *W*/*L* normalized I_D−V_G characteristics (V_D=100 V) of 30-nm-thick thermally evaporated (a) and 80-nm-thick melt-printed (b) TFTs with different channel lengths.

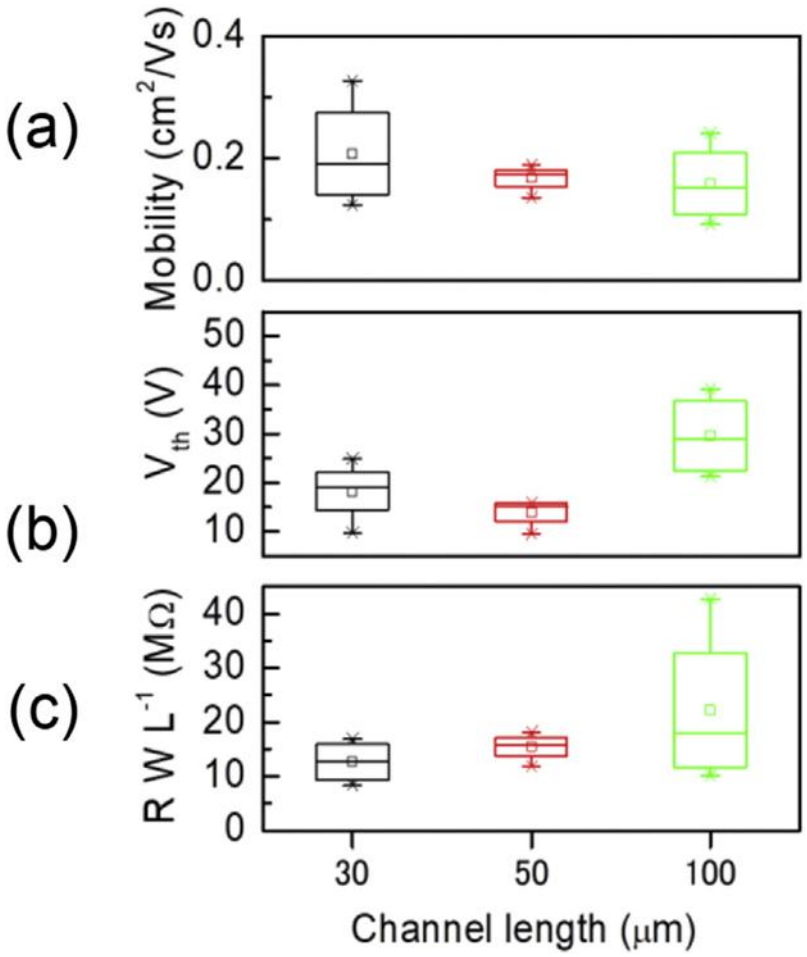

Fig. 4.7. Boxplots of the statistical comparison for the devices with different channel lengths from 30 to 100 μm in the melt-printed C13 TFTs; (a) mobility, (b) threshold voltage (V_{th}), (c) R_t W L−1.

4.2.4 Mechanism

At first, we carefully investigated the surface topology of the printing film which completed with the surface treatment and found many random bumps on the film, as shown in Fig. 4.8(a). The surface of the printing film contained hemispherical bumps with a height of approximately 20–50 nm and a diameter of 200 nm. Hereby, these bumps seemed to be corresponding with holes existing on the melt-printed films. After O_2 plasma treatment for 5 min, the number of bumps increased and their height increased to up to 120 nm, as shown in Fig. 4.8(b).

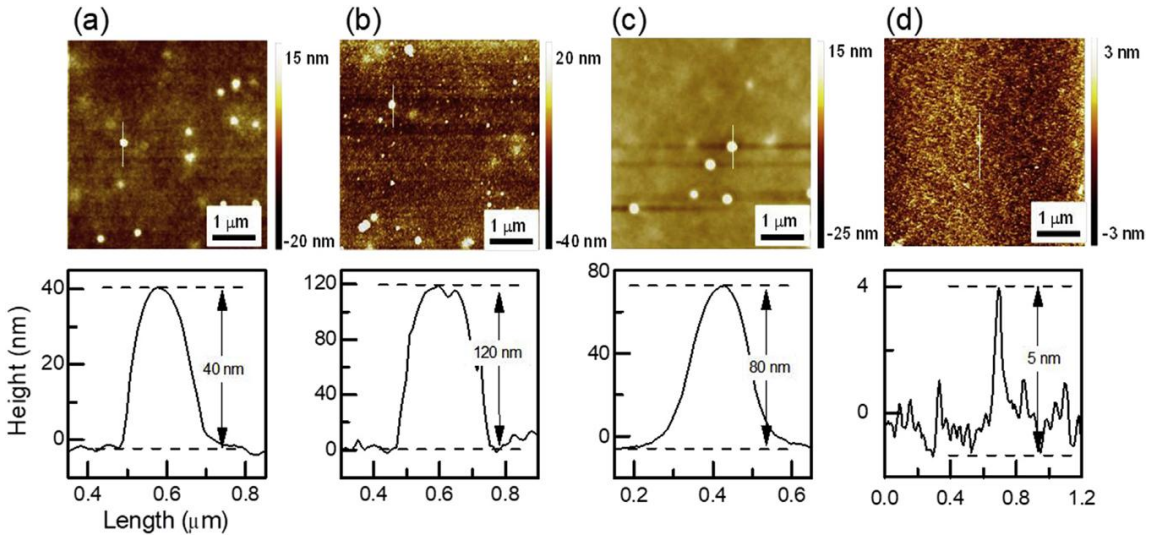

Fig. 4.8 AFM images of printing films and the cross-section profiles for the corresponding white lines in the images with different treatments; (a) pristine (cleaning with IPA), (b) plasma treatment for 5 min in an oxygen atmosphere, (c) finishing surface treatment with 10% CYTOP solution. (d) The surface morphology of vPI.

According to the manufacturer, the PI films contain SiO_2 beads to aid their efficient mass production, as illustrated in Fig. 4.9. This information is consistent with our images of the surfaces of the PI films in Fig. 4.8(a) and (b) since the surface of the polyimide was etched by the oxygen plasma whereas no influences occurred to the Si beads. More importantly, even after treating a pristine or O_2 plasma-treated PI film with 10% CYTOP solution (AGC), the bumps still influenced the surface morphology of the printing film (Fig. 4.8(c)). As shown in Fig. 4.8(d), no such bumps were observed on the surface of the vPI which was made at our laboratory with no addition of the Si beads to

the vanish. Fig. 4.10 shows the surface morphology of a powder melt-printed film of C13 obtained using a vPI-based printing film. This C13 film had no apparent deep holes in its surface, showing the strict step terrace structure. Therefore, we concluded that the bumps on the printing film and the deep holes in the melt-printed films resulted from the SiO_2 beads present in the commercial PI films. Note that the SiO_2 beads functioned as spacers between the surfaces of the substrate and PI film so that the thickness of the melt-printed film could be controlled simply by adjusting the time of the oxygen plasma and controlling the amount of loaded powder. For example, the oxygen plasma treatment for 1 min and 2 min on the commercial PI film can produce the 30-nm-thick and the 50-nm-thick melt-printed film, respectively.

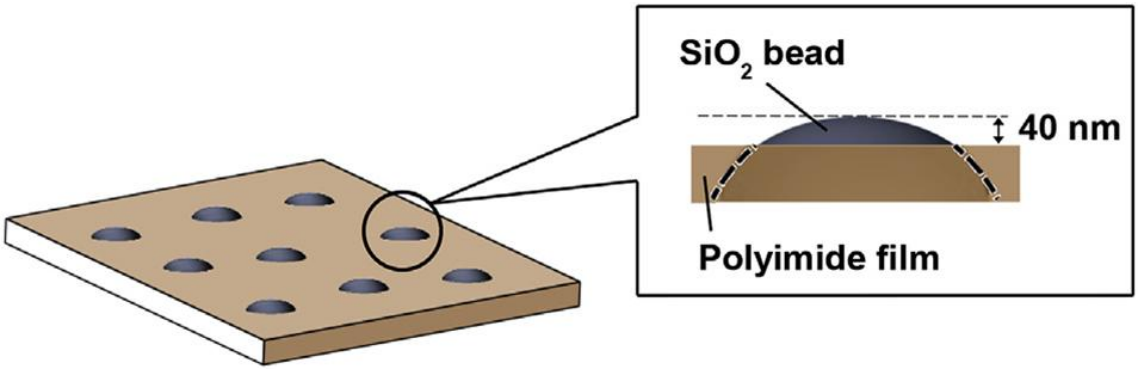

Fig. 4.9 Overview illustration of the cross-section of the printing film.

The melt-printed film prepared using vPI showed the smallest FWHM (largest crystallite size) among the samples (Fig. 4.3). The beads may induce disorders in the molecular alignment in adjacent regions of the resulting thin films. Consequently, the vPI film may be the best printing film from the viewpoint of crystalline quality of the resulting printed films. However, the larger thickness (>200 nm) of the C13 films printed using vPI might contribute to their larger crystallite size than that of the thinner (80 nm) C13 films fabricated with commercial PI films. In addition, using vPI also caused poor coverage of C13 because C13 did not spread as effectively during annealing.

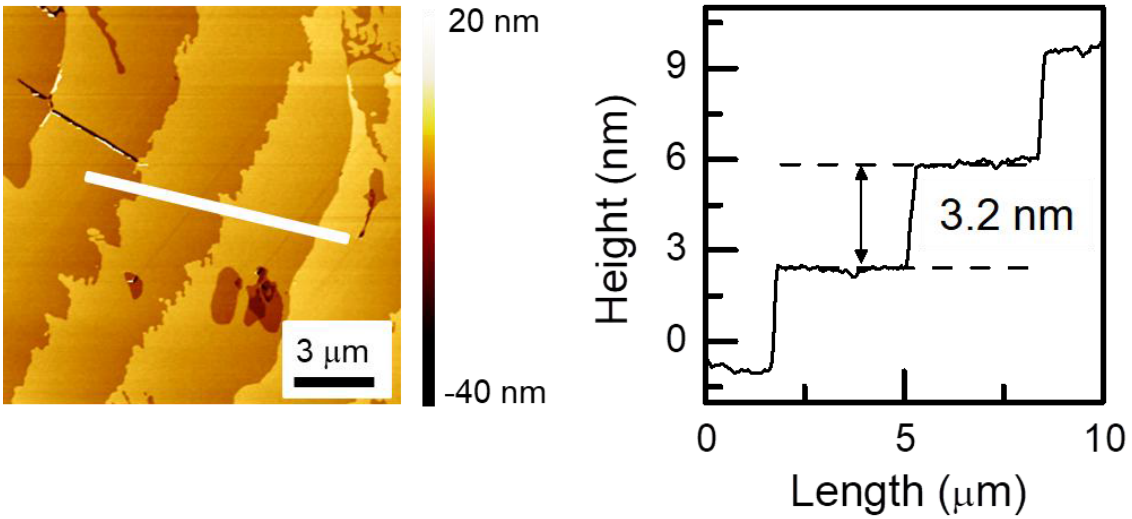

Fig. 4.10 AFM images of melt-printed C13 films and the cross-section profiles for the corresponding white lines drawn in the images. Suspension (a) and powder (b) printing films.

These results imply that the SiO_2 beads were involved in the formation of the thin films with smooth surfaces and high crystallinity by this process. Further research based on optimizing the number and/or size of SiO_2 beads in the PI films and placing spacers in order are needed. These findings led us to conclude that the suppression of these holes must be firstly prioritized in future research on our melt-printing process. Note that the bumps on the printing film are required as a spacer, as already pointed out above. We introduce controlled bumps on the PI films and report their effects in chapter 5.

4.3 Conclusion

In this chapter, we demonstrated a solvent-free printing process to prepare the active semiconductor layer for organic OTFTs at the beginning. In there, we directly melt-printed a small amount of C13 powder (less than 0.01 mg) onto a Si substrate. The AFM and microscope observations confirmed that large flat domains were prepared on a square surface area of *ca.* 1 cm^2. The highest mobility of 0.32 cm^2/Vs was exhibited by the OTFT device with the shortest channel length. These results proved that the developed process is highly efficient in the use of material. We also found that SiO_2 beads in the PI film functioned as a spacer to keep a constant distance between the printing film and substrate and contributed to the formation of molecularly flat surface of the melt-printed film. Therefore, introduction of controlled bumps on the printing film needs to be studied to clarify their effects on the crystallinity of the thin films and

performance of the resulting melt-printed OTFTs.

Chapter 5

5. Meniscus-guided melt-printing process for organic semiconducting layers

This chapter will be supported from the following presentation:

Atsuro Ohyama, Naoki Hirata, Naomi Oguma, Musubu Ichikawa*
A solvent-free transfer-printing process for organic semiconducting layers

This chapter is outlined as follows; firstly, the preparation of a new printing film named as “printing plate” is detailed with full information related to materials and methods. The SU-8 patterns are pointed out as an alternative for spacers on the vPI. Secondly, the melt-printed films prepared by using the printing plate are characterized with various measurements; AFM, XRD, GI-WAXS, and electrical measurement. These methods reveal that unnecessary defects originated from the SU-8 patterns affect the quality of the films, especially the defects in active channels when driving OTFTs. We finally provide practical patterns for device geometry in the rational melt-printing technology.

5.1 Introduction

Patterning organic semiconductor thin-films for OTFTs is mandatory for the following reasons[96]; (1) organic semiconductors are photosensitive materials which cause photo-induced charge carrier accumulation outside the active channel, resulting in high off-current[97], (2) the narrow area outside the channel of the OTFT ensures a low parasitic capacitance which can enhance an individual transistor speed[41,98]. This also prevents from generating a fringe current, which flows from the side of the source electrodes to the side of the drain current through the area, resulting in the overestimation of the charge carrier mobility[99]., (3) removing undesired organic thin-films is a better choice since weak layer adhesion of organic thin-films cause the detachment during further processes for the integration.

At present, there are many patterning techniques, mainly divided into two parts involving with when to pattern the OSC layer; a surface energy difference and directly

patterning the films in a printing process while forming the OSC layer[42,100–102], and a plasma ion-etching technique after forming the OSC layer[103]. Among them, the plasma ion-etching technique is the most promising thanks to its easy processing. However, oxygen ions generated in the technique may reach to the active channel, damage the organic thin-films, and deteriorate the device performances[103]. Therefore, a patterning method is still an interesting topic in the field of organic electronics.

As we mentioned in the previous chapter, we successfully developed a solvent-free melt-printing process combined with material's liquid isotropic phase and a polymer printing film. The silica beads in the PI film contributed to keeping a specific distance for the molten material to flow and to form molecularly flat surface with high crystallinity in cooling. In the conclusion, we questioned if we can place controlled bumps as spacers at a desired position on the PI film and pattern the OSC films. In this chapter, we concentrated on using a new PI film with controlled bumps, forming the films with various shapes, and patterning them in the process simultaneously.

5.2 Experimental

In this section, we detail about a new printing film (referred as printing plate hereafter) based on controlled bumps and the home-made polyimide film (vPI). As the controlled bumps, the photoresist patterns are prepared on the vPI by photolithography. The full information is as the follows.

5.2.1 Printing Plate

The vPI, made at our laboratory, was exploited as the base polymer for printing plates through the following steps as illustrated in Fig. 5.1. First, negative photoresist SU-8 2000.5 solution (MicroChem) diluted by 2 by using cyclopentanone was spin-coated at 3000 rpm for 45 s on the vPI, followed by soft-baking at 80 °C for 15 min and illuminating at a UV light intensity of 80 mJ/cm^2. Second, after post-baking at 150 °C for 20 min, the SU-8 patterns were prepared by splashing the droplets of ethyl lactate. The SU-8 patterns are placed to be dot or dotted-line over the area of ca. 1 cm^2. Note that we defined x axis and y axis related to the adjacent patterns as illustrated in Fig. 5.2 (b). In the case of the dot pattern, x always equals y whereas x is longer than y for the dotted-line patterns. Finally, the printing plate was completed with the solvent repelling agent and the powder melt-printing technology was proceeded as referred in chapter 2.

One might ask why the SU-8 was chosen instead of positive photoresist materials, which technically have higher resolution than the negative photoresist materials do in wet-etching[104–106]. That is because of its excellent mechanical and thermal stability to be used as the printing plate several times[107,108].

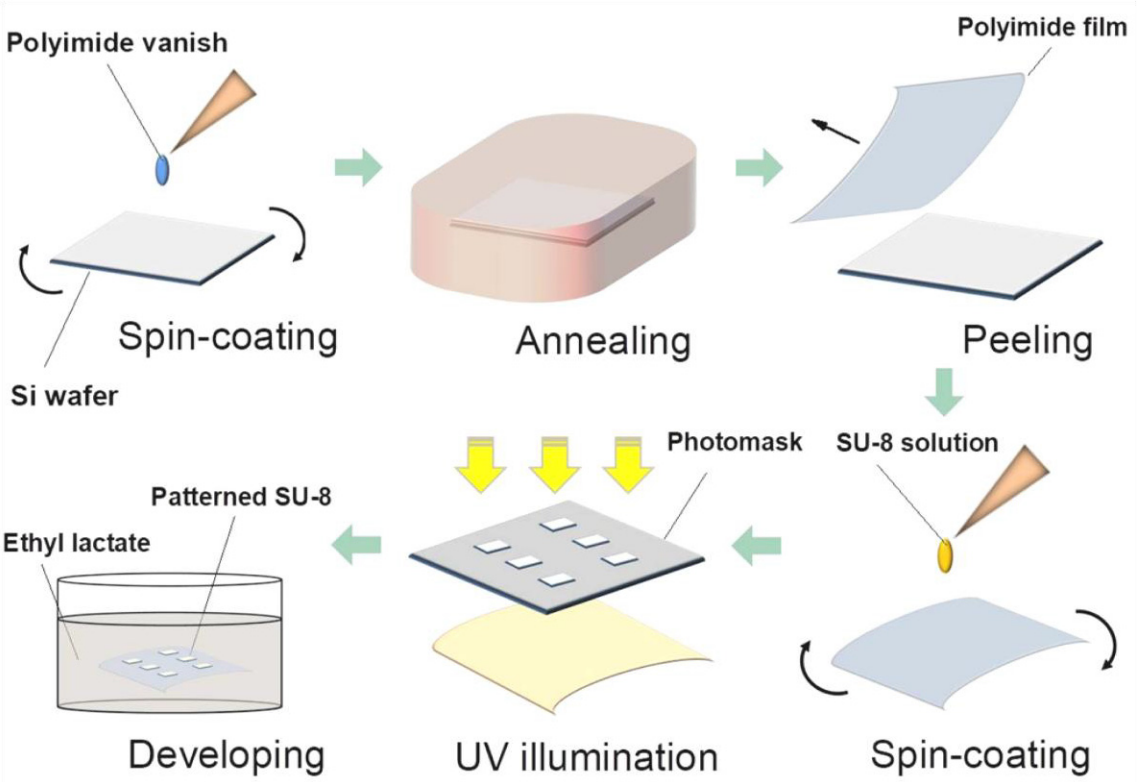

Fig. 5. 1 Schematic illustration of all steps in the preparation of the printing plate.

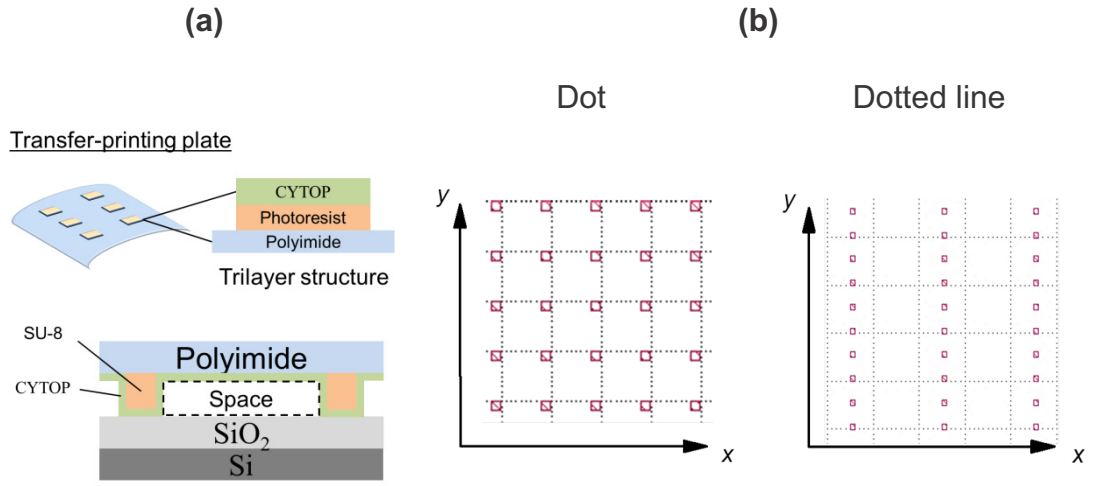

Fig. 5.2 (a) Schematic illustration of the cross section of the printing plate. (b) The SU-8 patterns designed as “Dot” and “Dotted line” with the definition of the dimensions.

5.3 Results and Discussion

Fig. 5.3 shows images of the C13, observing through the transparent printing plate before and after the beginning of the flow. To start the flow, the printing plate was softly touched to confirm a good contact with the substrate. Once the contact confirmed, the molten C13 spread until all the space was filled with the molten, and then they were cooled down to the room temperature slowly. High crystalline thin-films required a gradual decrease of the processing temperature otherwise many cracks appeared at weak spots, mostly between the defects generated from the SU-8 patterns.

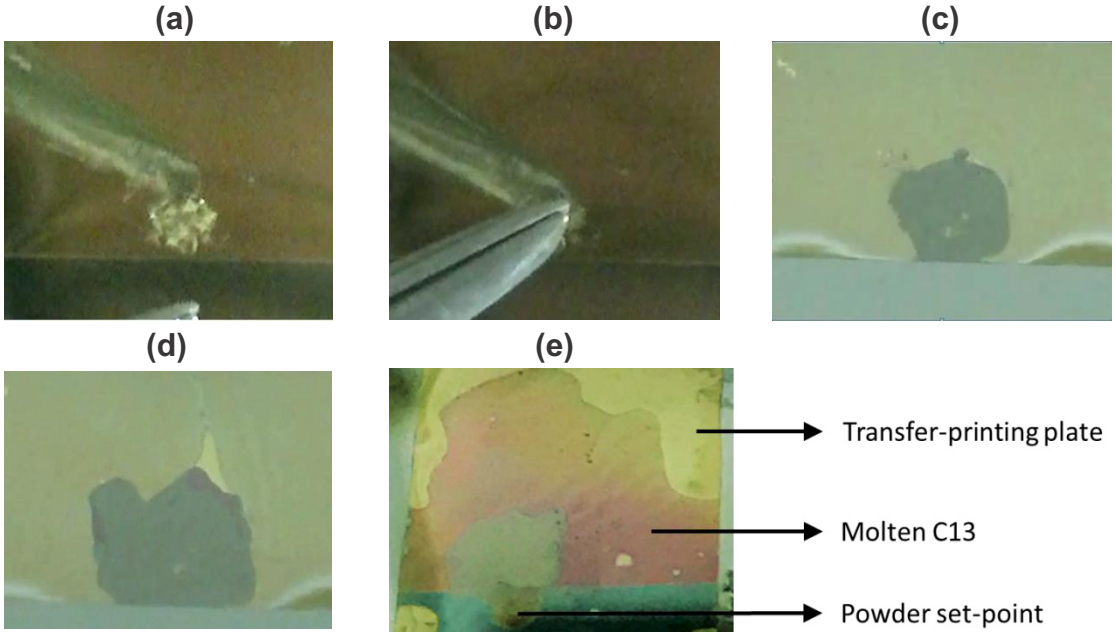

Fig. 5.3 Trace images of the molten OSC flowing time to time; (a) Just before the contact, (b) When the contacts made, (c) when the molten started flowing under the printing plate, (d) 2 second later, and (e) 5 minutes later.

5.3.1 Surface Morphology and Crystallinity

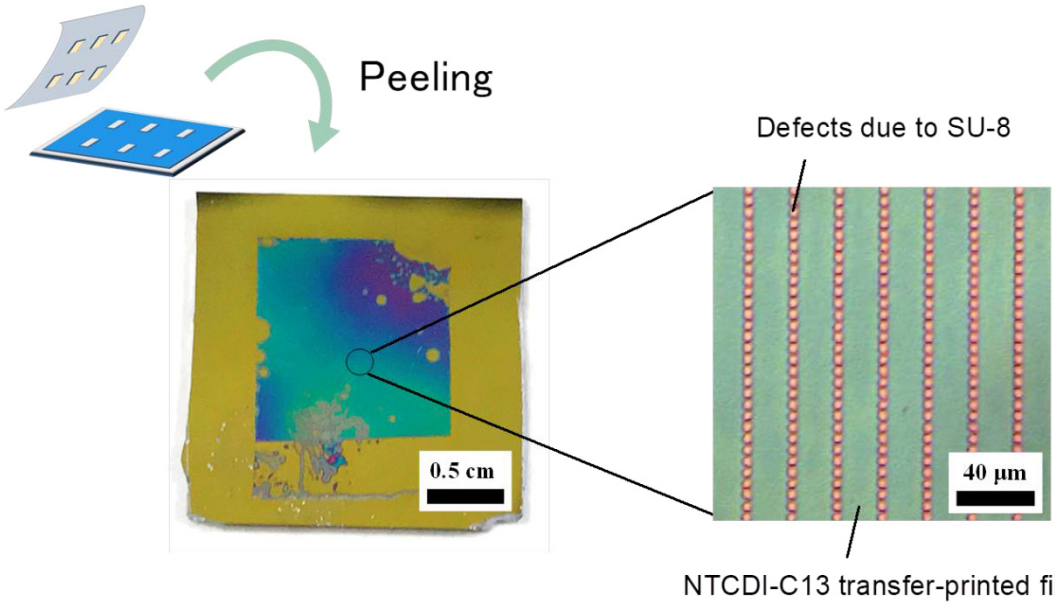

Fig. 5.4 Overview picture of a powder melt-printed C13 film prepared by using the printing plate on a Si substrate just after peeling off the plate. Image magnifying the picture on the left to show the line defects generated from the SU-8 patterns; (x, y) = (20 μm, 4 μm).

Fig. 5.4 presents a photograph of a typical powder melt-printed C13 thin film just after peeling off the plate from the substrate. We can observe a few large circular shaped defects which may result from dusts contaminated during the synthesis of C13 and the melt-printing process and can also point out the lack of the films at the edges which may originate from scratches when handling it with tweezers. Since the color gradually changes from side to side, the thickness seemed to be varied in the range of several ten nanometers. In regardless of these issues, the film was prepared exactly following our design and the magnified image proved the uniformity over the surface area of hundreds of micrometers. More importantly, the spacers do not need to be only tiny silica beads but they also can be exchanged into the micrometer scale of photoresist patterns. This is a very positive finding because photoresist patterns can form any shapes with high reproducibility in the scale of a few micrometers or even sub-micrometers in the future thanks to the maturation of the photolithography technology.

For the further investigation of the films, we also measured the surface topology of the line-patterned melt-printed film. Fig. 5.5 shows the defects generated from the SU-8 spacers were aligned in good order and the film was mostly smooth (the bright and dark

banded-patterns seen in the image are artifacts at the sharp edges of the films). This proves that we successfully patterned the melt-printed films in semi-line shapes. Thus, we prepared dotted-line patterns with varying *x* and *y* distances; (*x*, *y*) = (20 μm, 10 μm), (100 μm, 4 μm), and (200 μm, 10 μm). According to the results summarized in Fig. 5.4, there seemed to be a limitation involved with the maximum distance of each spacer. When *x* was 100 μm (Fig. 5.6 (b)), the melt-printed film was not flat but deflecting towards the farer positions from the spacers. This might induce from the molten C13 crawling in the space and drawing the printing plate with the meniscus force. When *x* reached to 200 μm, the molten C13 was fully pushed away by the part of the deflected printing plate as illustrated in Fig. 5.6 (c) and the resulting film was fully separated, leaving shallow films around the spacers. This means that the spacer can be the line-shape or whatsoever in the range of *x* and *y* distances within ca. 50 μm or less.

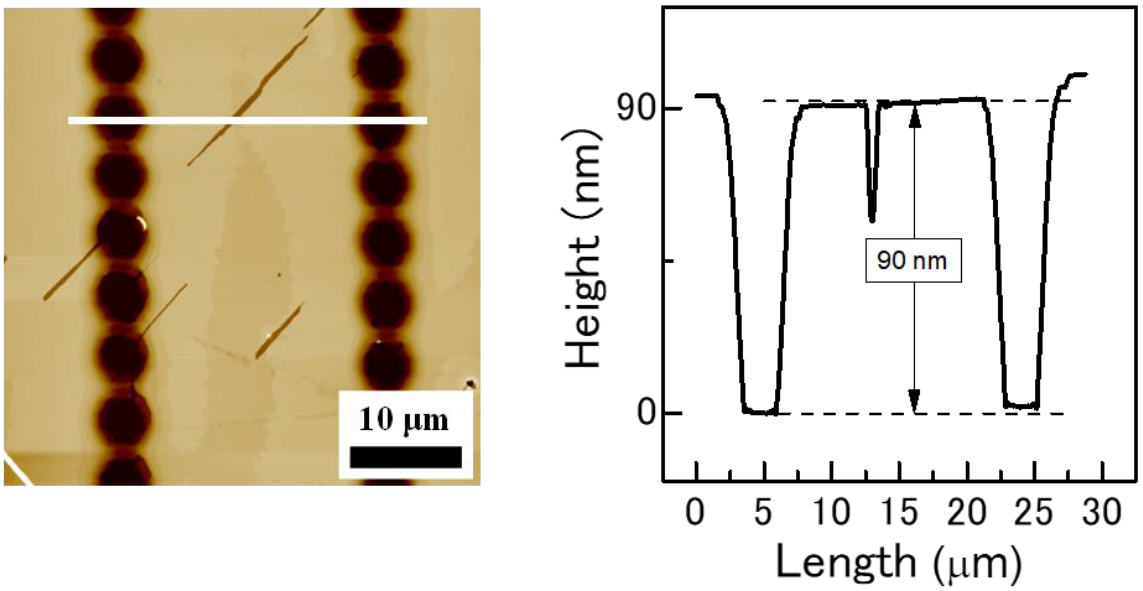

Fig. 5.5 AFM image of the line-patterned printing film and the cross-section profile for the corresponding the white line in the image. The height profile confirmed that the thickness is 90 nm in this case.

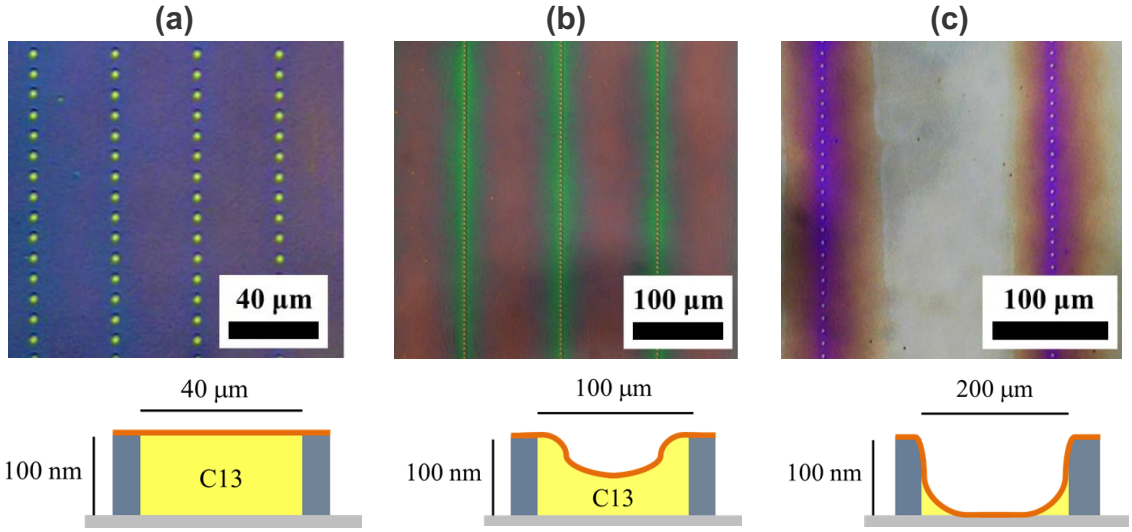

Fig. 5.6 Magnified images of powder melt-printed C13 films with different dimension of line patterns; (a) (*x, y*); (40 μm, 10 μm), (b) (*x, y*); (100 μm, 4 μm), (c) (*x, y*); (200 μm, 10 μm). The schematic illustrations of the cross section of the melt-printing set below the images.

Alongside with good findings, there are also bad ones, especially in the crystallinity. We carried out the XRD measurement in the out-of-plane direction. Fig. 5.7 shows the XRD patterns from the melt-printed films prepared by using the printing film with silica beads and dotted-line SU-8 patterns. As comparing the patterns, we observed sharp

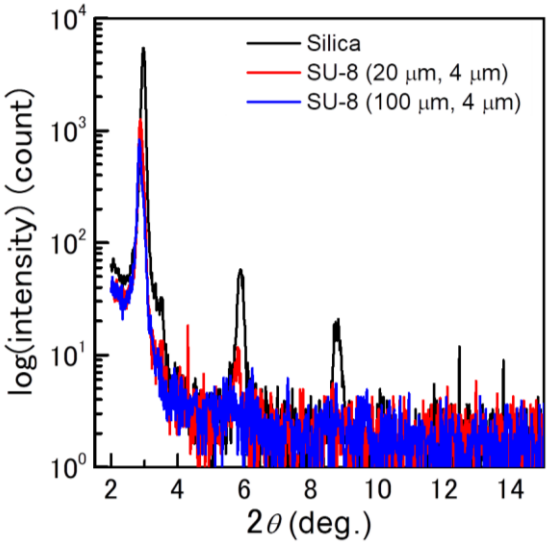

Fig. 5.7 X-ray diffraction (XRD) patterns of NTCDI-C13 thin films prepared by melt-printing with different spacers.

peaks can be indexed as (00*n*) planes of C13. The apparent difference from the black line, and the blue and red lines was found out in the progressive peaks of (00*n*); the

crystalline in the film prepared by the silica spacers consisted well-organized structures in the out-of-plane direction.

We also investigated the molecular orientation in the in-plane direction by using the grazing-incidence wide-angle X-ray scattering (GI-WAXS) measurement. Fig. 5.8 shows the representative scattering profiles of the GI-WAXS measurement for melt-printed films prepared by three different processes. As the result, the *d*-spacing of 0.33 or 0.34 estimated from the in-plane (Q_z = 0) indicates the excellent π-π stacking from all the films[50,109,110]. This is a bit in contrast to the previous XRD measurements that the SU-8 patterns resulted in low crystallinity of the out-of-plane direction. The absence of the films due to the large defects generated from the SU-8 patterns may complicate the quantitative comparison by decreasing the counts of the diffraction patterns in XRD.

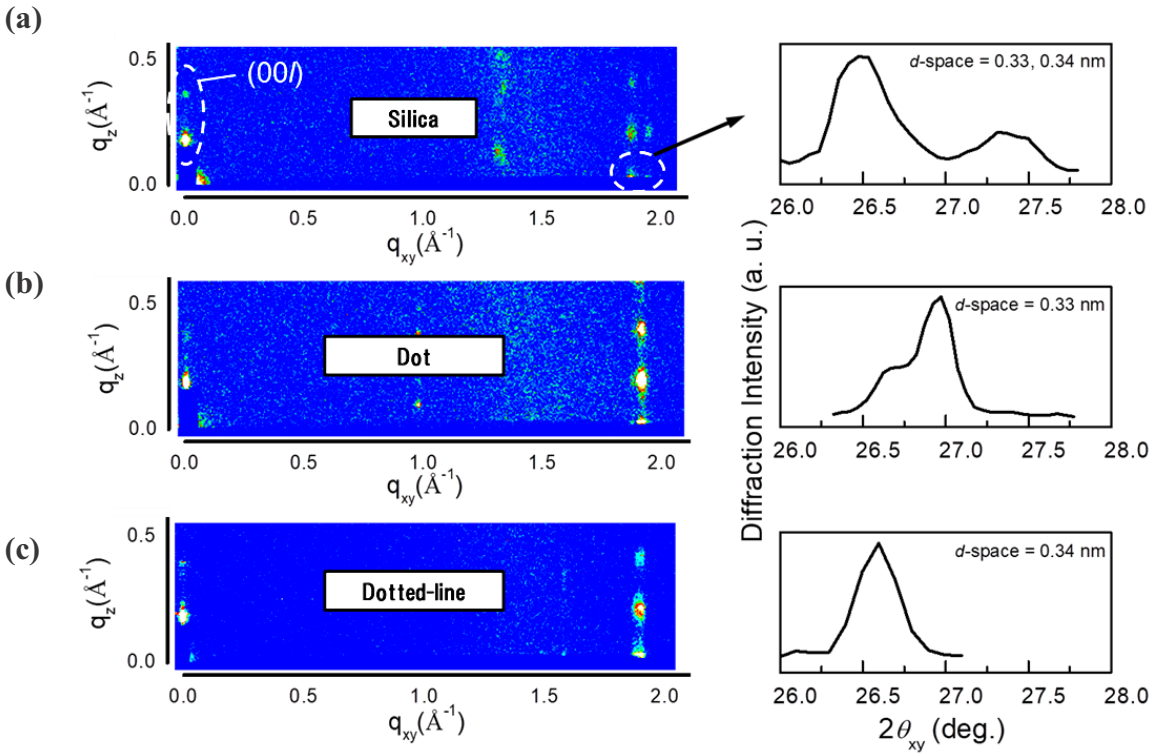

Fig. 5.8 Grazing-incidence wide-angle X-ray scattering (GI-WAXS) patterns of NTCDI-C13 thin films prepared by melt-printing with the spacer as (a) silica beads, (b) SU-8 dot patterns, (c) SU-8 dotted-line patterns.

5.3.2 Electrical property

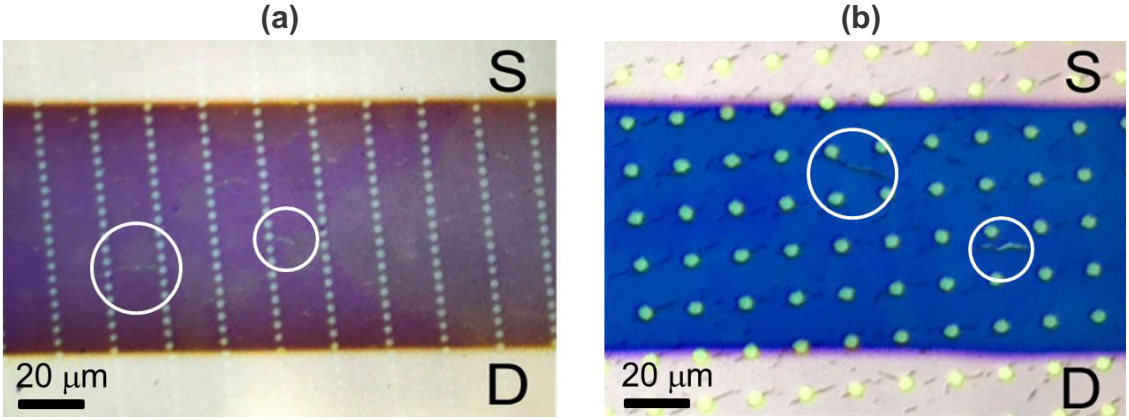

Fig. 5.9 Microscope images of the C13 TFTs completed with the thermal evaporation of gold layers as source and drain electrodes; (a) Dotted-line pattern (20 μm, 4 μm) and (b) dot pattern (20 μm, 20 μm). The substantial cracks in the active channel emphasized in the white circles.

Fig. 5.9 shows a picture of the active channel in typical C13 TFTs prepared by using the printing plates. For the both TFTs, the source and drain electrodes were evaporated to let y axis parallel to the direction of carrier transport although the y-axis was slightly tilted due to the manual mask alignment. Fig. 5.10 shows the drain current (I_D) − gate voltage (V_G) characteristics of the melt-printed and the thermal evaporated NTCDI-C13 TFTs. The electron mobilities of the melt-printed TFTs were extracted from the square root of saturation I_D vs V_G relationship to be 0.12 cm^2/Vs. However, these mobilities are inferior to the ones of the C13 OTFTs formed by the thermal evaporation and the melt-printing with the silica beads. This is because the large number of the substantial cracks occurred in the active channel trapping and slowing down the mobile carriers in the TFT operation. Note that these cracks were also observed from the melt-printed films based on other NTCDI-C*n*s and C8-BTBT and we figured out no differences in the flow and the crystallization for each material. This implies that these cracks are largely related to the mismatch of the thermal expansion coefficients between the Si wafer and the OSC in the temperature of 50-170 °C. Focusing on two microscope images in Fig. 5.9, the direction of the cracks appeared to be the one direction implying the presence of the well-aligned crystals in the thin-films. Therefore, the optimization of the SU-8 patterns to decrease the cracks, for example, the shape of the patterns and the distance of the spacers within the limitation will be required in the future.

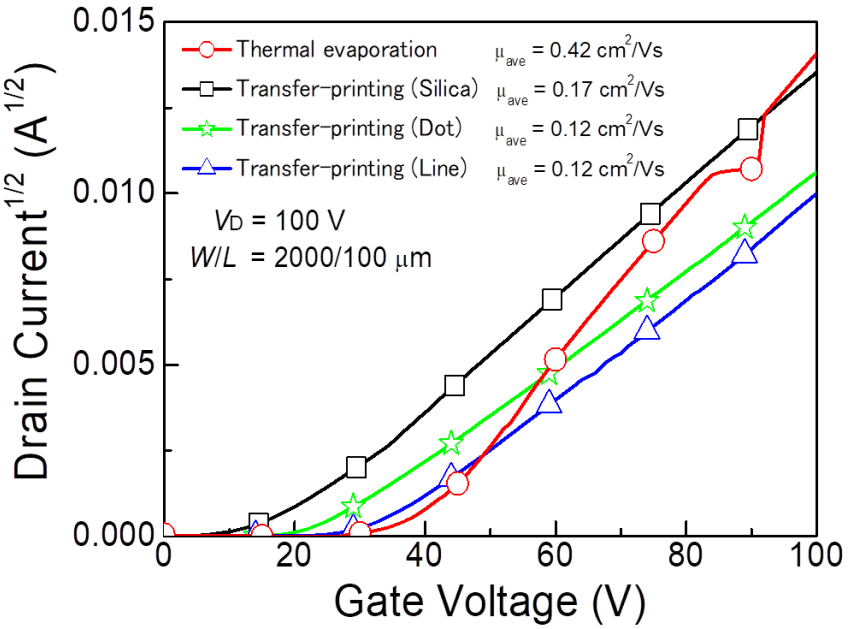

Fig. 5.10 I_D−V_G characteristics (V_D=100 V) of 30-nm-thick thermally evaporated TFTs and 80-nm-thick melt-printed TFTs with different spacers.

Table 3.3 Parameters of NTCDI-C13 TFTs formed by different processes.

Process	Spacer	μ (cm^2/Vs)	V_{th} (V)
Evaporation	**-**	**0.42**	**37**
Melt-printing	**Silica beads**	**0.17**	**18**
Melt-printing	**SU-8 dot**	**0.12**	**25**
Melt-printing	**SU-8 line**	**0.12**	**34**

5.3.3 Shape of Patterning

In 5.3.1, we pointed out to leave the direct distance of ca. 50 μm or less between the spacers to prepare homogeneous melt-printed films otherwise the meniscus force of OSCs deflected the printing plate resulting in non-homogeneous films. However, if it is in the range of the limitation, we could express various kinds of shapes; of course, the dotted-line and the dot patterns shown in Fig. 5.11 (a) and (b) and even the words “U” and ”M.” By having a closer look at the middle space of U and M, we could point out that the OSC were formed between two lines although there were also a few cracks. More interestingly, the high quality film was created in the U-shaped space with no apparent cracks, probably thanks to the additional fulcrum point between the lines to

mitigate the deflection of the printing plate. These findings will flourish our future works to precisely pattern OSC layers while controlling the quality and the crystal alignment in the films.

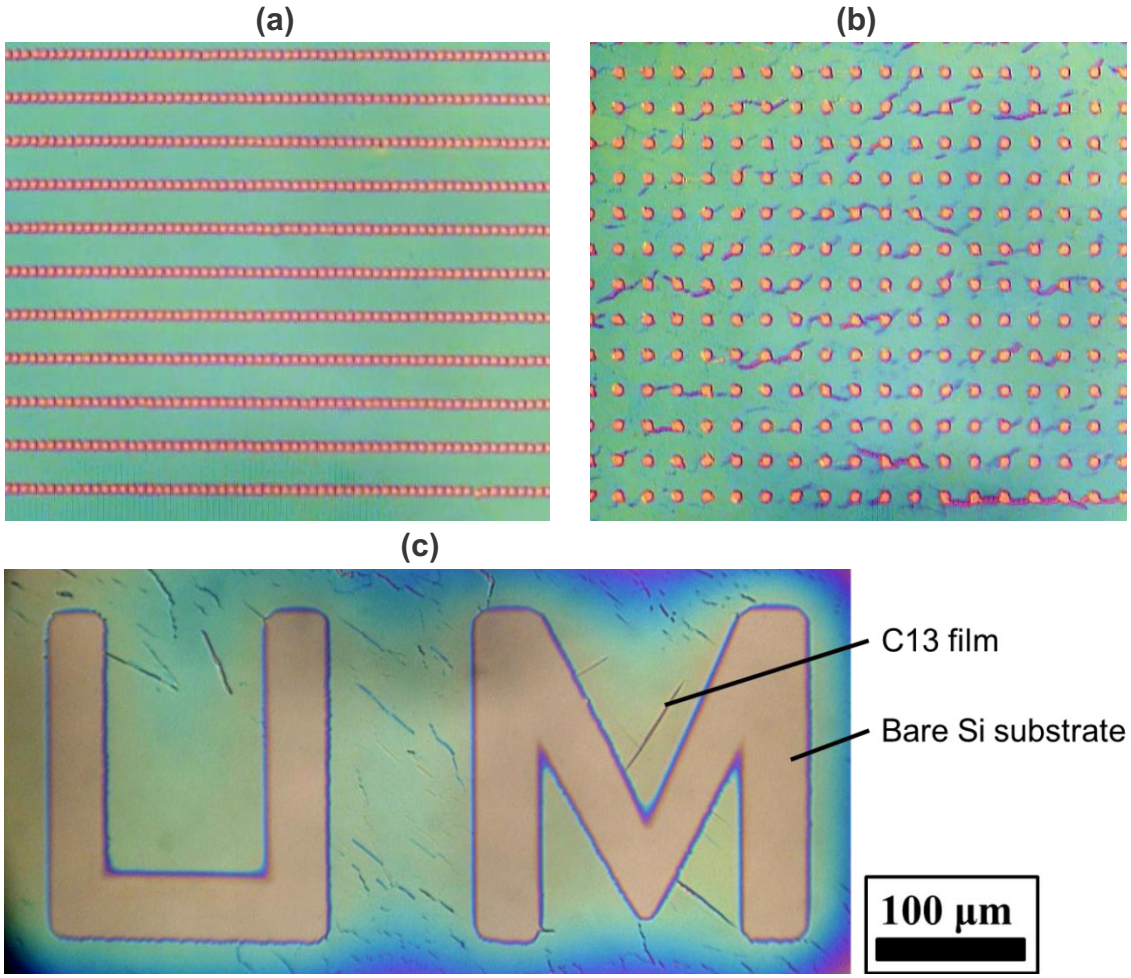

Fig. 5.11 Overview Images of the melt-printed films patterned into; dotted line (a), dot (b), and words (c).

5.4 Conclusion

In this chapter, we demonstrated the powder melt-printing process with the new melt-printing plate consisted of the SU-8 patterns and the home-made polyimide film (vPI).

First, we attempted to prepare the controlled bumps as spacers by photolithography as thin as possible and then we applied it to the powder melt-printing process to prove that the bumps worked well as the spacers instead of the Si beads leaving the melt-printed films on the substrate. By placing ca. 50 μm or less of the SU-8 spacers, the

homogeneous films were formed over the surface area of hundreds of micrometers.

Second, we optimized the distance of the spacers on the vPI with varying the *x* and *y*. When the direct distance of each spacer was more than 100 μm (*x* = 100), the printing plate was drawn and deflected by the meniscus force of the molten OSC, resulting in the non-homogeneous films. On the other hand, we did not observe such a trend when the distance was shorter than 50 μm. Therefore, we successfully determined the critical factor of the photoresist patterns as the distance of each spacer in the melt-printing technology due to the meniscus-force of the OSC. Since the meniscus-force during the flow is the driving force to form the thin-films, deeply understanding it must be essential to control the quality of the resulting films and to design new materials for the process.

Also, the XRD measurements in the out-of-plane direction were conducted on these films but the lower crystallinity compared with the one of the printed film prepared by using the printing film with the Si beads was found out although the accuracy of the comparison was unsure due to the partial lack of the films. On the other hand, the GI-WAXS measurement exhibited the sharp dots in the in-plane to prove the excellent π-π stacking which is favorable for the carrier transport in TFTs.

However, we found inferior mobilities of the C13 TFTs prepared by melt-printing with the SU-8 patterns to the ones prepared by thermally evaporating and melt-printing with the Si beads. We concluded that the substantial cracks in the active channel due to the large defects generated from the SU-8 patterns were problematic. Therefore, we require the optimization of the distance and the shape of the patterns to decrease the number of the cracks and to control the quality of the resulting films.

Finally, new designs of the SU-8 patterns were proposed from the experimental results. The patterns of the words “U” and “M” gave us some clues to flourish our work in the future; the strict fulcrum points are necessary to prevent the printing plate from deflecting by the meniscus-force of the OSC at high temperature of ca. 150 ℃.

Chapter 6

6. Conclusion and Outlook

6.1 Conclusion

In chapter 1, we discussed about the increasing demand of OLEDs which have been accelerating the research of organic electronics, including OTFTs. This led us to develop a new manufacturing process which improves a lot of issues in the conventional solution processes to prepare OTFTs. Hereby a new melt-printing process was developed combining an isotropic liquid phase and a polymer film with a solvent repellent finish.

In chapter 2, full information related to experimental conditions and materials from the selection of the OSC material to characterizations of samples was detailed.

In chapter 3, we demonstrated the melt-printing technology and optimized the process with varying kinds of OSCs and thickness of the thin-films, leading to nice outputs morphologically and electrically.

In chapter 4, the solvent-free printing process was achieved by getting rid of solvents in the system of the suspension melt-printing technology and by directly forming the films from the OSC powder. Also, we experimentally proved that the molten OSC formed the thin-films spreading in a specific space provided by silica beads thanks to their meniscus force.

In chapter 5, we focused on controlling the patterns of the spacers by using the photoresist patterns instead of the Si beads and successfully created the beautiful line shapes of OSCs and even wrote the words. The critical factor of the controlled bumps was estimated from systematic experiments, adjusting the distance of each spacer from 20 to 300 μm (only a few results are shown in the thesis) in the case of our set at the moment. Therefore, the direct distance of the spacers has to be in the range of 50 μm otherwise the meniscus force of the molten OSCs drew the printing film resulting in non-homogeneous films.

6.2 Outlook

Although the solvent-free printing process for OTFTs was demonstrated and optimized

in a careful manner, there seems to be a lot of works to do for more improvements. We point out some remedies in this section. There are roughly three areas which we could not clarify in this thesis; (1) the precise patterning of OSC layers in any shapes and at any places, (2) the decrease of the contact resistance, and (3) the design of new OSC materials for melt-processing.

First, the precise patterning of OSC layers in any shapes and at any positions should be necessarily considered for future work because the patterning of the OSC layer is mandatory since the photo-induced carrier accumulation in excess organic layers leads to high off current as we previously mentioned in chapter 5. The resolution of the patterning will reach down to sub-micrometers or even nano-meters in the future by combining our process with the well developed nanoimprint technology in industries. The simulation for nanoimprint lithography process development will significantly help to accelerate the maturation of this technology. We also raised the issue that the detachment of the fragile OSC film during the further steps for the circuit integration is unavoidable without the patterning of the OSC. In our case, we nearly achieved the patterning. As we described in Chapter 5, the photoresist patterns are usable as the spacers instead of silica beads but the direct distance of the controlled bumps are needed to be in the range of 50 μm otherwise homogeneous films are not feasible. Therefore, the design of new patterns might be alike as illustrated in Fig. 6.1. By using these patterns, we should fabricate integrated circuits such as inverters and ringoscillators. Apart from the technology of OTFTs, this process

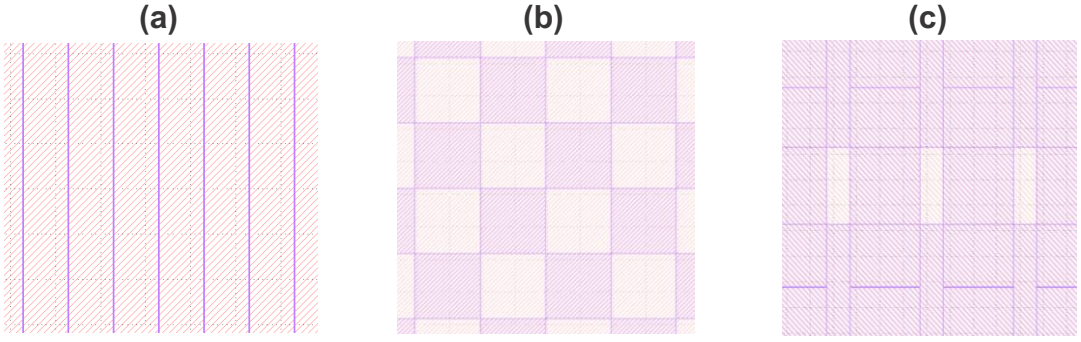

Fig. 6.1 Design of new SU-8 patterns; line (a), checked (b), and rectangular open hole. The area of dark purple is referring to the SU-8.

Second, the decrease of the contact resistance is necessary to consider our films in the integrated circuits. Increasing the number of transistors in circuits tends to make many issues if the contact resistance is too large, for example, high driving voltages and low

operation speeds. We are now researching the introduction of an electron injection layer into the printed films and gathering an interesting result that the deep holes associated with the spacers could work as a shortcut path to reduce the contact resistance although we need more proofs by using other OSC materials. In regard to the fabrication of the integrated circuits, our process will be favorable because of the controlled bumps which can pattern the OSC layer and create vias in the OSC layer to connect top and bottom metal layers without damaging the OSC.

Finally, the design of new OSC materials, which is suitable for the melt-processing, is also required. As discussed in chapter 1, the trend to shift conventional techniques into environmentally friendly ones is rapidly growing in several industries and this is not the different case for organic electronics. Taking a careful look at the solvent-free processes reported until now, all of them exploited the matter of states, especially isotropic liquid phase. Hereby, we believe that the development of new organic semiconductors which show an isotropic liquid phase is needed. Unfortunately, an indicator to design suitable materials for melt-processing is not clarified at present. Therefore, we need to find a good indicator, probably the meniscus force of the molten OSCs. Preparing the printed films from a lot of materials and gathering the information of the force will help us to design new materials and predict high quality thin-films for OTFTs.

References

[1] R.A. Soref, Proc. IEEE **81**, 1687 (1993).
[2] G.T. Reed, G. Mashanovich, F.Y. Gardes, and D.J. Thomson, Nat. Photonics **4**, 518 (2010).
[3] I. Ferain, C.A. Colinge, and J.P. Colinge, Nature **479**, 310 (2011).
[4] K. Nomura, H. Ohta, K. Ueda, T. Kamiya, M. Hirano, and H. Hosono, Science (80-.). **300**, 1269 (2003).
[5] J.A. Rogers, T. Someya, and Y. Huang, Science (80-.). **327**, 1603 (2010).
[6] G.H. Heilmeier and L.A. Zanoni, J. Phys. Chem. Solids **25**, 603 (1964).
[7] K. Kudo, M. Yamashina, and T. Moriizumi, Jpn. J. Appl. Phys. **23**, 130 (1984).
[8] F. Garnier, R. Hajlaoui, A. Yassar, and P. Srivastava, Science (80-.). **265**, 1684 (1994).
[9] W. Helfrich and W.G. Schneider, Phys. Rev. Lett. **14**, 229 (1965).
[10] C.W. Tang and S.A. VanSlyke, Appl. Phys. Lett. **51**, 913 (1987).
[11] H. Spanggaard and F.C. Krebs, Sol. Energy Mater. Sol. Cells **83**, 125 (2004).
[12] B. Maennig, J. Drechsel, D. Gebeyehu, P. Simon, F. Kozlowski, A. Werner, F. Li, S. Grundmann, S. Sonntag, M. Koch, K. Leo, M. Pfeiffer, H. Hoppe, D. Meissner, N.S. Sariciftci, I. Riedel, V. Dyakonov, and J. Parisi, Appl. Phys. A **79**, 1 (2004).
[13] B. Geffroy, P. le Roy, and C. Prat, Polym. Int. **55**, 572 (2006).
[14] D. Zhang, T. Huang, and L. Duan, Adv. Mater. 1902391 (2019).
[15] X.-H. Zhang, W.J. Potscavage, S. Choi, and B. Kippelen, Appl. Phys. Lett. **94**, 043312 (2009).
[16] Y.-Y. Lin, D.J. Gundlach, S.F. Nelson, and T.N. Jackson, IEEE Electron Device Lett. **18**, 606 (1997).
[17] S. Lee, B. Koo, J. Shin, E. Lee, H. Park, and H. Kim, Appl. Phys. Lett. **88**, 162109 (2006).
[18] F. Würthner and M. Stolte, Chem. Commun. **47**, 5109 (2011).
[19] S. Tatemichi, M. Ichikawa, T. Koyama, and Y. Taniguchi, Appl. Phys. Lett. **89**, 112108 (2006).
[20] D. Shukla, S.F. Nelson, D.C. Freeman, M. Rajeswaran, W.G. Ahearn, D.M. Meyer, and J.T. Carey, Chem. Mater. **20**, 7486 (2008).
[21] H. Ebata, T. Izawa, E. Miyazaki, K. Takimiya, M. Ikeda, H. Kuwabara, and T. Yui, J. Am. Chem. Soc. **129**, 15732 (2007).
[22] K. Nakayama, Y. Hirose, J. Soeda, M. Yoshizumi, T. Uemura, M. Uno, W. Li,

M.J. Kang, M. Yamagishi, Y. Okada, E. Miyazaki, Y. Nakazawa, A. Nakao, K. Takimiya, and J. Takeya, Adv. Mater. **23**, 1626 (2011).
[23] C. Waldauf, P. Schilinsky, M. Perisutti, J. Hauch, and C.J. Brabec, Adv. Mater. **15**, 2084 (2003).
[24] M. Chikamatsu, A. Itakura, and Y. Yoshida, Chem. Mater. **20**, 7365 (2008).
[25] M. Chikamatsu, S. Nagamatsu, Y. Yoshida, K. Saito, K. Yase, and K. Kikuchi, Appl. Phys. Lett. **87**, 1 (2005).
[26] Y. Horii, K. Sakaguchi, M. Chikamatsu, R. Azumi, K. Yase, M. Kitagawa, and H. Konishi, Appl. Phys. Express **3**, (2010).
[27] H. Yan, Z. Chen, Y. Zheng, C. Newman, J.R. Quinn, F. Dötz, M. Kastler, and A. Facchetti, Nature **457**, 679 (2009).
[28] M. Ichikawa, Y. Yokota, H.G. Jeon, G.D.R. Banoukepa, N. Hirata, and N. Oguma, Org. Electron. **14**, 516 (2013).
[29] H. Iino, T. Usui, and J. Hanna, Nat. Commun. **6**, 6828 (2015).
[30] C. Mitsui, H. Tsuyama, R. Shikata, Y. Murata, H. Kuniyasu, M. Yamagishi, H. Ishii, A. Yamamoto, Y. Hirose, M. Yano, T. Takehara, T. Suzuki, H. Sato, A. Yamano, E. Fukuzaki, T. Watanabe, Y. Usami, J. Takeya, and T. Okamoto, J. Mater. Chem. C **5**, 1903 (2017).
[31] J.-H. Dou, Y.-Q. Zheng, Z.-F. Yao, Z.-A. Yu, T. Lei, X. Shen, X.-Y. Luo, J. Sun, S.-D. Zhang, Y.-F. Ding, G. Han, Y. Yi, J.-Y. Wang, and J. Pei, J. Am. Chem. Soc. **137**, 15947 (2015).
[32] H. Klauk, editor , Org. Electron. Wiley, chapter 1 (2006).
[33] K. Jung, Y.C. Kim, H. Shin, B. Park, J.D. Lee, E.S. Cho, and S.J. Kwon, Appl. Phys. Lett. **96**, 103305 (2010).
[34] D. Gupta, M. Katiyar, and D. Gupta, Org. Electron. Physics, Mater. Appl. **10**, 775 (2009).
[35] K. Noda, Y. Wada, and T. Toyabe, Org. Electron. **15**, 1571 (2014).
[36] L. Torsi, N. Cioffi, C. Di Franco, L. Sabbatini, P.G. Zambonin, and T. Bleve-Zacheo, Solid. State. Electron. **45**, 1479 (2001).
[37] C. Liu, G. Li, R. Di Pietro, J. Huang, Y.-Y. Noh, X. Liu, and T. Minari, Phys. Rev. Appl. **8**, 034020 (2017).
[38] D.K. Schroder, Semicond. Mater. Device Charact. **second ed.**, 1998 Chap. 3 (2006).
[39] D.M. Taylor, Semicond. Sci. Technol. **30**, 054002 (2015).
[40] Z. Ding, G.A.W. Abbas, H.E. Assender, J.J. Morrison, S.G. Yeates, E.R. Patchett, and D.M. Taylor, Org. Electron. **31**, 90 (2016).

[41] E.R. Patchett, A. Williams, Z. Ding, G. Abbas, H.E. Assender, J.J. Morrison, S.G. Yeates, and D.M. Taylor, Org. Electron. Physics, Mater. Appl. **15**, 1493 (2014).
[42] B. Kang, W.H. Lee, and K. Cho, ACS Appl. Mater. Interfaces **5**, 2302 (2013).
[43] S.K. Park, T.N. Jackson, J.E. Anthony, and D.A. Mourey, Appl. Phys. Lett. **91**, 063514 (2007).
[44] Z. He, K. Xiao, W. Durant, D.K. Hensley, J.E. Anthony, K. Hong, S.M. Kilbey, J. Chen, and D. Li, Adv. Funct. Mater. **21**, 3617 (2011).
[45] R.D. Deegan, O. Bakajin, and T.F. Dupont, Nature **389**, 827 (1997).
[46] K. Norrman, A. Ghanbari-Siahkali, and N.B. Larsen, Annu. Reports Prog. Chem. - Sect. C **101**, 174 (2005).
[47] F.J. Zhang, C.A. Di, N. Berdunov, Y. Hu, Y. Hu, X. Gao, Q. Meng, H. Sirringhaus, and D. Zhu, Adv. Mater. **25**, 1401 (2013).
[48] Y. Li, C. Liu, A. Kumatani, P. Darmawan, T. Minari, and K. Tsukagoshi, Org. Electron. **13**, 264 (2012).
[49] A. Kumatani, C. Liu, Y. Li, P. Darmawan, K. Takimiya, T. Minari, and K. Tsukagoshi, Sci. Rep. **2**, 393 (2012).
[50] Y. Yuan, G. Giri, A.L. Ayzner, A.P. Zoombelt, S.C.B. Mannsfeld, J. Chen, D. Nordlund, M.F. Toney, J. Huang, and Z. Bao, Nat. Commun. **5**, 3005 (2014).
[51] R. Janneck, F. Vercesi, P. Heremans, J. Genoe, and C. Rolin, Adv. Mater. **28**, 8007 (2016).
[52] A. Pierre, M. Sadeghi, M.M. Payne, A. Facchetti, J.E. Anthony, and A.C. Arias, Adv. Mater. **26**, 5722 (2014).
[53] M.R. Niazi, R. Li, E. Qiang Li, A.R. Kirmani, M. Abdelsamie, Q. Wang, W. Pan, M.M. Payne, J.E. Anthony, D.-M. Smilgies, S.T. Thoroddsen, E.P. Giannelis, and A. Amassian, Nat. Commun. **6**, 8598 (2015).
[54] T. Hamai, S. Arai, H. Minemawari, S. Inoue, R. Kumai, and T. Hasegawa, Phys. Rev. Appl. **8**, 054011 (2017).
[55] R. Janneck, N. Pilet, S.P. Bommanaboyena, B. Watts, P. Heremans, J. Genoe, and C. Rolin, Adv. Mater. **29**, 1703864 (2017).
[56] A. Yamamura, S. Watanabe, M. Uno, M. Mitani, C. Mitsui, J. Tsurumi, N. Isahaya, Y. Kanaoka, T. Okamoto, and J. Takeya, Sci. Adv. **4**, 1 (2018).
[57] M. Ikawa, T. Yamada, H. Matsui, H. Minemawari, J. Tsutsumi, Y. Horii, M. Chikamatsu, R. Azumi, R. Kumai, and T. Hasegawa, Nat. Commun. **3**, 1176 (2012).
[58] Y. Aleeva and B. Pignataro, J. Mater. Chem. C **2**, 6436 (2014).

[59] N.A. Azarova, J.W. Owen, C.A. McLellan, M.A. Grimminger, E.K. Chapman, J.E. Anthony, and O.D. Jurchescu, Org. Electron. **11**, 1960 (2010).
[60] S.E. Shaheen, R. Radspinner, N. Peyghambarian, and G.E. Jabbour, Appl. Phys. Lett. **79**, 2996 (2001).
[61] P.H. Lau, K. Takei, C. Wang, Y. Ju, J. Kim, Z. Yu, T. Takahashi, G. Cho, and A. Javey, Nano Lett. **13**, 3864 (2013).
[62] M. Hambsch, K. Reuter, M. Stanel, G. Schmidt, H. Kempa, U. Fügmann, U. Hahn, and A.C. Hübler, Mater. Sci. Eng. B **170**, 93 (2010).
[63] H. Minemawari, T. Yamada, H. Matsui, J. Tsutsumi, S. Haas, R. Chiba, R. Kumai, and T. Hasegawa, Nature **475**, 364 (2011).
[64] G. Grau, R. Kitsomboonloha, S.L. Swisher, H. Kang, and V. Subramanian, Adv. Funct. Mater. **24**, 5067 (2014).
[65] H. Kang, R. Kitsomboonloha, K. Ulmer, L. Stecker, G. Grau, J. Jang, and V. Subramanian, Org. Electron. Physics, Mater. Appl. **15**, 3639 (2014).
[66] J. Sun, H. Park, Y. Jung, G. Rajbhandari, B.B. Maskey, A. Sapkota, Y. Azuma, Y. Majima, and G. Cho, ACS Omega **2**, 5766 (2017).
[67] G. Grau, J. Cen, H. Kang, R. Kitsomboonloha, W.J. Scheideler, and V. Subramanian, Flex. Print. Electron. **1**, 023002 (2016).
[68] K. Alfonsi, J. Colberg, P.J. Dunn, T. Fevig, S. Jennings, T.A. Johnson, H.P. Kleine, C. Knight, M.A. Nagy, D.A. Perry, and M. Stefaniak, Green Chem. **10**, 31 (2008).
[69] J. Fauvarque, Appl. Catal. B Environ. **12**, N23 (1997).
[70] D.J. Burke and D.J. Lipomi, Energy Environ. Sci. **6**, 2053 (2013).
[71] G.C. Windham, L. Zhang, R. Gunier, L.A. Croen, and J.K. Grether, Environ. Health Perspect. **114**, 1438 (2006).
[72] Z.B. Henson, P. Zalar, X. Chen, G.C. Welch, T.-Q. Nguyen, and G.C. Bazan, J. Mater. Chem. A **1**, 11117 (2013).
[73] J. Cho, K.H. Cheon, K.H. Park, S.-K. Kwon, Y.-H. Kim, and D.S. Chung, Org. Electron. **24**, 160 (2015).
[74] M. Sakai, T. Okamoto, Y. Yamazaki, J. Hayashi, S. Yamaguchi, S. Kuniyoshi, H. Yamauchi, Y. Sadamitsu, M. Hamada, and K. Kudo, Phys. Status Solidi - Rapid Res. Lett. **7**, 1093 (2013).
[75] T. Sasaki, M. Sakai, T. Ko, Y. Okada, H. Yamauchi, K. Kudo, Y. Sadamitsu, and S. Shinamura, Adv. Electron. Mater. **2**, 1500221 (2016).
[76] T. Matsushima, A.S.D. Sandanayaka, Y. Esaki, and C. Adachi, Sci. Rep. **5**, 14547 (2015).

[77] Z.K. Kao, Y.H. Hung, and Y.C. Liao, J. Mater. Chem. **21**, 18799 (2011).
[78] M. Kanzaki, Y. Kawaguchi, and H. Kawasaki, ACS Appl. Mater. Interfaces **9**, 20852 (2017).
[79] C.P. Udawatte, K. Yanagisawa, and S. Nasu, J. Solid State Chem. **154**, 444 (2000).
[80] M. Ichikawa, K. Iwasaki, A. Ohyama, J. Miyazawa, Y. Yokota, N. Hirata, and N. Oguma, Jpn. J. Appl. Phys. **56**, 111601 (2017).
[81] H.E. Katz, J. Johnson, A.J. Lovinger, and W. Li, J. Am. Chem. Soc. **122**, 7787 (2000).
[82] M.R. Churchill, Inorg. Chem. **12**, 1213 (1973).
[83] S. Bates, G. Zografi, D. Engers, K. Morris, K. Crowley, and A. Newman, Pharm. Res. **23**, 2333 (2006).
[84] B.D. Cullity and S.R. Stock, PEARSON, Edinburgh, U.K. **2001**, Chap. 4 (1979).
[85] S. Kobayashi and K. Inaba, 1 (2014).
[86] Y. Wu, P. Liu, S. Gardner, and B.S. Ong, Chem. Mater. **17**, 221 (2005).
[87] R. Ruiz, A. Papadimitratos, A.C. Mayer, and G.G. Malliaras, Adv. Mater. **17**, 1795 (2005).
[88] H. Sirringhaus, T. Kawase, R.H. Friend, T. Shimoda, M. Inbasekaran, W. Wu, and E.P. Woo, Science (80-.). **290**, 2123 (2000).
[89] A.C. Huebler, F. Doetz, H. Kempa, H.E. Katz, M. Bartzsch, N. Brandt, I. Hennig, U. Fuegmann, S. Vaidyanathan, J. Granstrom, S. Liu, A. Sydorenko, T. Zillger, G. Schmidt, K. Preissler, E. Reichmanis, P. Eckerle, F. Richter, T. Fischer, and U. Hahn, Org. Electron. **8**, 480 (2007).
[90] H. Kang, R. Kitsomboonloha, J. Jang, and V. Subramanian, Adv. Mater. **24**, 3065 (2012).
[91] S.R. Forrest, Nature **428**, 911 (2004).
[92] K.-Y. Wu, T.-Y. Wu, S.-T. Chang, C.-S. Hsu, and C.-L. Wang, Adv. Mater. **27**, 4371 (2015).
[93] H.-L. Cheng, W.-Q. Lin, and F.-C. Wu, Appl. Phys. Lett. **94**, 223302 (2009).
[94] A. Ohyama, J. Miyazawa, Y. Yokota, N. Hirata, N. Oguma, and M. Ichikawa, Org. Electron. **58**, 231 (2018).
[95] H. Sirringhaus, Adv. Mater. **17**, 2411 (2005).
[96] M. Höppner, D. Kneppe, H. Kleemann, and K. Leo, Org. Electron. **76**, 105357 (2020).
[97] N.K. Za'aba and D.M. Taylor, Org. Electron. **65**, 39 (2019).

[98] C.P. Watson, B.A. Brown, J. Carter, J. Morgan, and D.M. Taylor, Adv. Electron. Mater. **2**, 1500322 (2016).
[99] K. Pei, M. Chen, Z. Zhou, H. Li, and P.K.L. Chan, ACS Appl. Electron. Mater. **1**, 379 (2019).
[100] S.C. Lim, S.H. Kim, J.H. Lee, M.K. Kim, D.J. Kim, and T. Zyung, Synth. Met. **148**, 75 (2005).
[101] U. Zschieschang, M. Halik, and H. Klauk, Langmuir **24**, 1665 (2008).
[102] S. Li, Y.T. Chun, S. Zhao, H. Ahn, D. Ahn, J.I. Sohn, Y. Xu, P. Shrestha, M. Pivnenko, and D. Chu, Nat. Commun. **9**, 393 (2018).
[103] S. Steudel, K. Myny, S. De Vusser, J. Genoe, and P. Heremans, Appl. Phys. Lett. **89**, 183503 (2006).
[104] C. Martin-Olmos, L.G. Villanueva, P.D. Van Der Wal, A. Llobera, N.F. De Rooij, J. Brugger, and F. Perez-Murano, Adv. Funct. Mater. **22**, 1482 (2012).
[105] I.S. Amiri, V.J. Sorger, M.M. Ariannejad, X. Ling, M. Ghasemi, and P. Yupapin, Microsyst. Technol. **24**, 1673 (2018).
[106] W.-M. Yeh, D.E. Noga, R.A. Lawson, L.M. Tolbert, and C.L. Henderson, J. Vac. Sci. Technol. B, Nanotechnol. Microelectron. Mater. Process. Meas. Phenom. **28**, C6S6 (2010).
[107] C.P. Watson, B.A. Brown, J. Carter, J. Morgan, and D.M. Taylor, Adv. Electron. Mater. **2**, 1500322 (2016).
[108] J. Greener, W. Li, J. Ren, D. Voicu, V. Pakharenko, T. Tang, and E. Kumacheva, Lab Chip **10**, 522 (2010).
[109] A. Welford, S. Maniam, E. Gann, X. Jiao, L. Thomsen, S.J. Langford, and C.R. McNeill, Org. Electron. **75**, 105378 (2019).
[110] X. Jiao, S. Maniam, S.J. Langford, and C.R. McNeill, Phys. Rev. Mater. **3**, 013606 (2019).

List of publishments

Atsuro Ohyama, Jun Miyazawa, Yoichiro Yokota, Naoki Hirata, Naomi Oguma, Musubu Ichikawa, **Printing technology based on isotropic liquid phase of naphthalene diimide derivatives for n-type organic transistors**

Atsuro Ohyama, Naoki Hirata, Naomi Oguma, Musubu Ichikawa, **Solvent-free printing process for organic transistors using a naphthalene diimide bearing long alkyl chains**

Musubu Ichikawa, Kazuaki Iwasaki, Atsuro Ohyama, Jun Miyazawa, Yoichiro Yokota, Naoki Hirata, Naomi Oguma, **Comparative study of long alkyl chain substituted naphthalene diimide drivatives as n-type organic thin-film transistor materials**

Conference Presentations

Atsuro Ohyama, Naoki Oguma, Naoki Hirata, Musubu Ichikawa
転写法を用いて作製した長鎖アルキル鎖長を有するナフタレンジイミド誘導体膜のトランジスタ特性
第 76 回応用物理学会秋季学術講演会, 2015 年 9 月 15 日発表

Atsuro Ohyama, Naoki Oguma, Naoki Hirata, Musubu Ichikawa 融点処理を利用した溶媒フリー転写プロセスによる n 型トランジスタの開発
第 77 回応用物理学会秋季学術講演会, 2016 年 9 月 15 日発表

Atsuro Ohyama, Naoki Oguma, Naoki Hirata, Musubu Ichikawa
長鎖アルキル基を有するペリレンジミド誘導体転写膜のトランジスタ特性
第 77 回応用物理学会秋季学術講演会, 2016 年 9 月 15 日発表

Atsuro Ohyama, Naoki Oguma, Naoki Hirata, Musubu Ichikawa
極薄フォトレジストパターンをスペーサーとして利用した有機半導体膜の無溶媒転写形成
第 79 回応用物理学会秋季学術講演会, 2018 年 9 月 19 日発表

Atsuro Ohyama, Naoki Oguma, Naoki Hirata, Musubu Ichikawa 溶融転写法で作製した C8-BTBT 薄膜のトランジスタ特性
第80回応用物理学会秋季学術講演会, 2019年9月22日発表

Atsuro Ohyama, Naoki Oguma, Naoki Hirata, Musubu Ichikawa
A solvent-free transfer-printing process for organic semiconducting layers
EM-NANO, (presented on Dec. in 2019)